

Impedance spectroscopy: A general introduction and application to dye-sensitized solar cells

Juan Bisquert and Francisco Fabregat-Santiago

Photovoltaic and Optoelectronic Devices Group, Departament de Física, Universitat Jaume I, 12071 Castelló, Spain

in Dye-sensitized Solar Cells

By Kuppuswamy Kalyanasundaram

<https://www.taylorfrancis.com/books/e/9780429156359/chapters/10.1201/b16409-17>

10.1. Introduction

Impedance Spectroscopy (IS) has become a major tool to investigate the properties and quality of dye-sensitized solar cells (DSC) devices. In this chapter we provide an introduction of IS methods of interpretation focusing on the analysis of DSC impedance data, as well as a scope of the main results obtained so far. IS also gives access to fundamental mechanisms of operation of solar cells, therefore we will discuss our views of basic photovoltaic principles that are required to realize the interpretation of the experimental results. The chapter summarizes some 10 years of experience of the authors in modeling, measurement and interpretation of IS applied in DSC.

A good way to start this subject is a brief recollection of how it evolved over the first years. The original “standard” configuration of a DSC¹ that emerged in the early 1990s is formed by a large internal area nanostructured TiO₂ semiconductor, connected to a transparent conducting oxide (TCO), coated with photoactive dye molecules, and in contact with redox I⁻/I₃⁻ electrolyte, that is in turn connected to Pt-catalyzed counterelectrode (CE). The DSC developed initially as a photoelectrochemical solar cell. Electrochemical Impedance Spectroscopy (EIS) is a traditional method, central to electrochemical science and technology. Electrochemistry usually investigates interfacial charge transfer between a solid conductor (the working electrode, WE) and an electrolyte, by a voltage applied between WE and CE, with the assistance of a reference electrode (RE), that allows to identify the voltage drop at the interface between the WE and the electrolyte. In addition the electrolyte often contains a salt that provides a large conductivity in the liquid phase and removes limitations by drift transport in electrical field, thus electrochemistry is mostly concerned with interfacial charge transfer events, possibly governed by diffusion of reactants or products. EIS allows to readily separate the interfacial capacitance and charge-transfer resistance, and to identify diffusion components in the electrolyte as well. A good introduction to such applications is given by Gabrielli.²

In solid state solar cell science and technology the most commonly applied frequency technique is Admittance Spectroscopy (AS). By tradition AS denominates a special method that operates at reverse voltage and evaluates the energy levels of majority carrier traps (in general, all those that cross the Fermi level) as well as trap densities of states.³ In work on DSCs and other solar cells we may be interested to probe a wide

variety of conditions, so we generally use the denomination Impedance Spectroscopy (IS) to denote the technique applied in this context (rather than EIS or AS).

Before the advent of DSC, IS had been widely applied in photoelectrochemistry.^{4,5} This is a field widely explored since the 1970s, using compact monocrystalline or polycrystalline semiconductor electrodes for sunlight energy conversion.⁶⁻⁸ In these systems IS provides information on the electronic carrier concentration at the surface, via Mott-Schottky plots (i.e. the reciprocal square capacitance versus the bias voltage) characterization and on the rates of interfacial charge transfer.⁹⁻¹¹ Several important concepts, later to be applied in DSC, were established at that time, such as the bandedge shift by charging of the Helmholtz layer and the crucial role of surface states in electron or hole transfer to acceptors in solution.^{9,10,12-14} Nonetheless, it was clearly recognized that applying IS in these systems is far from trivial, for example due to the presence of frequency dispersion that complicates the determination of parameters.¹⁵

It was natural to apply such well established electrochemical methods to DSC and several groups did so.¹⁶⁻¹⁹ However in the early studies it was necessary to clarify a conceptual framework of interpretation and this took several years. On the one hand, the early diffusion-recombination model,²⁰ was generally adopted for steady-state techniques and produced very good results when extended to light-modulated frequency techniques.²¹ In this approach the only role of the applied voltage is to establish the concentration of electrons at the edge of the TiO₂ in contact with TCO.^{20,21} On the other hand, classical photoelectrochemical methods heavily rest on the notion of charge collection at the surface space-charge layer, while diffusion is viewed as an auxiliary component, at best.²² Thus in photoelectrochemistry of compact semiconductor electrodes the main method to describe the system behavior is an understanding of the electric potential distribution between the bulk semiconductor and the semiconductor/electrolyte interface.⁷

Owing to these conflicting approaches, in the DSC area there were many discussions about the distribution of the applied voltage as internal “potential drops”, the origin of photovoltage, screening, and the role of electron-hole separation at space-charge region.²³⁻²⁷ This is understandable since the DSC is a porous, heterogeneous system, and in models of systems with a complex morphology, it is generally difficult to match diffusion control with a precise statement about the electrical potential distribution. The key element for progress is to adopt a macrohomogeneous approach and focus in the

spatial distribution of the Fermi level. This approach emerged in the DSC area^{24,28-30} and eventually led to generalized photovoltaic principles based on splitting of Fermi levels and the crucial role of selective contacts.³¹⁻³⁴ Another central concept that appeared in the DSC area was a “conduction band capacitance”,^{26,28,30} later to be generally defined as a chemical capacitance.³⁵ This capacitive element is normally absent in classical photoelectrochemistry but it is central for the interpretation of frequency resolved techniques in DSC. Also important was the recognition^{26,36} that nanostructured TiO₂ should be treated as a disordered material, much like the amorphous semiconductors,³⁷⁻³⁹ with electronic traps affecting not only the surface events, but any differential/kinetic measurements, including the chemical capacitance,³⁵ recombination lifetime and transport coefficients.⁴⁰

The passage from established ideas of photoelectrochemistry to those best suited to the DSC inevitably required to treat the porous-mixed phase structure of the DSC. But Electrochemistry was already evolving in this direction for some decades, first with the description of porous electrodes,⁴¹ and then, with the introduction of truly active electrodes that become modified under bias voltage, such as intercalation metal-oxides,⁴² conducting polymers⁴³ and redox polymers.⁴⁴ Especially the work of Chidsey and Murray⁴⁴ importantly shows the modification of the diffusion coefficient in the solid phase, as well as the capacitance of the solid material as a whole, in opposition to the standard interfacial capacitance. In the analysis of these systems, either porous or not, it was well recognized the importance of coupling transport elements with interfacial and/or recombination components for proper description of IS data. Transmission line models provide a natural representation of the IS models and were widely used.^{43,45}

Transmission line models incorporating frequency dispersion that is ubiquitous in disordered materials were developed and applied to nanostructured TiO₂ used in DSC, Fig. 1, and a very good realization of the model was soon found in the experiment, as shown in Fig. 2.⁴⁶ Later, diffusion-reaction models were solved for IS characterization, and the models were put in relation to both nanostructured semiconductors and bulk semiconductors for solar cells.⁴⁷ Disorder was included also in generalized transmission lines for anomalous diffusion.⁴⁸ The role of macroscopic contacts was also analyzed in generalized transmission line models, as shown in Fig. 1(b),⁴⁹ and this effect would take relevance because of the TCO contribution to the measured impedance.^{50,51}

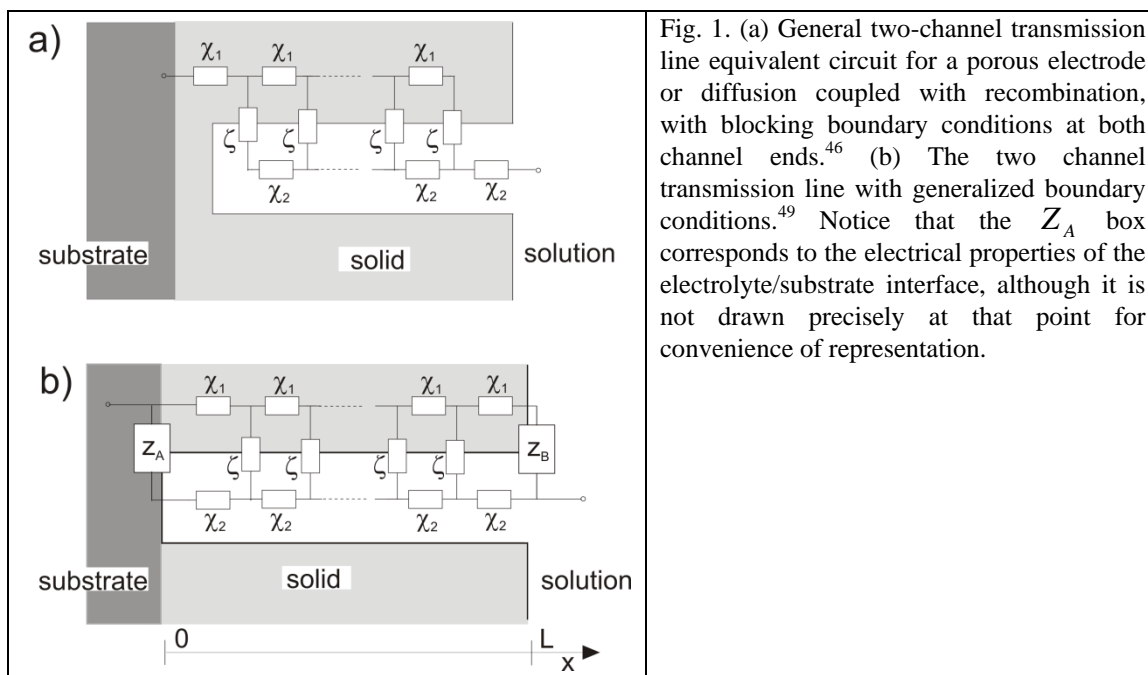


Fig. 1. (a) General two-channel transmission line equivalent circuit for a porous electrode or diffusion coupled with recombination, with blocking boundary conditions at both channel ends.⁴⁶ (b) The two channel transmission line with generalized boundary conditions.⁴⁹ Notice that the Z_A box corresponds to the electrical properties of the electrolyte/substrate interface, although it is not drawn precisely at that point for convenience of representation.

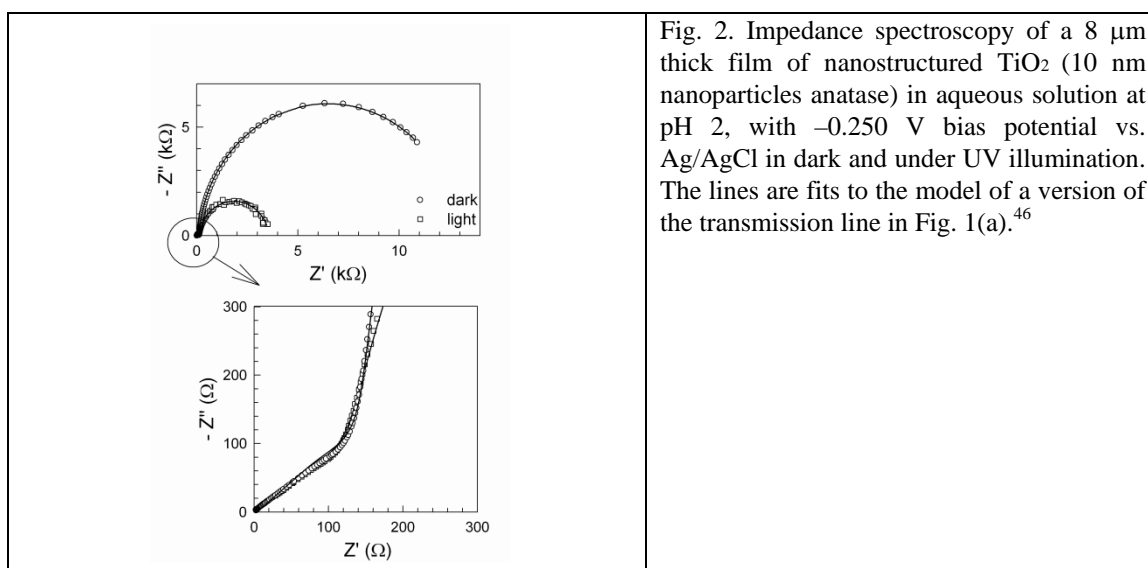


Fig. 2. Impedance spectroscopy of a 8 μm thick film of nanostructured TiO_2 (10 nm nanoparticles anatase) in aqueous solution at pH 2, with -0.250 V bias potential vs. Ag/AgCl in dark and under UV illumination. The lines are fits to the model of a version of the transmission line in Fig. 1(a).⁴⁶

The calculation of the diffusion-recombination impedance⁴⁷ opened the way for a direct measurement of conductivity of electrons in TiO_2 by IS⁵² that provided a good validation of the method. Further, the diffusion-recombination impedance also reveals naturally⁴⁷ the chemical capacitance of electrons in nanostructured TiO_2 (associated to the rise of the Fermi level), which appears as well in measurements of cyclic voltammetry (at slow scan rates)⁵³ and electron lifetime.⁵⁴

Application of these IS methods and models to DSC⁵¹ showed that IS provides a picture of the energetics of TiO_2 , which is a crucial tool for comparing different DSC

configurations.⁵⁵ It also showed that it was possible to obtain simultaneously the parameters for transport and recombination at different steady-state conditions of a DSC, which is an unsurpassed power of the technique. The trends of the electron diffusion coefficient⁵¹ were similar to those found previously by L. M. Peter and coworkers by light-modulated techniques.⁵⁶ The electron lifetime derived from IS measurements was also consistent⁵⁵ with that obtained from open-circuit voltage decays.^{54,57} The variation of parameters with the bias voltage (correspondent to the electron Fermi level) observed by IS and other methods was related to multiple trapping characteristics in an exponential distribution of states.^{33,58} This subject has been recently summarized in review articles.⁵⁹⁻⁶¹

The consistency of the different experimental methods provided a great confidence of the significance of modeling and experimental tools. The usefulness of IS for DSC characterization became apparent, since IS allows a full picture of the different device aspects to be obtained.^{18,19} Several groups presented detailed and systematic IS characterization of DSC.⁶²⁻⁶⁴ The literature of papers applying IS in DSC is very large and we do not aim to cite all the contributions. We highlight a paper on high efficiency DSC⁶⁵ that provides excellent examples of diffusion-recombination impedances, a full analysis of electron transport data, as well as the reconstruction of the current density-potential ($j-V$) curve from the resistance obtained by IS. Subsequently, IS has been applied in different and important configurations of DSC, such as those using ionic liquids,⁶⁶ ordered TiO₂ nanotubes,⁶⁷ and solid hole conductor.⁶⁸

2. A basic solar cell model

2.1. The ideal diode model

Many general aspects of solar cell operation can be understood starting with an ideal model that represents optimal performance. Fig. 3(a) shows the steady-state characteristic $j-V$ curve of a solar cell. This curve was drawn using the ideal diode model:

$$j = j_{sc} - j_d \left(e^{qV/mk_B T} - 1 \right) \quad (1)$$

Here j is the electrical current density, V is the voltage difference between the contacts, j_{sc} the short-circuit current density, j_d the dark reverse current density, q is the positive elementary electrical charge, k_B is Boltzmann's constant and T the absolute temperature. The coefficient m is an ideality factor, the "ideal" model being for $m = 1$.

From Eq. (1) we obtain the open-circuit voltage V_{oc} :

$$V_{oc} = \frac{mk_B T}{q} \ln \left(1 + \frac{j_{sc}}{j_d} \right) \quad (2)$$

and we can also write Eq. (1) in terms of V_{oc}

$$j = j_{sc} \frac{1 - e^{q(V - V_{oc})/mk_B T}}{1 - e^{-qV_{oc}/mk_B T}} \quad (3)$$

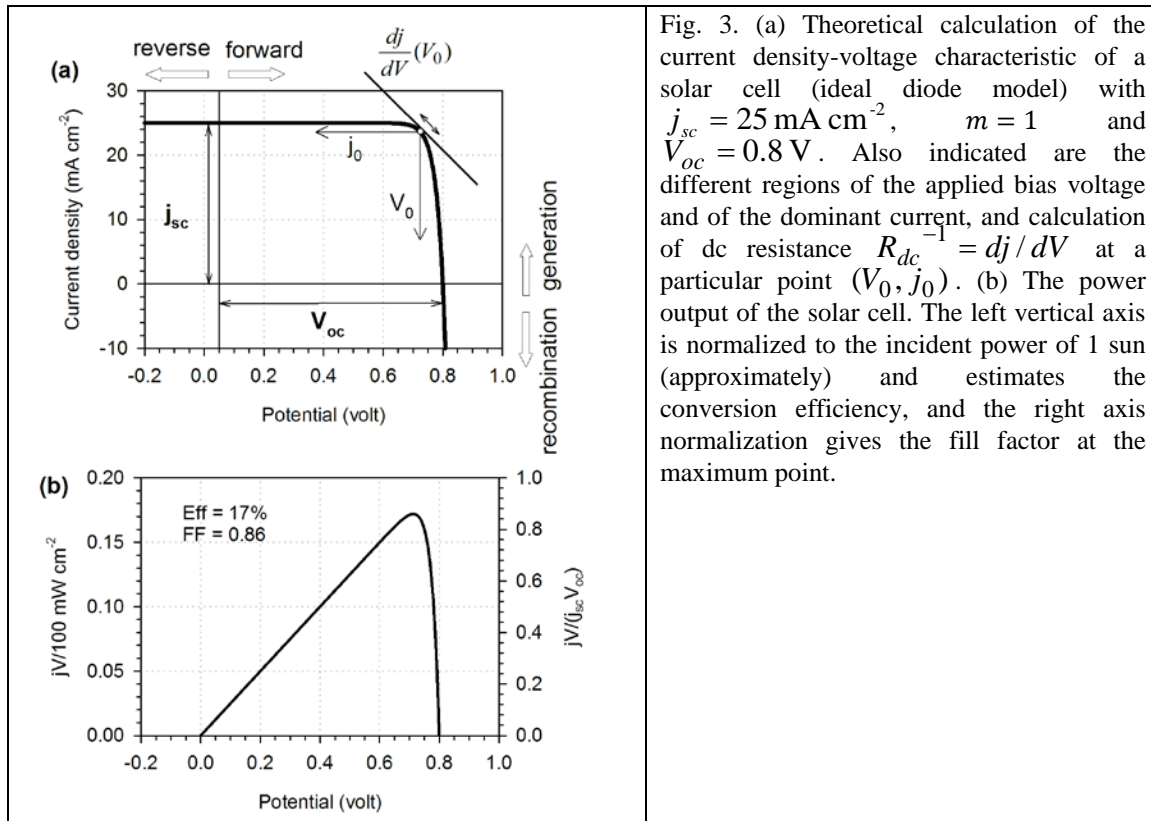


Fig. 3. (a) Theoretical calculation of the current density-voltage characteristic of a solar cell (ideal diode model) with $j_{sc} = 25 \text{ mA cm}^{-2}$, $m = 1$ and $V_{oc} = 0.8 \text{ V}$. Also indicated are the different regions of the applied bias voltage and of the dominant current, and calculation of dc resistance $R_{dc}^{-1} = dj/dV$ at a particular point (V_0, j_0) . (b) The power output of the solar cell. The left vertical axis is normalized to the incident power of 1 sun (approximately) and estimates the conversion efficiency, and the right axis normalization gives the fill factor at the maximum point.

Bias voltage is denoted “forward” when it injects charge in the solar cell and induces recombination, and otherwise “reverse”. Changing the illumination intensity Φ_0 , one can trace different curves similar to Fig. 3(a) with other values of j_{sc} and V_{oc} . The values and shape of these curves for a given solar cell allow us to determine the energy conversion efficiency of the photovoltaic device, Fig. 3(b). Another crucial parameter is the fill factor (FF), which is the maximum electrical power delivered by the cell with respect to $j_{sc} \cdot V_{oc}$, Fig. 3(b). A high FF requires that the current remains high at the maximum power point. This is obtained if the j-V curve is reasonably “squared” as in Fig. 3(a).

2.2. Physical origin of the diode equation for a solar cell

It is important to clarify the physical interpretation of the diode equation. We consider a slab of p-type semiconductor with thickness L . At position x , n is the density of minority carriers (electrons), and J_n the flux in the positive x direction. The conservation equation is

$$\frac{\partial n}{\partial t}(x) = G_{\Phi}(x) + G_d(x) - \frac{\partial J_n}{\partial x}(x) - U_n(x) \quad (4)$$

In Eq. (4) G_{Φ} is the rate of optical photogeneration (per unit volume) due to the illumination intensity Φ_0 (photons·cm⁻²), while G_d is the rate of generation in the dark by the surrounding blackbody radiation. U_n is the rate of recombination of electrons per volume. A simple and important model is the linear form, with electron lifetime τ_0

$$U_n = \frac{n}{\tau_0} \quad (5)$$

Eq. (4) must hold locally, in equilibrium, therefore, assuming Eq. (5), we have

$$G_d = \frac{n_0}{\tau_0} \quad (6)$$

where n_0 is the carrier density in dark equilibrium. This is because in dark equilibrium, by detailed balance principle, the rate of generation equilibrates the recombination rate.³¹ A similar constraint on G_d applies for any recombination model.

The flux of electron carriers with the diffusion coefficient D_0 relates to the gradient of concentration by Fick's law

$$J_n = -D_0 \frac{\partial n}{\partial x} \quad (7)$$

While Eq. (4) can be solved for any kind of generation profile and boundary conditions, we now adopt some assumptions that lead to the central diode model (1) in the simplest way. We assume that the photogeneration of carriers is homogeneous, and we consider that the transport of electrons is very fast. Thus we assume that D_0 is very large implying that the gradient of concentration required to maintain the flux is very small. With these assumptions all the quantities in Eq. (4), except the carrier flux, become independent of position. We now integrate between $0 \leq x \leq L$ and we obtain

$$\frac{\partial n}{\partial t} = G_{\Phi} + G_d - \frac{1}{L}[J_n(L) - J_n(0)] - U_n \quad (8)$$

The next condition we need is to assume that the semiconductor is supplemented with ideal selective contacts to form a solar cell, as shown in Fig. 4.³³ Thus the left contact extracts all the arriving electron carriers.

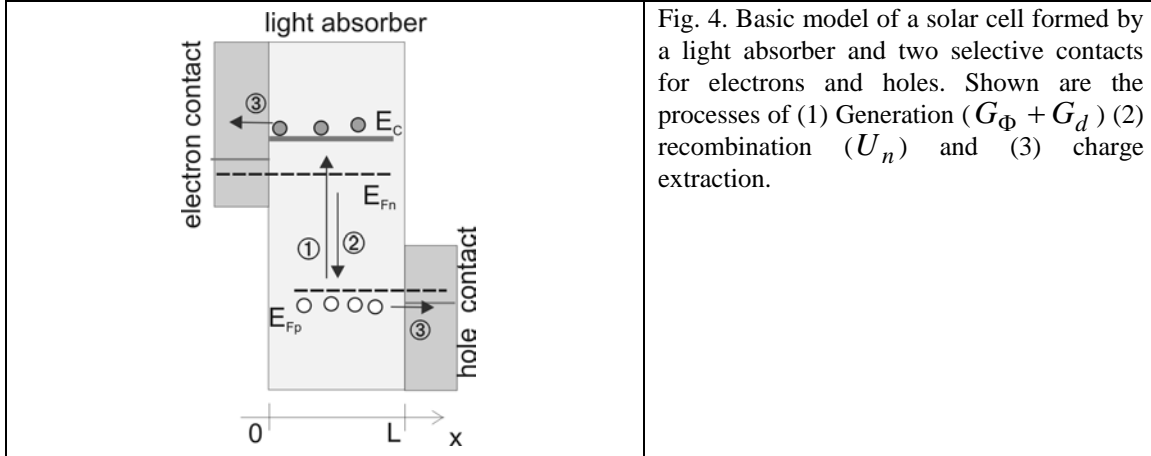


Fig. 4. Basic model of a solar cell formed by a light absorber and two selective contacts for electrons and holes. Shown are the processes of (1) Generation ($G_{\Phi} + G_d$) (2) recombination (U_n) and (3) charge extraction.

The electrical current density in the positive x direction is

$$j = -qJ_n(0) \quad (9)$$

and the right contact is perfectly blocking to electrons:

$$J_n(L) = 0 \quad (10)$$

Therefore, the output current at time t is:

$$j = qL \left[G_{\Phi} + G_d - U_n - \frac{\partial n}{\partial t} \right] \quad (11)$$

If we restrict our attention to *steady-state* condition, Eq. (11) reduces to

$$j = qLG_{\Phi} - qL[U_n - G_d] \quad (12)$$

Comparing Eqs. (1) and (12) we obtain that the photocurrent generated at short-circuit is

$$j_{sc} = qLG_{\Phi} \quad (13)$$

The total generation per unit area, LG_{Φ} , is proportional to the incident light intensity, $LG_{\Phi} = \eta_{opt} \Phi_0$, where η_{opt} is an optical quantum yield, that depends on the properties of absorption of the radiation by the solar cell. We also obtain that

$$j_d = qLG_d \quad (14)$$

Therefore the dark reverse current corresponds to the extraction of the carriers generated by the thermal surrounding radiation.

We already appreciate that the ideal diode model of a solar cell, states that a constant current is drawn out of the cell, namely $j_{sc} + j_d$, corresponding to *all* the electron carriers generated in the semiconductor. In addition, the recombination term produces a current in the opposite direction. At high forward bias the recombination term dominates and bends the $j-V$ curve, as it is indicated in Fig. 3(a). Note that this ideal model does not contain any trace of diffusion at all. The only necessary element to obtain the diode model is to state that the contacts are selective and extract only one carrier at each side, as indicated in Fig. 4.

Another step to convert the conservation equation into a $j-V$ characteristic is to relate the carrier density n to the applied voltage V by means of the introduction of Fermi levels. We assume the extended states for electrons at the level E_c (conduction band edge), with effective density N_c . With respect to the electron Fermi level E_{Fn} , we have

$$n = N_c e^{(E_{Fn}-E_c)/k_B T} \quad (15)$$

and considering the dark (equilibrium) Fermi level E_{F0}

$$n_0 = N_c e^{(E_{F0}-E_c)/k_B T} \quad (16)$$

we obtain

$$n = n_0 e^{(E_{Fn}-E_{F0})/k_B T} \quad (17)$$

The voltage V is measured at the selective contacts, and corresponds to the difference of Fermi levels of carriers at the contacts. If the contacts are ideally reversible,³³ each contact separately equilibrates with the Fermi level of electrons, E_{Fn} , and holes, E_{Fp} , therefore we have

$$V = (E_{Fn} - E_{Fp}) / q \quad (18)$$

For a p-semiconductor the holes Fermi level remains at the dark equilibrium level, $E_{Fp} = E_{F0}$, and so Eq. (18) can be written

$$E_{Fn} = E_{F0} + qV \quad (19)$$

In consequence

$$n = n_0 e^{qV/k_B T} \quad (20)$$

Using the linear recombination of Eq. (5) in Eq. (12), and applying the Boltzmann statistics indicated in Eq. (20), we obtain the diode equation (1) with $m = 1$. But if we assume a *nonlinear* recombination model, more general than that used previously

$$U_n = k_r n^\beta \quad (21)$$

we obtain the general diode equation with $m = 1/\beta$. Here, Eq. (21) is written as a purely empirical law but its origin will be further discussed below.

It should be noted that the recombination mechanism has a major impact in the shape of $j - V$ curve, especially on the FF, and therefore on the solar cell conversion efficiency. In fact, as we have shown with the above model, for ideal selective contacts, the diode ideality factor m is entirely determined by the bulk recombination mechanism. This point is well understood in solid-state electronics.⁶⁹

3. Introduction to IS methods

In general, IS is applied in a system with electrical contacts. It consists on the measurement of the ac electrical current $\hat{I}(\omega)$ at a certain angular frequency ω , when a certain ac voltage $\hat{V}(\omega)$ is applied to the system, or vice versa, measurement of $\hat{V}(\omega)$ at applied $\hat{I}(\omega)$. The impedance is

$$Z(\omega) = \frac{\hat{V}(\omega)}{\hat{I}(\omega)} \quad (22)$$

The symbol \hat{x} over a quantity x indicates that \hat{x} has the following properties. It is

- (1) the complex amplitude of a sinusoidal (ac) perturbation of x and
- (2) a small perturbation.

The ‘‘smallness’’ of \hat{x} is required in order to obtain in Eq. (22) the *linear* impedance, i.e., $\hat{I}(\omega)$ is linear with respect to $\hat{V}(\omega)$, or vice versa, so that $Z(\omega)$ is independent of the amplitude of the perturbation. In modeling work, this is ensured if the absolute value of \hat{x} is much less than that of the steady state quantities \bar{x} , \bar{y} , ... In practice this means that the amplitude of the voltage must be of the order of several mV. However in some situations, e.g. close to a phase transition, a small perturbation of voltage induces very large variations of charge or current, and the conditions of linearity must be carefully inquired.

In the impedance measurement the system is (ideally) kept at a fixed steady state by imposing stationary constraints such as dc current, illumination intensity, etc., and the $Z(\omega)$ is measured scanning the frequency at many values $f = \omega/2\pi$, typically over several decades, i.e. from mHz to 10 MHz, with 5-10 measurements per decade. At each frequency the impedance meter must check that the $Z(\omega)$ is stable. At low frequencies this takes considerable time, i.e., stabilizing a measurement at $f = 10$ mHz consumes

minutes. But measurement at low frequencies is often important in order to check that one is approaching the dc regime, as further explained below. So judicious selection of the frequency window of measurement is necessary, and this is often aided by experience.

In addition to scanning the frequencies, it is usually very important to determine the IS parameters at different conditions of steady state. This is the key approach in order to relate the measurement to a given physical model. At each steady state the $Z(\omega)$ data is related to a model in the *frequency* domain, which usually is represented as an equivalent circuit. By changing the steady state, the change of impedance parameters (resistances, capacitances, etc.) can be monitored in relation to the physical properties of the system. Since the impedance measurement takes considerable time, it is often the case that the steady state *changes* along the impedance measurement, and precautions should be taken to avoid a serious drift of the parameters. In particular, care should be taken with unintentional changes of temperature in solar cells, since this introduces additional and unwanted variation of parameters.

Note that at each steady state a full scan of frequencies is necessary. Thus many steady state points imply a long measurement, perhaps a whole day. However, data that do not cover different steady states may be in some cases of little value, if there is uncertainty about the meaning of the parameters. It is also important to check the true significance of parameters by materials variation of the samples, e.g., to confirm the correlation of a transport resistance with the reciprocal length of the sample. The extent to which these approaches must be realized judiciously depends on preliminary knowledge and experience about the particular system.

3.2. Steady state and small perturbation quantities

As an example of the relationship between ac impedance and steady-state quantities, we discuss a characteristic experiment on a solar cell using the ideal model outlined above in Figs. 3 and 4. We choose a certain point of bias voltage V_0 with the associated current density j_0 . At this point, a small displacement of voltage $\hat{V}(\omega)$ implies a change of current $\hat{j}(\omega)$. The value $\omega = 0$ in parenthesis indicates that the displacement is infinitely slow, i.e., $\hat{V}(0)$ and $\hat{j}(0)$ attain a value that is independent of time. The displacement of the current and voltage is indicated in Fig. 3(a) with arrows.

For a solar cell with area A the quotient of the small quantities gives

$$Z(0) = \frac{\hat{V}(0)}{A\hat{j}(0)} = \left(\frac{Adj}{dV} \right)^{-1} = R_{dc} \quad (23)$$

That is, the small quantities give a derivative of voltage with respect to current. This is the reciprocal of the slope of the $j - V$ curve, which is in turn the dc resistance of the solar cell R_{dc} (per area) in those particular conditions.

A similar process occurs if we measure the modification of electrical charge \hat{Q} under a perturbation of the voltage. The quotient is a capacitance

$$\frac{\hat{Q}(0)}{\hat{V}(0)} = \frac{dQ}{dV} = C \quad (24)$$

In general the parameters obtained by IS are related to derivatives of the steady state variables describing the system, i.e., IS gives differential resistance, differential capacitance, etc. But we usually omit the specification of “differential” in the context of IS; it is implicitly assumed.

It is useful to observe that, since R_{dc} is the reciprocal of the slope of the current density-potential curve, Fig. 3(a), knowledge of R_{dc} at several points allows us to construct the full curve, provided that a single point of the curve is known (for example, the value of j_{sc}):

$$j(V) = j_{sc} - \int_0^V R_{dc}^{-1} dV \quad (25)$$

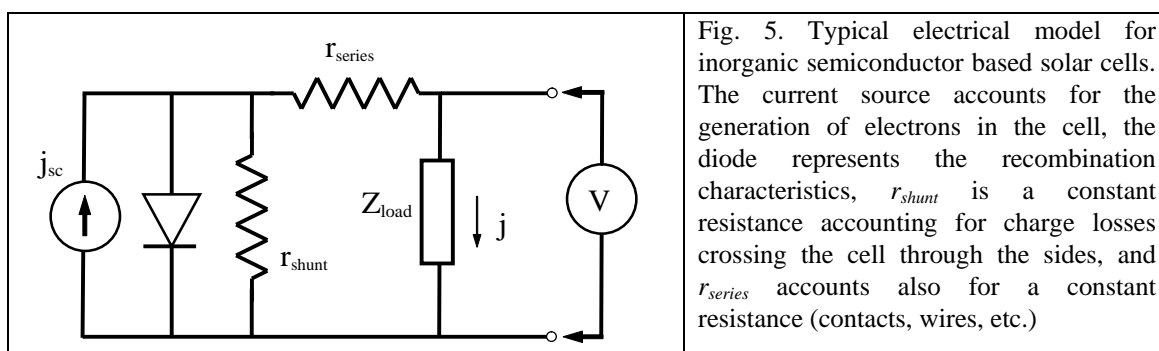
Therefore, understanding the different elements that determine R_{dc} is a key step for analyzing the factors governing the efficiency of the solar cell.

From the steady state characteristic we can only derive $Z(0)$, that is, the impedance at the frequency $\omega = 0$. But in order to understand the operation of the solar cell we wish to know which is the origin of R_{dc} in terms of the internal processes occurring in the device: transport of charges, accumulation at certain points, recombination of carriers, and so on. Eventually we are interested also in the dynamic behavior of the solar cell, i.e., how it responds with time to a certain perturbation.

One way to obtain the dc parameters of the solar cell is to apply a certain model of steady state operation. This can be done by an equivalent circuit that describes dc current distribution, including diode elements. This is different to ac equivalent circuits for IS spectra that will be amply discussed below. In fact since the diode *is not* a linear impedance, thus it is not a differential element in the sense explained previously.

In particular a dc model including an ideal diode, shunt resistance r_{shunt} , and series

resistance r_{series} is amply used in this context, see Fig. 5.^{70,71} This procedure normally assumes that r_{shunt} and r_{series} are *independent* of voltage along the $j-V$ characteristics. This assumption may work well in some classes of solar cells such as monocrystalline Si solar cells. But in other cases, especially in devices including electrochemical processes such as in DSC, it is far from clear that resistances remain constant, even at reverse voltage. Great care should be taken with applying dc models to DSC, since one may impose a model that does not occur in the device and the results may have little meaning.



We will see later how to construct a dc model that is normally useful for the analysis of DSC, but first we need to discuss the origin of the elements that appear in equivalent circuits. To this end we describe a much more powerful approach, applying IS, to obtain all the stationary and dynamic information about the current-voltage behavior of the system.

3.3. The frequency domain

In general, the method of IS, consists on measuring the quotient in Eq. (22) when the signal $\hat{V}(\omega)$ varies at different angular velocities. When the velocity ω is very slow, we are close to the steady state conditions and we obtain exactly the dc resistance as indicated in Eq. (23). But when ω becomes faster, some processes in the system are not able to respond to the applied perturbation. Therefore $Z(\omega)$ contains contributions from “things faster than” ω .

By scanning the frequency we obtain a changing response (the impedance spectrum) that can be treated by several methods (analytical, numerical, and importantly, by visual inspection of the shape of the response) in order to provide a detailed physical picture on the dynamic properties of the system. In particular, it is very important for solar cell

applications that this method allows to dissect the steady-state response into its elementary components. A vivid explanation of the physics and interpretation of the electrical magnitudes in the frequency domain for dielectric materials is given in the book “Dielectric Relaxation in Solids” by A. K. Jonscher.⁷²

One may wonder why to use so many different angular frequencies in the measurement, when the same processes can be probed by time transients, i.e. applying a voltage step and monitoring the subsequent evolution towards equilibrium. One could therefore observe the fast and progressively slower processes in the system, in a similar fashion as by the variation of the frequency of the perturbation.

Indeed, time transient methods are very important experimental tools, and *mathematically*, small amplitude time transients contain the same information as the small frequency linear impedance. Both are related by the operation of Laplace transform. Indeed, when the decay of the system is governed by a single process (usually an exponential decay, with a characteristic time constant τ), IS and time transients are equally valid approaches. The difference arises when the response is composed by a combination of processes. Then it turns out that it is much easier to deconvolute the response, in terms of models, from the spectroscopic response $Z(\omega)$ than from the much featureless time-dependent signal.

As another example of the advantages of the frequency domain, let us find the kinetic response of the capacitance that was derived in equilibrium conditions in Eq. (24). In the time domain we apply a small step of the voltage $\hat{V}(t) = \Delta V \cdot u(t)$, being $u(t)$ the unit step function at $t = 0$, and we observe the consequent evolution of the charge $\hat{Q}(t)$ that passes to the system. However, it is not usually feasible to measure a charge transient, thus we need to observe the current transient $\hat{I}(t)$ and perform an integration:

$$\hat{Q}(t) = \int_0^t \hat{I}(t') dt' \quad (26)$$

Let us look at this process in the frequency domain. We use the variable $s = i\omega$, being $i = \sqrt{-1}$. The Laplace-transformation of a function $f(t)$ to the frequency domain is defined as

$$F(s) = \int_0^\infty e^{-st} f(t) dt \quad (27)$$

Application of the transform to Eq. (26) gives

$$\hat{Q}(s) = \frac{\hat{I}(s)}{s} \quad (28)$$

Now we introduce a frequency-dependent capacitance that generalizes Eq. (24)

$$C^*(\omega) = \frac{\hat{Q}(\omega)}{\hat{V}(\omega)} \quad (29)$$

$C^*(\omega)$ is a function of the frequency, that coincides with the static differential capacitance C at $\omega = 0$. Applying Eq. (22) we obtain from (28)

$$C^*(\omega) = \frac{\hat{I}(\omega)}{i\omega\hat{V}(\omega)} = \frac{1}{i\omega Z(\omega)} \quad (30)$$

This result shows that it is straightforward to resolve the small step charging experiment if the impedance is known. We observe in Eq. (30) that the conversion of impedance data to capacitance turns out to be a very simple operation. This simplicity of conversion between very different electrical magnitudes appears because of the convenient properties of complex numbers, and by the fact that in the frequency domain, derivatives and integrals consist on arithmetic operations involving s .

Switching the data between different representation is a very useful tool of analysis in IS. The most frequently used functions are described in Table 1,⁷³ indicating also the separation of the magnitudes in real and imaginary part.

Table 1. Impedance representations

Denomination	Definition*	Real and imaginary parts
Impedance	$Z(\omega)$	$Z = Z' + iZ''$
Admittance	$Y(\omega) = \frac{1}{Z(\omega)}$	$Y = Y' + iY''$
Phase angle	$\tan \delta = \frac{Z''}{Z'}$	
Complex capacitance	$C^*(\omega) = \frac{1}{i\omega Z(\omega)}$	$C^* = C' + iC''$
Conductivity	$\sigma^*(\omega) = \frac{L}{AZ(\omega)}$	$\sigma^* = \sigma' + i\sigma''$, $\sigma'(0) \equiv \sigma$
Complex dielectric constant	$\varepsilon^*(\omega) = LC^*(\omega) / A$	$\varepsilon^* = \varepsilon' + i\varepsilon''$ $\sigma^* = i\omega\varepsilon^*$

Complex electric modulus	$M^*(\omega) = \frac{1}{\varepsilon(\omega)}$	$M^* = M' + iM''$
--------------------------	---	-------------------

(*) L is the length of the sample, A the area.

3.4. Simple equivalent circuits

Many measurements of IS in electrochemistry and materials devices can be described by equivalent circuits composed by combinations of a few elements, that are indicated in Table 2. Equivalent circuits are formed by the connection of these and other elements by wires, that represent low resistance paths in the system. Two elements are in series when the current through them is the same, and are in parallel when the voltage acting on them is the same. Using Kirchhoff rules, we add the impedances for two elements in series and the resulting impedance is an equivalent description of the initial connection (it produces the same current under applied voltage as the combination that it replaces). For elements in parallel we add the admittances (or the complex capacitances) to form the equivalent impedance.

Table 2. Basic ac electrical elements

Denomination	Symbol	Scheme	Impedance
Resistance	R		R
Capacitance	C		$\frac{1}{i\omega C}$
Inductor	L		$i\omega L$
Constant phase element (CPE)	Q_n		$\frac{(i\omega)^{-n}}{Q_n}$

A first example of equivalent circuit is the R_1C_1 series combination. From the impedance

$$Z(\omega) = R_1 + \frac{1}{i\omega C_1} \quad (31)$$

we obtain the complex capacitance

$$C^*(\omega) = \frac{C_1}{1 + i\omega\tau_1} \quad (32)$$

where the relaxation time is defined as

$$\tau = R_1 C_1 \quad (33)$$

Let us look more closely at the meaning of the relaxation time τ_1 in relation to the response of the system in the time domain. We consider the type of measurement commented before in which a change of voltage ΔV is applied at time $t = 0$ and the subsequent evolution of the electrical current is monitored. In the frequency domain the step voltage $\hat{V}(t) = \Delta V \cdot u(t)$ has the expression

$$\hat{V}(s) = \frac{\Delta V}{s} \quad (34)$$

and the electrical current is

$$\hat{I}(s) = \frac{\hat{V}(s)}{Z(s)} = \frac{\Delta V}{sZ(s)} = \frac{\tau_1 \Delta V}{R_1(1 + s\tau_1)} \quad (35)$$

Inverting Eq. (35) to the time domain we obtain

$$I(t) = \frac{\Delta V}{R} e^{-t/\tau_1} \quad (36)$$

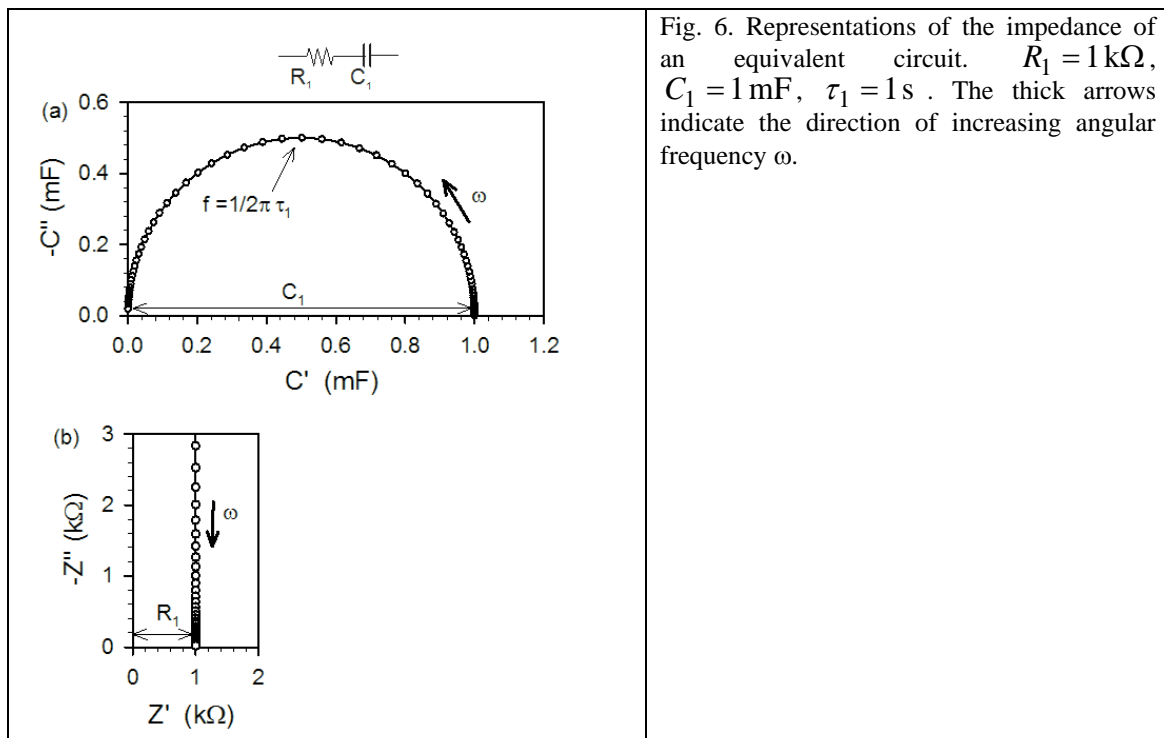


Fig. 6. Representations of the impedance of an equivalent circuit. $R_1 = 1 \text{ k}\Omega$, $C_1 = 1 \text{ mF}$, $\tau_1 = 1 \text{ s}$. The thick arrows indicate the direction of increasing angular frequency ω .

In general the process described by Eqs. (32) or (36) is an elementary relaxation with the characteristic frequency

$$\omega_1 = \frac{1}{\tau_1} = \frac{1}{R_1 C_1} \quad (37)$$

The plot of the complex capacitance is shown in Fig. 6(a). The capacitance displays an arc from the dc value $C^*(0) = C_1$ to the high frequency value. The top of the arc occurs at the characteristic frequency of the relaxation ω_1 . The impedance, shown in the complex plane in Fig. 6(b), forms a vertical line. This is a “blocking” circuit, since the impedance of a capacitor is ∞ at low frequency, and effectively constitutes an open circuit connection, so dc current cannot flow. But the impedance of the capacitor decreases as the frequency increases. At very large frequencies, with respect to ω_1 , the capacitor becomes effectively a short-circuit. So there remains only the resistance R_1 . The impedance of a resistor is the same at all frequencies, hence the vertical line in Fig. 6(b). The arc in Fig. 6(a) is the manifestation of an elementary relaxation process that corresponds to an exponential decay in the time domain, indicated in Eq. (36).

Another important example of equivalent circuit is the RC parallel combination, Fig. 7. The admittance of the combination is

$$Y_1(\omega) = \frac{1}{R_1} + i\omega C_1 \quad (38)$$

With the addition of a series resistance R_2 we obtain the circuit shown in Fig. 7. The impedance is

$$Z(\omega) = R_2 + Y_1 = R_2 + \frac{R_1}{1 + i\omega\tau_1} \quad (39)$$

The complex impedance plot is shown in Fig. 7(a). The parallel RC forms an arc in the complex plane that is shifted positively along the real axis by the series resistance, R_2 . As we remarked before, at zero frequency the capacitor can be substituted by open-circuit connection. In contrast to Fig. 6, we observe in Fig. 7 that this is a circuit with dc conduction determined by the low frequency intercept, $Z(0) = R_{dc} = R_1 + R_2$.

In Fig. 7(a) the three plots correspond to a variation of the parallel resistance, which implies a change of the characteristic time $\tau_1 = R_1 C_1$. In the complex plane we readily infer the structure of the circuit from the shape of the spectra, but frequency values and time scales cannot be directly read. To this end it is useful to apply the plot with respect to frequency (sometimes termed a Bode plot). Fig. 7(b) shows the transition of the resistance from the low frequency (R_{dc}) to the high frequency value (R_2). This high frequency value occurs by the fact that the capacitor impedance disappears at very high

frequency, $Z(\omega = \infty) = 0$, and shunts the parallel resistance. Another representation often used to display the characteristic frequencies is the phase angle. Fig. 7(c) shows that the peak of phase angle moves to higher frequencies when τ_1 decreases.

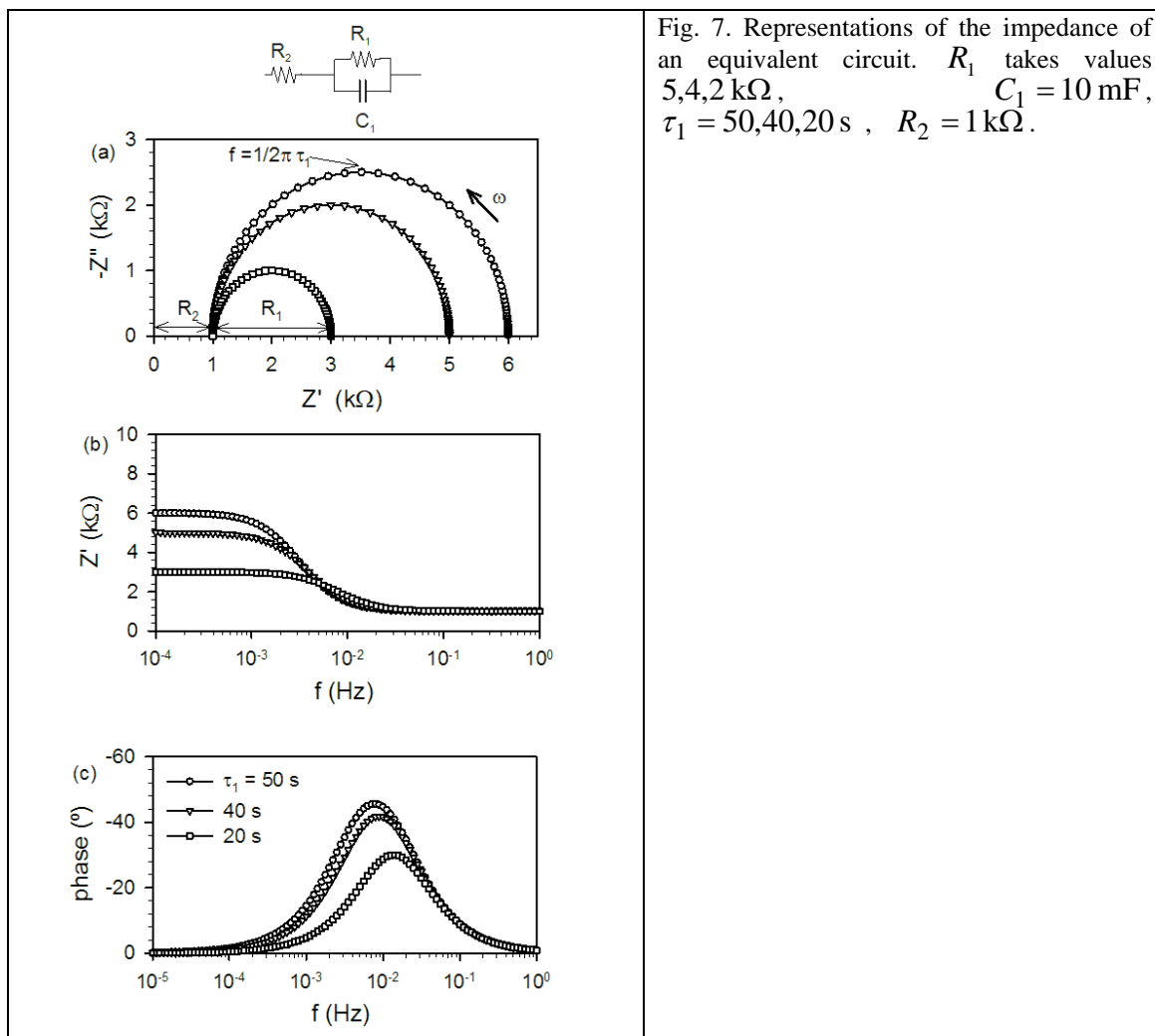


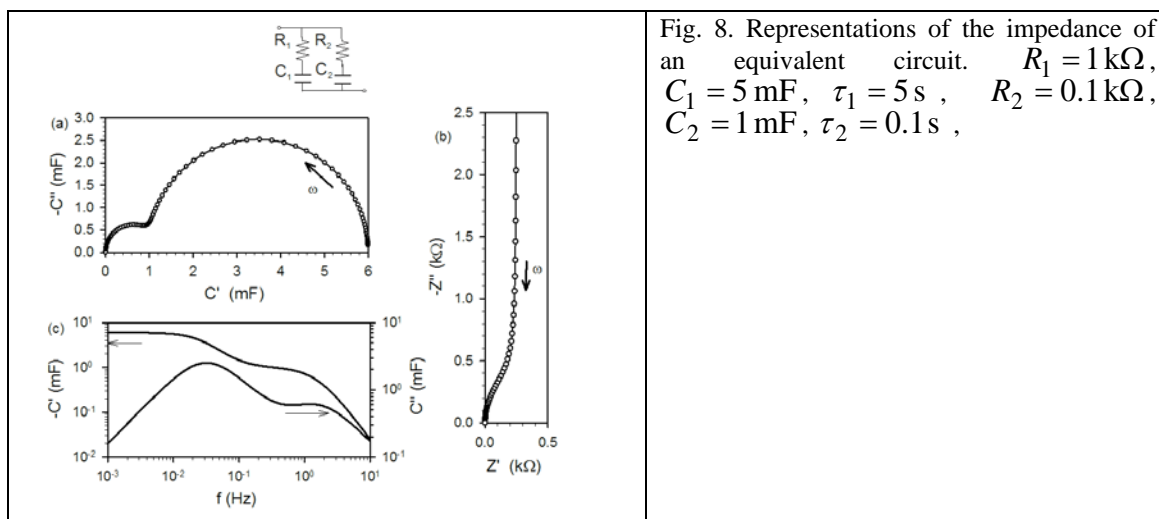
Fig. 7. Representations of the impedance of an equivalent circuit. R_1 takes values 5,4,2 k Ω , $C_1 = 10$ mF, $\tau_1 = 50,40,20$ s, $R_2 = 1$ k Ω .

In measurement of material systems it is rather frequent that the IS response is composed of the combination of several processes. The time constants, and the connection of the elements describing such processes, depend on the internal structure of the system. A primary aim of the data analysis is to identify the contribution of separate relaxation processes in the frequency response of the system and such aim is greatly assisted by picking the appropriate form of data display. In IS measurement we obtain the data, and such data we may transform as desired between the different representations of Table 1.

As we remarked in a previous section, the most critical information concerning solar

cell device operation in stationary conditions relates to the separation of resistances. However, in IS capacitances also play a crucial role, since different elements with similar resistance, provide very distinct spectral features if their associated capacitances sufficiently differ in magnitude. The capacitance is, therefore, a key to the understanding of the origin of the measured resistances.

Fig. 8 shows the example of a system composed of several relaxations represented by two series RC circuits connected in parallel. This circuit is relevant for the analysis of multiple-trap systems in electronic materials.^{74,75} Inspection of the complex impedance plane in Fig. 8(b) only shows the blocking response at low frequencies and an additional feature at high frequency. For a blocking circuit it is natural to analyze the capacitance, and the plot of the capacitance components with respect to the frequency, Fig. 8(c), usually reveals a great deal of information. In Fig. 8(c) we observe two plateaus of the real part of the capacitance that clearly indicate two distinct relaxation processes. These relaxations are manifest in the peaks of the loss component of the capacitance, C'' . When increasing the frequency, each peak of C'' indicates the occurrence of a relaxation and a consequent decrease of the capacitance.⁷² These features can be observed also in the complex capacitance plot in Fig. 8(a), that show separate arcs for the two relaxations.



Let us consider in more detail how to obtain the parameters of a given IS data set. The main method is the fitting by least squares methods using equivalent circuit software that is available in many kinds of measurement equipments. But the fitting

process requires the assumption of a given equivalent circuit, and sometimes, in addition, the input of reasonable trial parameters. As we have mentioned before, inspection of the data set in several complementary representations usually gives a good hint of the equivalent circuit structure, at least in the less complex cases. Another useful approach is to read the values of parameters *directly* from the data representation, e.g. resistances and capacitances of separate contributions, and this can be done as already discussed in the examples of Fig. 7(b) and 8(c). However, the values of capacitance or impedance in a certain frequency domain can be influenced by the whole equivalent circuit. So to obtain the circuit parameters, in many occasions there is no substitute for *integral* data fitting. Treating separately a part of the spectral data is a valuable resource but must be used with care.

For example, in Fig. 7(a) we observe that when approaching the dc limit, the impedance displays a vertical line. Therefore, at low frequency Fig. 7(a) can be simply described by RC parallel combination. The low frequency resistance is clearly given by R_{dc} . But what should be the low frequency capacitance C_{lf} ? It cannot be C_1 , otherwise the arc would finish in the origin of Fig. 7(a), and it doesn't. In general it is very useful to obtain the impedance formula in a restricted frequency domain, and we show the method with this example.

First, from the expression of the impedance in Eq. (39) we find the low frequency limit which gives

$$Z(\omega) = R_1 + R_2 + i\omega R_1^2 C_1 \quad (40)$$

This last equation does not correspond to any recognizable circuit elements combination. In fact we are looking for a *parallel* combination, which should describe well the data in Fig. 7(a) at low frequencies, thus we transform Eq. (40) to the admittance, maintaining the first order approximation in ω , with the result

$$Y(\omega) = \frac{1}{R_1 + R_2} + i\omega \frac{R_1^2}{(R_1 + R_2)^2} C_1 \quad (41)$$

In Eq. (41) we readily recognize the parallel RC admittance formula. The low frequency capacitance is

$$C_{lf} = \frac{R_1^2}{(R_1 + R_2)^2} C_1 \quad (42)$$

Therefore the capacitance depends on the resistances of the original circuit. This

result is quite natural, since the capacitance relates to the reciprocal of the impedance (see Table 1), and the later is greatly influenced by the series resistance. However, the result in Eq. (42) cannot be inferred without a proper calculation.

Let us continue with the analysis of the effect of different types of equivalent circuit elements. While the combination of resistances and capacitors provide a spectra that remains in the first quadrant of the complex impedance plane, it is not uncommon to find that the data cross to the fourth quadrant. One reason for this is the inductance of the leads, which very frequently causes a tail at high frequencies in which the spectrum crosses the real axis. A different feature is often found in several types of solar cells at *low frequency*, consisting on a loop that forms an arc in the fourth quadrant.⁷⁶ One of the representations of this effect is a series RL branch complementing the RC circuit of Fig. 7. The model is shown in Fig. 9, and the total admittance has the value

$$Y(\omega) = \frac{1}{R_1} + \frac{1}{R_3 - i\omega L_3} + i\omega C_1 \quad (43)$$

The low frequency limit of Eq. (43) is

$$Y(\omega) = \frac{1}{R_0} + i\omega \left(C_1 - \frac{L_3}{R_3^2} \right) \quad (44)$$

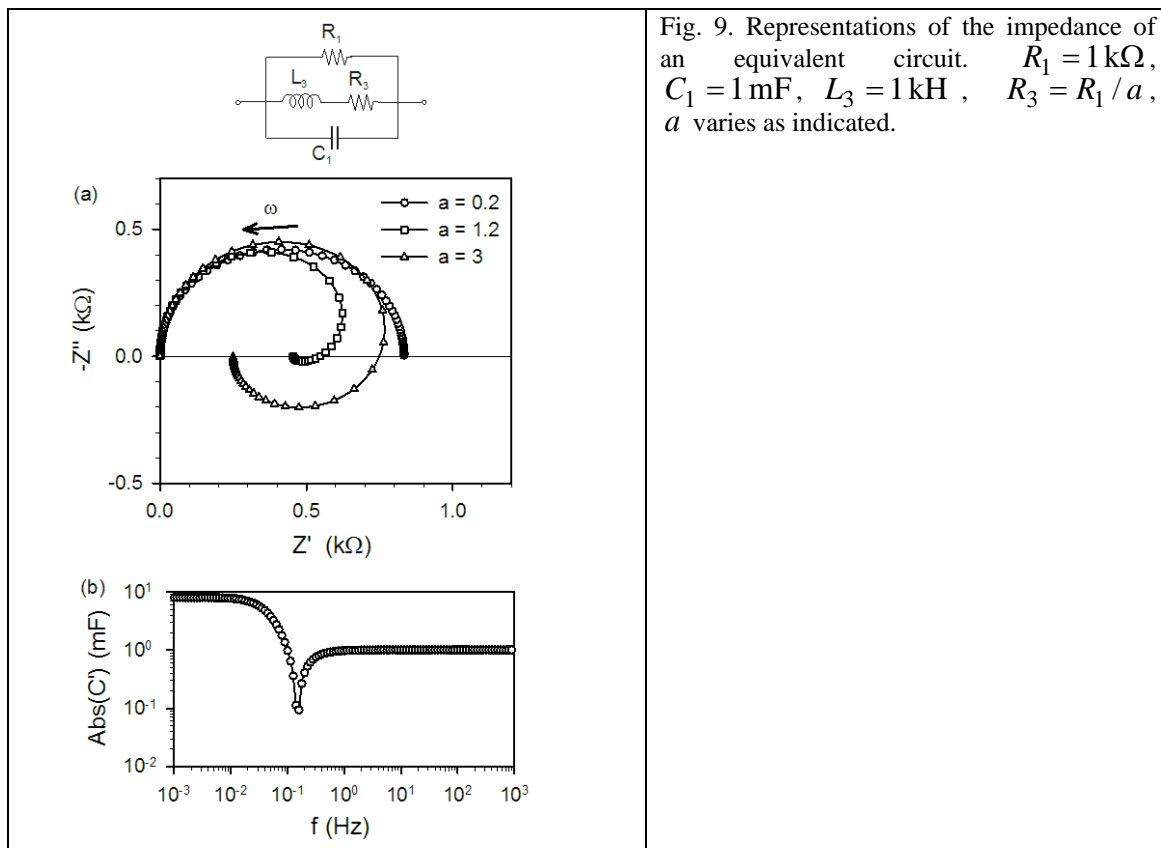


Fig. 9. Representations of the impedance of an equivalent circuit. $R_1 = 1 \text{ k}\Omega$, $C_1 = 1 \text{ mF}$, $L_3 = 1 \text{ kH}$, $R_3 = R_1 / a$, a varies as indicated.

Eq. (44) shows that when R_3 is small, the capacitance becomes negative at low frequencies, $C = -C_N$ with the value

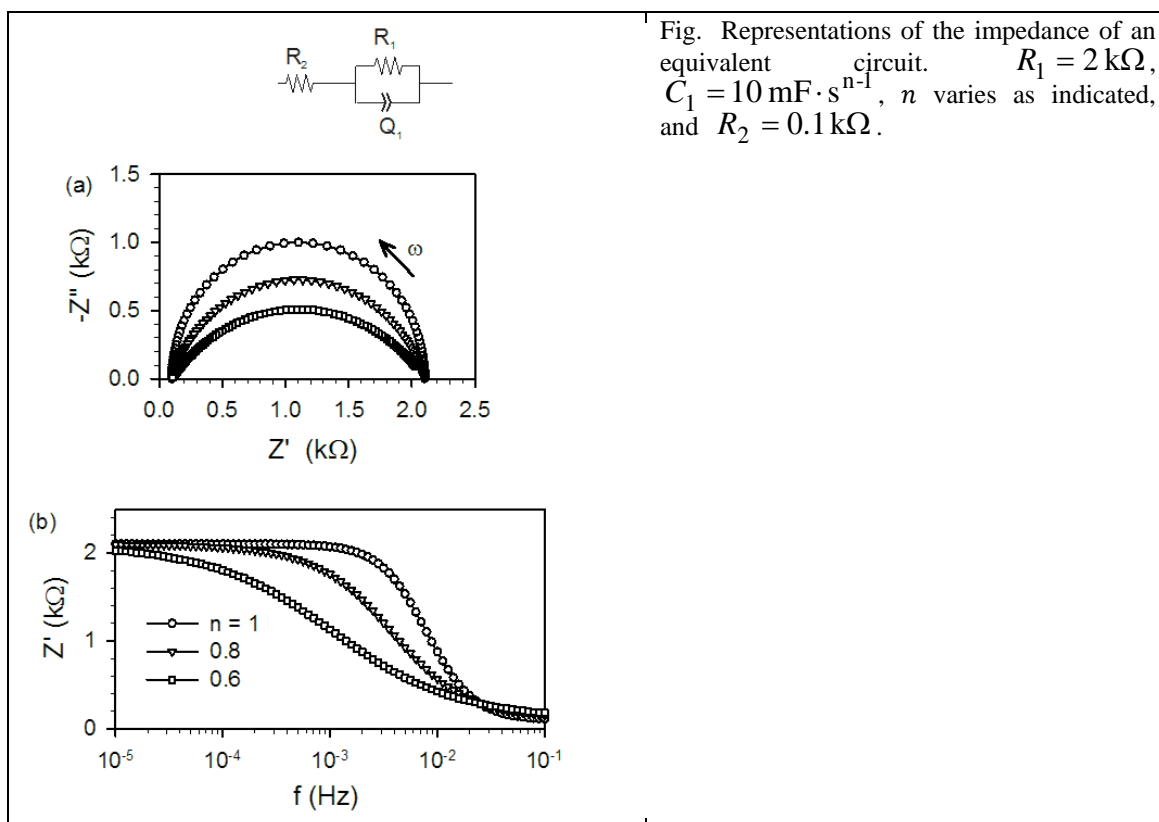
$$C_N = \frac{L_3}{R_3^2} - C_1 \quad (45)$$

The different spectra both with positive and negative low frequency capacitance are shown in Fig. 9(a). If $R_3 < (L_3 / C_1)^{1/2}$ the impedance traces a low frequency arc in the fourth quadrant, otherwise, the impedance remains in the first quadrant. The intercept of Z with the real axis (i.e. the transition of $C'(\omega)$ to negative values) is at the frequency

$$\omega_{NC} = \left[\frac{1}{L} \left(\frac{1}{C_1} - \frac{R_3^2}{L_3} \right) \right]^{1/2} \quad (46)$$

In the capacitance vs. frequency representation, Fig. 9(b), the presence of the inductor appears as the negative contribution that becomes more negative towards lower frequencies. At high frequencies the plot is dominated by C_1 , and at lower frequencies the circuit capacitance begins to decrease due to the inductive effect. It shows a dip at the transition from positive to negative values, at ω_{NC} , and then the absolute value

increases towards lower frequencies, until it saturates at the value $-C_N$.



As a final example of the simple equivalent circuits we consider the presence of a Constant Phase Element (CPE) as shown in Fig. The normal application of a CPE is to describe a capacitive process that presents some frequency dispersion, which occurs when the CPE index n departs from 1. In fact the pure capacitance response with $n = 1$ is very rare, and it is often necessary to use CPEs with $n < 1$ in fitting of data.⁴⁶ Despite such a widespread occurrence, a general origin for CPE response in terms of a unique physical process has not been identified. CPE is related to systems that show some kind of self-scaling, either of geometric origin (such as fractal electrodes⁷⁷) or dynamical origin (like in some multiple trapping systems⁷⁵). Due to self-scaling properties of CPE response, it is normally difficult to identify the specific factor causing the dispersion, and CPE should be regarded as a useful and often indispensable tool for data description.

When index n becomes small the modification of the capacitive response is rather large, and the RQ arc becomes progressively depressed, as shown in Fig. 10(a). The CPE also produces a strong slowing down of the response. Fig. 10(b) shows that for the

capacitor response the transition from low to high frequency resistance is completed in less than two decades of frequency, while for $n = 0.6$ it requires more than four decades. Consequently, the characteristic frequency shows an important decrease as n decreases, according to the expression⁴⁶

$$\omega_1 = \frac{1}{(R_1 Q_1)^{1/n}} \quad (47)$$

The foregoing discussion has shown that equivalent circuit representations are a very powerful resource for the inverse problem that is usually a main task in IS data treatment: to establish an impedance model from a set of data. Importantly, equivalent circuits allow to visualize the structure of the model and to separately treat data portions in certain relevant frequency windows. However, equivalent circuits are by no means *necessary* to establish a physical model; what is needed is an impedance *function*, in any of its all possible analytical representations.

It should also be mentioned, that not all complex functions of frequency are valid impedance responses. The complex function $Z(\omega)$ must obey causality conditions (i.e., the stimulus must precede the response), which imposes analytical constraints known as Kramers-Kronig transforms.⁷² These transforms allow to construct the real part of $Z(\omega)$ if the imaginary part is known at all the frequencies, and vice versa. Using equivalent circuit elements such as those of Table 1, ensures that the resulting model obeys the Kramers-Kronig relations.

4. Basic physical model and parameters of IS in solar cells

4.1. Simplest impedance model of a solar cell

In the process of obtaining physical information from IS data, it is necessary to relate the observable equivalent circuit elements with the system properties. As mentioned before, equivalent circuits are a useful tool for interpretation, and the meaning attached to the circuit elements, the potential in the circuit, etc., may be quite different from the standard physics textbook examples.

This is particularly the case in the analysis of solar cells. Note that the ac equivalent circuits that we have discussed are composed of passive elements (resistances, capacitances). It is usual to interpret the flow of charges in circuits in terms of the mechanistic view of drift of charges in electrical field caused by potential differences. This image is also very popular for explaining the photovoltaic action, e.g. in a p - n

junction, in terms of an electric field that sends oppositely charged carriers in different directions. However, a solar cell is a kind of *battery*, which is an element that produces an electromotive force, and such element *cannot* work with electrostatic voltage differences alone. According to Volta's idea the electromotive force is an *nonelectrostatic action* on charges in conductors that causes unlike charges to separate and remain separated.⁷⁸ Thus we wish to obtain the *internal* ac equivalent circuit of a solar cell, using only linear elements associated to small signal ac perturbation, with emphasis on the interpretation of the elements that make it work as a device for production of electricity. The key approach for useful reading of ac equivalent circuits of DSC is that potentials in the circuit represent electrochemical potential of electrons (or holes) in the actual device.

To clarify this, we start with the simplest model of a solar cell, discussed above in Sec. 2.2, that contains the necessary elements without complications of carrier transport, specific features of selective contacts, etc. We calculate the IS response of the solar cell of Fig. 4,³⁵ corresponding to the application of a small ac electrical perturbation.

We showed before that the dynamic response of the simple solar cell model in Fig. 4 is determined by the equation

$$\frac{\partial n}{\partial t} = G - U_n - \frac{j}{qL} \quad (48)$$

where $G = G_\Phi + G_d$ is the carrier generation rate. For calculating the IS response we need to combine two approaches: (1) All physical quantities are composed of a stationary part (e.g., \bar{n}) and a small perturbation part that varies with time. (2) We must reduce all the dependencies implicit in Eq. (48), explicitly to voltage, so that the result is an impedance.

For example the carrier density dependence on time takes the form

$$n(t) = \bar{n} + \hat{n}(t) \quad (49)$$

The variation of voltage applied in the solar cell produces a variation of the electron Fermi level, which changes as

$$E_{Fn}(t) = \bar{E}_{Fn} + q\hat{\phi}_n(t) \quad (50)$$

where $\hat{\phi}_n$ is the small perturbation voltage. But by Eq. (15) there is a unique dependence of n on E_{Fn} . Thus

$$n(t) = n(E_{Fn} + \hat{\phi}_n) \quad (51)$$

Expanding to first order Eq. (51) we obtain

$$n(t) = \bar{n} + \frac{\partial n_c}{\partial E_{Fn}} \hat{\phi}_n \quad (52)$$

The derivative in Eq. (52) appears recurrently in solar cell theory and requires a special denomination. We introduce the *chemical capacitance*, a thermodynamic quantity that reflects the capability of a system to accept or release additional carriers with density N_i due to a change in their chemical potential, μ_i .^{35,79} In general, for a volume element that stores chemical energy due to a thermodynamic displacement, the chemical capacitance *per unit volume* is defined as

$$c_\mu = q^2 \frac{\partial N_i}{\partial \mu_i} \quad (53)$$

More generally, we use in Eq. (53) the electrochemical potential, that coincides with the electron Fermi level.⁶⁰ Thus the chemical capacitance for conduction band electrons is³⁵

$$c_\mu^{cb} = q^2 \frac{\partial n}{\partial E_{Fn}} = \frac{q^2 n}{k_B T} = \frac{N_c q^2}{k_B T} \exp[-(E_C - E_{Fn})/k_B T] \quad (54)$$

The macroscopic capacitance for a film of thickness L , area A and porosity p is

$$C_\mu^{cb} = LA(1-p)c_\mu^{cb} \quad (55)$$

being the amount $LA(1-p)$, the volume of the film, V_f . Using Eqs. (49), (52) and (54), we arrive at the relationship between the small perturbation of carrier density and voltage:

$$\hat{n} = \frac{1}{q} c_\mu^{cb} \hat{\phi}_n \quad (56)$$

Next we expand the recombination term in Eq. (48) and we obtain

$$U_n(t) = \bar{U}_n + \left(\frac{\partial \bar{U}_n}{\partial n} \right) \hat{n} = \bar{U}_n + \left(\frac{\partial \bar{U}_n}{\partial n} \right) \frac{c_\mu^{cb}}{q} \hat{\phi}_n \quad (57)$$

And finally, the current is

$$j(t) = \bar{j} + \hat{j}(t) \quad (58)$$

When we insert the different expanded expressions into Eq. (48), we obtain, first, a time-independent equation that was already discussed, (12), and which gives the stationary condition of the solar cell according to bias voltage and illumination. In

addition, the time dependent terms provide a new equation that takes the form:

$$c_{\mu}^{cb} \frac{\partial \hat{\phi}_n}{\partial t} + \frac{\hat{\phi}_n}{r_r^{cb}} + \frac{\hat{j}}{L} = 0 \quad (59)$$

where the recombination resistance per unit volume is given by

$$r_r^{cb} = \frac{1}{c_{\mu}^{cb}} \left(\frac{\partial \bar{U}_n}{\partial n} \right)^{-1} \quad (60)$$

Note that Eq. (60) corresponds to the following expression

$$r_r^{cb} = \left(q^2 \frac{\partial \bar{U}_n}{\partial E_{Fn}} \right)^{-1} \quad (61)$$

and the macroscopic recombination resistance, that corresponds to the reciprocal derivative of the recombination current with respect to voltage, is

$$R_r^{cb} = \frac{1}{LA(1-p)} r_r^{cb} \quad (62)$$

The fundamental parameter describing recombination, however is the recombination per unit of effective internal area (A_{eff}) $r_r' = A_{eff} R_r = LA(1-p)hR_r = hr_r$, being h the ratio between the effective area and the volume of the TiO_2 film, $h = A_{eff} / LA(1-p)$.

We remark that the carrier generation terms are absent from Eq. (59), since in IS we can only modulate electrical injection of carriers; the situation is different in light-modulated techniques, as explained in the Chapter by Peter and Hagfeldt.

From Eq. (59) the structure of the impedance model can be inferred directly.³⁵ $\hat{\phi}_n$ can be viewed as the potential in an equivalent circuit (but remember that physically it is the electrochemical potential!). Then Eq. (59) is Kirchoff's rule for current conservation. The first term is a capacitive current, the second one is an ohmic current through the resistor R_r , and the third is the extraction current. Note that the two first currents do *not* represent transport currents (i.e., an ensemble of carriers moving in a certain direction in space), but the rates of creation and destruction of conduction band electrons. In fact recombination is what maintains the current in a diode, as explained in the book of Sha.⁶⁹

For calculating the impedance we apply the Laplace transform ($\partial/\partial t \rightarrow i\omega$) in Eq. (59) and use the definition in Eq. (22)

$$Z = -\frac{\hat{\phi}_n}{\hat{j}} = \frac{1}{L} \frac{1}{\frac{1}{r_r^{cb}} + i\omega c_\mu^{cb}} \quad (63)$$

Eq. (63) clearly corresponds to the parallel combination of the chemical capacitance and recombination resistance, which is the *minimal IS model* of a solar cell. Fig. 11(b) shows the equivalent circuit corresponding to the basic solar cell scheme of Fig. 11(a).

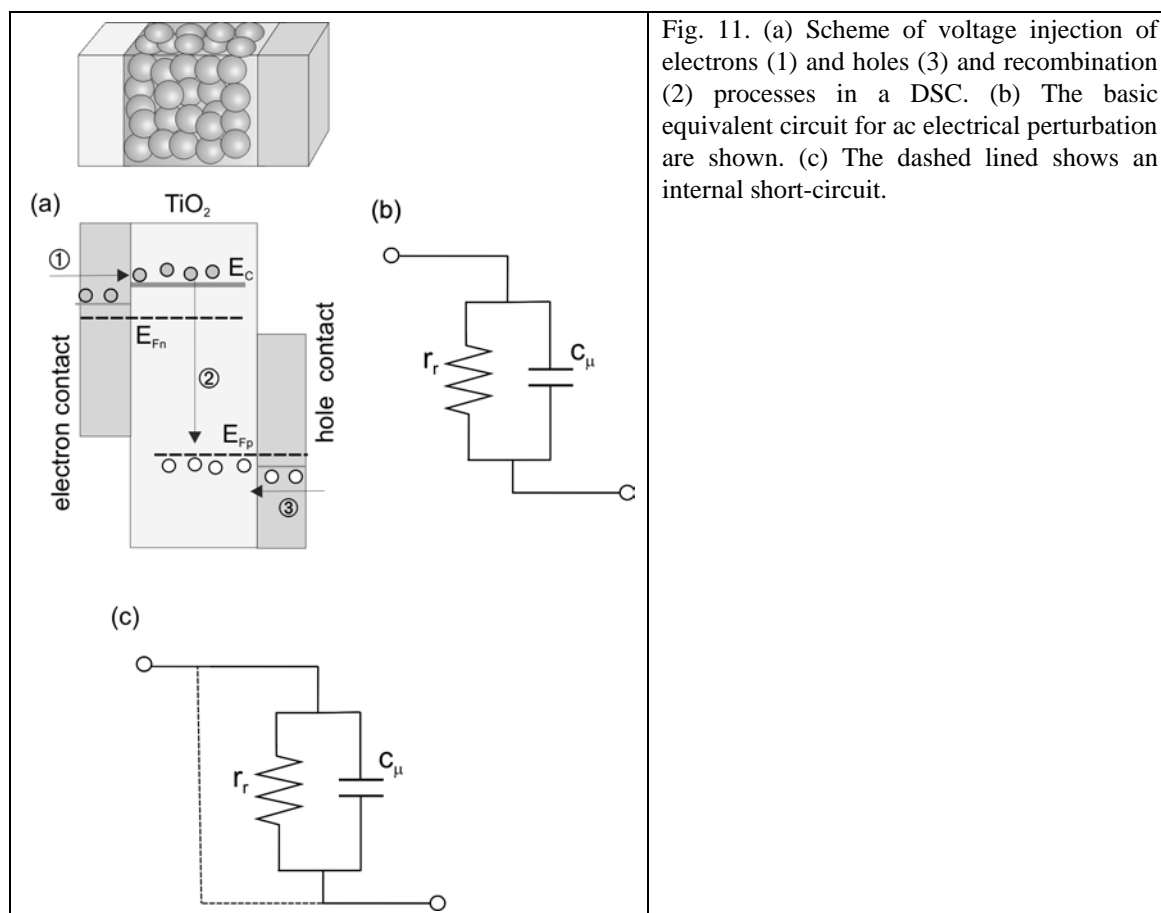


Fig. 11. (a) Scheme of voltage injection of electrons (1) and holes (3) and recombination (2) processes in a DSC. (b) The basic equivalent circuit for ac electrical perturbation are shown. (c) The dashed lined shows an internal short-circuit.

In Fig. 11(b) we can observe that the chemical capacitance is a necessary element of the solar cell: it produces a voltage (associated to splitting of Fermi levels) by the creation of excess carriers from photons. An important message of Fig. 11 is that recombination resistance must be *large*, as this will allow carriers accumulated in the capacitive element to flow through the external circuit when they return to the equilibrium situation. We point out that the recombination resistance in Fig. 11(b) corresponds to the diode in the dc circuit of Fig. 5.

Figure 11(b) displays also the special structure of connection of the R and C elements

by selective contacts that is implicit in the derivation of the result in Eq. (63). This connection is essential to channel the carriers in the desired direction. An example of the failure of selective contacts is shown in Fig. 11(c). Electrons and holes meet directly at the left contact, producing an internal short circuit. Such device cannot produce a photovoltage.

It should be also recognized that in contrast with electrochemical batteries and capacitors, in solar cells there is always an electrical connection between the outer electrodes via the internal resistance r_r . In fact the solar cell works by promotion of carriers from a low to a high energy level, with the energy of the photons,³³ and such energy levels are separately connected to the outer electrodes. Since the excitation is possible, the converse process, which is the decay from high to low energy level by radiative recombination, must be possible as well. This is the most favorable case of the recombination resistance, which is unavoidable, as it is an intrinsic component of the photophysical process that makes the solar cell produce useful work. In this sense we regard Fig. 11(b) as the minimal model.

But while certain recombination processes are unavoidable in the solar cell, additional sources of recombination are detrimental to the performance. For example, in Fig. 11(c) a strong recombination at the left contact produces a low internal resistance, in a process that does not contribute at all in carrier generation. This must be regarded as a failure of the device. In fact reducing surface recombination is the most critical step in the preparation of high efficiency industrial silicon solar cells.⁸⁰ In general, equivalent circuits illustrate a main point about solar cell operation: the dc current follows predominantly the path of least resistance. Therefore, low resistances *in parallel* to the chemical capacitance reduce the output power.

The ideal model provides a very useful reference to understand IS results of solar cells. However, it should be emphasized that one of the goals of hybrid nanostructured organic-inorganic solar cells is to obtain low cost photovoltaic devices, and therefore there are additional elements contributing to the photovoltaic conversion process. A key feature that makes IS attractive is that it can be applied in full devices and indicate thereof the main limitations to photoelectrical performance. We will progress in subsequent sections towards a full realistic model for DSC devices, but a simple example may be illustrative.

The usual way to construct a selective contact for holes is using a hole transport

material that readily conducts hole carriers and blocks electrons, and this is shown in Fig. 12. However, it is generally the case that organic conductors, that can penetrate the pores of TiO_2 nanostructures, possess a limited carrier mobility. Being the conductivity low, a gradient of the hole Fermi level is required to inject, as in Fig. 12 (a), or to extract the holes across the layer. Comparing this case with the ideal selective contact in Fig. 11(a), the difference is that in the latter case the extraction of holes has no cost at all in terms of Fermi level gradient. We have mentioned above that *parallel* resistances should be large, and from the present example we appreciate that *series* resistance must be relatively small to avoid power losses.

The Fermi level drop for hole transport in Fig. 12 implies a “potential drop” in the equivalent circuit, with an associated impedance which is related to hole diffusion. Therefore, problems in the performance of contacts, or transport layers, can be detected with IS measurement. To do so, we must be able to separate, in the IS data, following the previous example, the contribution of recombination resistance and transport layer resistance. This will depend largely on the values of *capacitances* of the two elements. Interpreting the capacitance, is a major tool for identifying the physical origin of processes observed in IS measurement, as mentioned before.

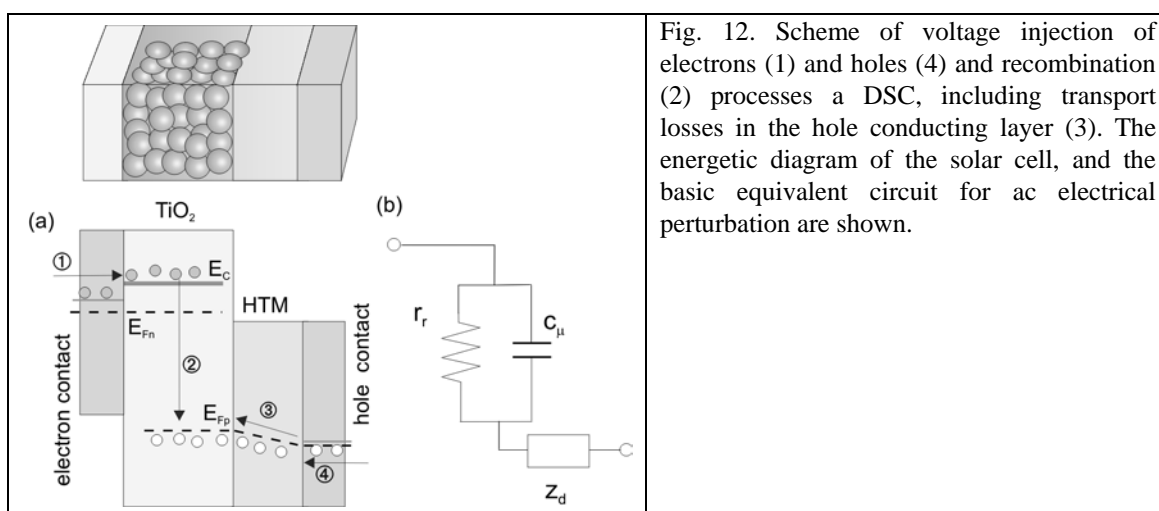


Fig. 12. Scheme of voltage injection of electrons (1) and holes (4) and recombination (2) processes a DSC, including transport losses in the hole conducting layer (3). The energetic diagram of the solar cell, and the basic equivalent circuit for ac electrical perturbation are shown.

4.2. Measurements of electron lifetime

It is interesting to explain in more detail the relationship between the equivalent circuit elements describing the solar cell IS response and the electron lifetime. In order to describe IS behavior we have considered in Eq. (63) an experiment that relates voltage to electrical current measurement. But we can apply the general dynamic

equation (59) in experiments in which we apply a perturbation and let the system decay by itself.^{54,57} Since no current is extracted we obtain

$$\frac{\partial \phi_n}{\partial t} = -\frac{\phi_n}{r_r^{cb} c_\mu^{cb}} = -\frac{\phi_n}{R_r^{cb} C_\mu^{cb}} \quad (64)$$

Eq. (64) describes, for example, the exponential decay of a small step of excess carrier concentration by recombination. From Eq. (64), the time constant of the decay process, which we denote the *response time*, is

$$\tau_r = r_r^{cb} c_\mu^{cb} \quad (65)$$

and this gives also, in the model outlined above

$$\tau_r = \left(\frac{\partial \bar{U}}{\partial n} \right)^{-1} \quad (66)$$

With the normal assumption of first order reaction for direct electron transfer from the conduction band, Eq. (5), we obtain simply $\tau_r = \tau_0$. In this simple model the lifetime is constant, and the response time and electron lifetime have the same meaning. But in general, the lifetime can be dependant of steady-state conditions, as it is obvious in Eq. (66). In addition, in the presence of additional relaxation processes such as trapping and release in localized electronic states, the response time contains components due to kinetic delays in addition to the free carrier lifetime.⁴⁰

5. Basic physical models and parameters of IS in dye-sensitized solar cells

5.1. Electronic processes in a DSC

A general view of the electronic and ionic processes occurring in a DSC are shown in Fig. 13. With respect to the basic solar cell model in Fig. 4, in a DSC the sensitizer (molecular dye, inorganic quantum dot, etc.) is the absorber.³³ The selective contacts to the absorber are formed, first, by an electron transport material (ETM), which is the wide bandgap semiconductor nanostructure on top of a TCO, being TiO₂ the archetypical semiconductor. The second selective contact is a hole transport material (HTM), which in original DSC is a redox carrier in liquid electrolyte, but in full solid devices is an organic hole conductor, as explained in the Chapter by Snaith.

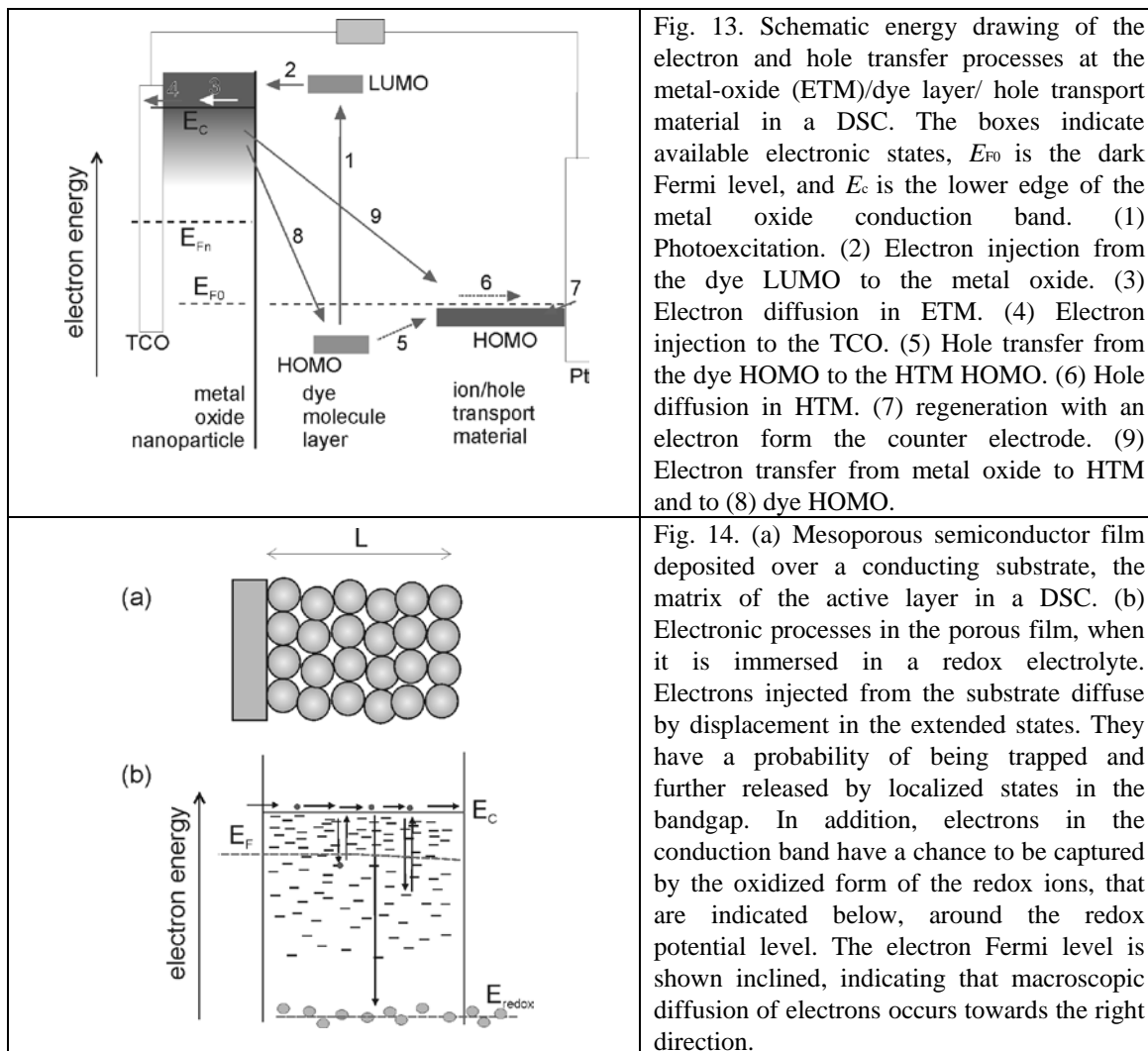
In IS we do not monitor directly the photoinjection process, as explained above, and the main attention is focused on electronic processes of electrons in the ETM (and

eventually holes in solid state HTM), which are described in Fig. 14. The reason why IS relates predominantly to electrons in the wide bandgap semiconductor, is that the concentration of redox carrier in electrolyte is very high (approaching 10^{20} cm^{-3}), and it is hardly affected by the bias, while electron concentration changes by many orders of magnitude when the potential is displaced.⁸¹ We can therefore monitor wide variations of the IS parameters related to electronic processes, as discussed below.

Materials for hybrid solar cells based on low cost semiconductors, usually include a large extent of electronic energy disorder, implying a wide distribution of localized electronic states in the bandgap, as indicated in Fig. 14.⁶¹ The transport of electrons is usually described in terms of classical multiple trapping transport.⁶¹ This model includes two classes of electronic states: the transport states above the mobility edge (that may be associated with extended states in the conduction band), and localized states in the bandgap. The latter states do not participate in spatial displacement but retain the carriers for a certain time by trapping-detrapping process. A process of injection (or extraction) of carriers causes diffusion of electrons along the extended states, and these carriers have the chance to be captured, and later released, by traps.

In addition free carriers have a possibility to be captured in recombination process. Specifically shown in Fig. 14, is the electron transfer from the metal oxide nanoparticles towards ionic species in solution (these are depicted around their own Fermi level, the redox potential). This is the dominant recombination mechanism in standard liquid electrolyte DSC,¹ where the I^-/I_3^- redox couple is normally used to regenerate the oxidized dye molecules from the counterelectrode. In DSC with solid HTM⁸² the interfacial charge transfer implies recombination of electrons and holes in the separate materials.

In the following subsections we discuss the impedance elements associated with the electronic processes shown in Fig. 14.



5.2. The capacitance of electron accumulation in a DSC

We have already described in Eq. (54) the chemical capacitance associated with delocalized, transport states, using the Boltzmann distribution (nondegenerate conditions). The presence of bandgap states introduces additional possibilities for loading the semiconductor with charges. For one specific electronic state characterized by the energy E (this energy is defined to be increasingly negative for states deeper in the gap), the average equilibrium occupancy is determined by the Fermi level as described by the Fermi-Dirac distribution function

$$f(E - E_{Fn}) = \frac{1}{1 + \exp[(E - E_{Fn})/k_B T]} \quad (67)$$

If the distribution of localized states is $g(E)$, the chemical capacitance is obtained

integrating all the contributions through the bandgap

$$c_{\mu}^{traps} = q^2 \int_{-\infty}^{+\infty} g(E) \frac{df}{dE_{Fn}} dE \quad (68)$$

Using $df(E - E_{Fn})/dE_{Fn} = -df(E - E_{Fn})/dE$ and integrating Eq. (68) by parts, we arrive at

$$c_{\mu}^{traps} = q^2 \int_{-\infty}^{+\infty} \frac{dg}{dE} f(E - E_{Fn}) dE \quad (69)$$

A simple solution to Eq. (69) is obtained by the zero-temperature limit of the Fermi function, i.e. a step function at $E = E_{Fn}$ separating occupied from unoccupied states. Then it follows that

$$c_{\mu}^{traps} = q^2 \int_{-\infty}^{E_{Fn}} \frac{dg}{dE} dE = q^2 g(E_{Fn}) \quad (70)$$

In this approximation, Eq. (70), the charging related to the perturbation dV corresponds to filling a slice of traps at the Fermi level, as explained in Fig. 15, and the chemical capacitance is proportional to the density of states (DOS).

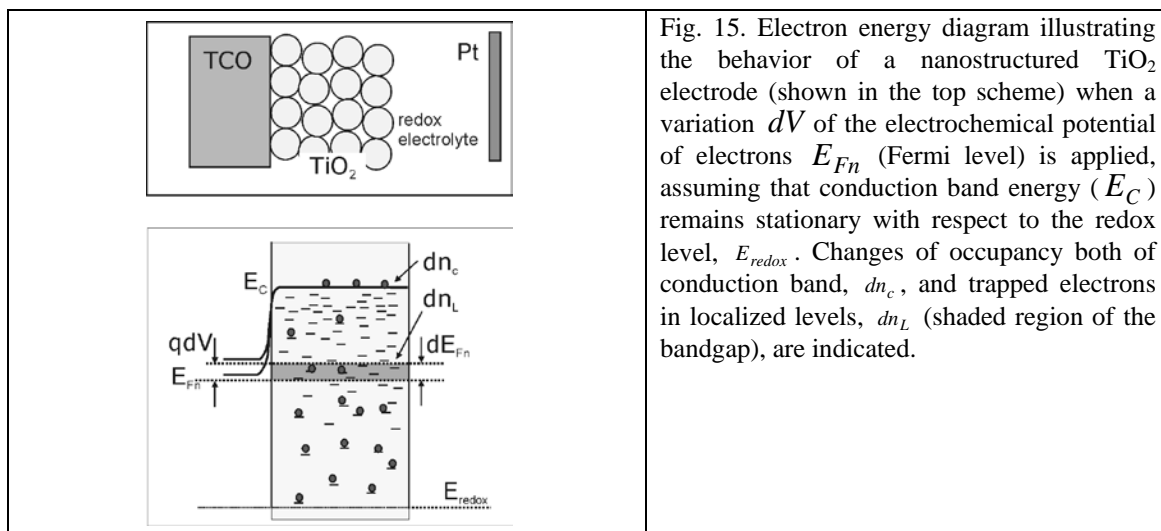


Fig. 15. Electron energy diagram illustrating the behavior of a nanostructured TiO₂ electrode (shown in the top scheme) when a variation dV of the electrochemical potential of electrons E_{Fn} (Fermi level) is applied, assuming that conduction band energy (E_c) remains stationary with respect to the redox level, E_{redox} . Changes of occupancy both of conduction band, dn_c , and trapped electrons in localized levels, dn_L (shaded region of the bandgap), are indicated.

A common finding in nanostructured TiO₂ is an exponential distribution of localized states in the bandgap as described by the expression

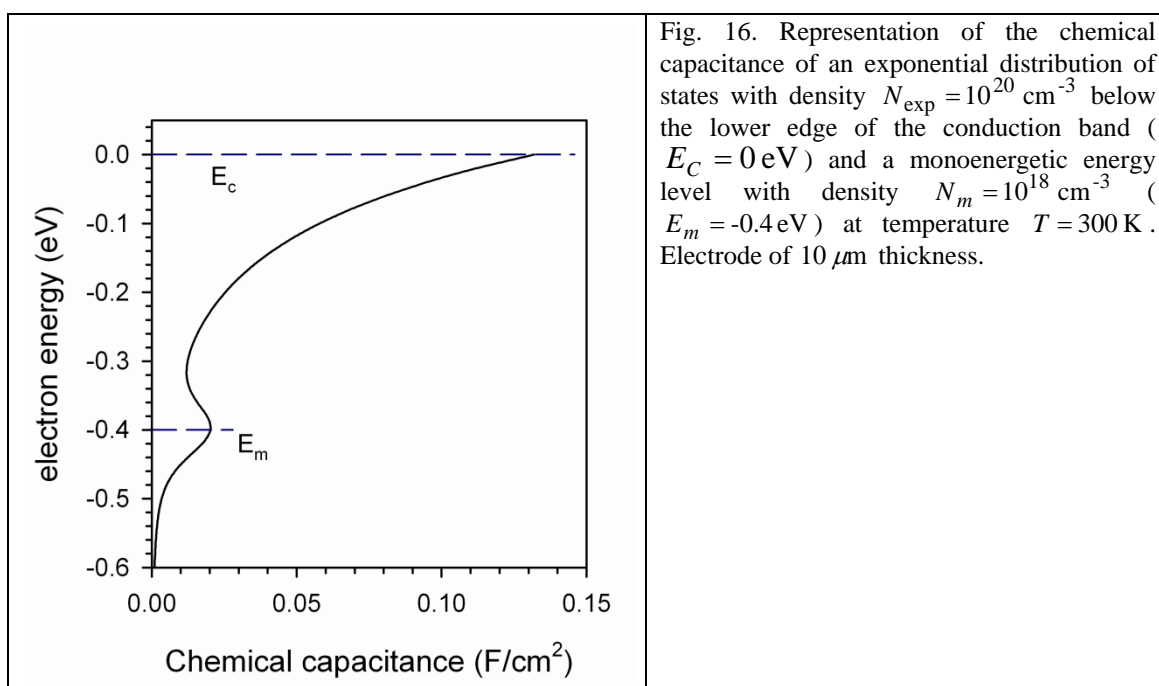
$$g(E) = \frac{N_L}{k_B T_0} \exp[(E - E_c)/k_B T_0] \quad (71)$$

Here N_L is the total density and T_0 is a parameter with temperature units that

determines the depth of the distribution, which can be alternatively expressed as a coefficient $\alpha = T/T_0$. According to Eqs. (70) and (71) the chemical capacitance should display an exponential dependence on applied potential:

$$C_{\mu}^{traps} = \frac{N_L q^2}{k_B T_0} \exp[(E - E_C)/k_B T_0] \quad (72)$$

with a slope $q/k_B T_0$ in log-linear representation with respect to voltage, a fact that has been observed many times in the literature, using IS (as discussed in the next Section) and cyclic voltammetry (CV).^{51,53,83,84} In addition, nanostructured TiO₂ usually shows a nearly-monoenergetic state below the bandgap. Therefore the total chemical capacitance, due to occupation of electronic levels, displays the shape shown in Fig. 16, and this shape is indeed obtained in measurements.⁸⁵ From here onwards we will use C_{μ} as the sum of the contributions from traps and extended states, see below Eq. (113).



One important parameter for nanostructured devices is the position of the semiconductor conduction band/transport level, E_C , with respect to the Fermi level of holes, or redox potential of ion carriers. E_C determines, for example, the maximum photovoltage that can be obtained in a DSC,²⁴ and also the efficient injection of photoexcited electrons from the sensitizer. E_C can be modified by absorption of dipolar species at the metal oxide/electrolyte interface, as indicated in Fig. 17(a).⁸⁶

Measurements of capacitance by IS or CV immediately reveal the global displacement of the semiconductor energy levels as a shift along the potential axis, as illustrated in Fig. 17(b).

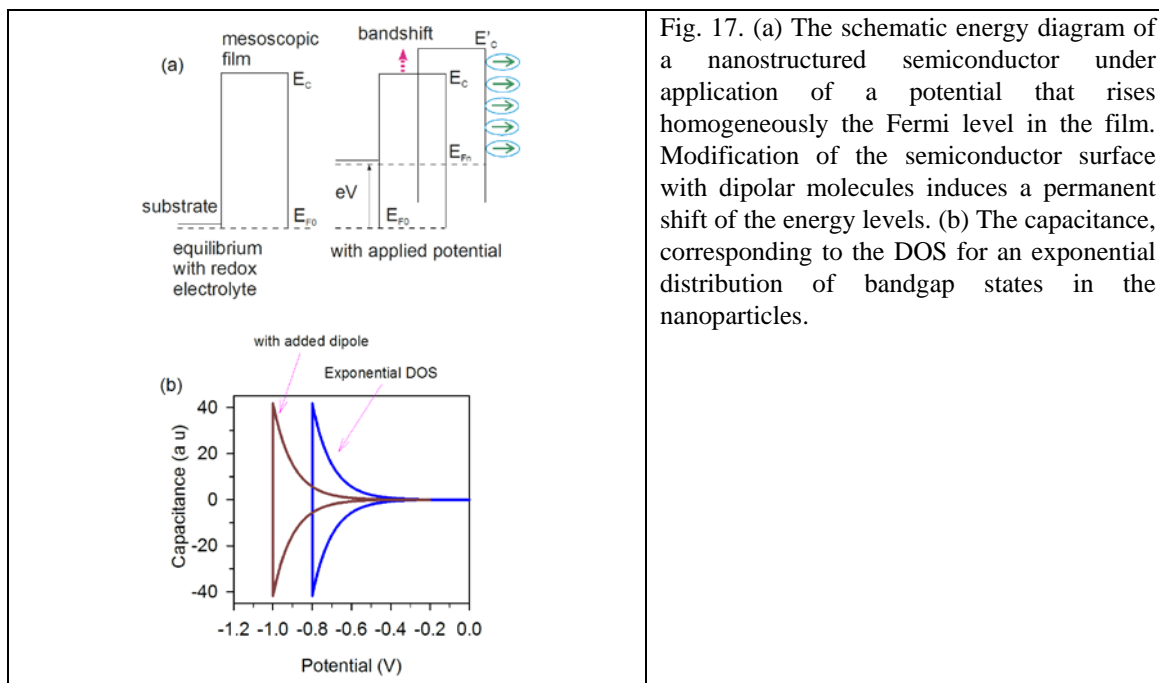


Fig. 17. (a) The schematic energy diagram of a nanostructured semiconductor under application of a potential that rises homogeneously the Fermi level in the film. Modification of the semiconductor surface with dipolar molecules induces a permanent shift of the energy levels. (b) The capacitance, corresponding to the DOS for an exponential distribution of bandgap states in the nanoparticles.

For maintaining charge neutrality into a nanostructured film under electron accumulation, it is required that the increasing electron charge in the nanoparticles be accompanied by positive ion charge at the semiconductor/electrolyte interface. In addition to the chemical capacitance, C_μ , ionic accumulation charges the Helmholtz capacitance, C_H , which is usually a constant, and is connected in series. The total capacitance becomes

$$C = \left(C_\mu^{-1} + C_H^{-1} \right)^{-1} \quad (73)$$

Equation (73) also describes the distribution of the applied bias, either as a Fermi level in the semiconductor, or as interfacial potential drop. As discussed later in more detail, at strong forward bias it is usual to find that the capacitance saturates towards C_H , implying that the increasing potential modifies the voltage in the Helmholtz layer, so that the band shifts.

It should be emphasized that in general C_μ depends on the properties of the electrochemical potential of the carriers. The model explained above in terms of the distribution of electronics states is one possible approach that has been found very

useful in the interpretation of capacitance measurements of DSC.^{53,87} In general, however, ionic effects, interactions, etc., that govern the electrochemical potential,⁸⁸ will affect the chemical capacitance.

5.3. Recombination resistance

In the Applications Section we will show that the DSC operation is very similar to the ideal photovoltaic model that has been outlined above. The main reason for this are:

- (1) The TCO/TiO₂ contact and nanostructured TiO₂ network provide a very good electron selective contact, whereby the Fermi level of the TCO follows the rise of the electron Fermi level in TiO₂ nanoparticles.
- (2) Electron transport is fast enough to provide long diffusion lengths.

Despite these properties, DSC performances remain far below the theoretical efficiencies that can be calculated on the basis of the absorption band of current sensitizers such as N719.⁸⁹ One important limitation to present DSC efficiency is that the Fermi level (redox potential) of the dominant redox couple, I/I₃⁻, is too high and limits the photovoltage. Other redox couples, with a more positive redox potential (in electrochemical scale) show poorer kinetic properties at the different internal interfaces,⁹⁰ which yields higher recombination losses.⁶⁸

Governing recombination at the semiconductor/electrolyte interface is perhaps the most critical issue to improve the DSC performance. There are two basic approaches to analyze recombination in a DSC, either to study the recombination resistance in IS, or the electron lifetime. In the literature the second method is preferred since it can be directly measured by several techniques. From the point of view of IS, both quantities are related by the chemical capacitance as indicated in Eq. (65), and more generally, by the capacitance, which may or not be chemical in origin.⁹¹ However, the lifetime is a quantity that corresponds to the transient behavior of the solar cell, while the recombination resistance contains primary information about recombination rate at steady state,⁴⁰ and we consider that this resistance, appearing in the fundamental circuit of Fig. 11, is the central quantity to discuss recombination in relation to the steady state performance of DSCs. Even if we choose to study electron lifetimes, the main information on charge transfer in the lifetime is the resistance, not the capacitance in Eq. (65).

Let us specify the meaning of recombination flux. In Fig. 4 we showed that solar cell

operation under illumination consists basically in the competition between two currents, the photocurrent due to extraction of the photogenerated carriers, and the recombination current which goes in the opposite sense to generation. In Eq. (12) the recombination current is therefore $j_{rec} = qLU_n$. However in practice, the situation is much more complicated, both in terms of morphology and kinetics, and we need to identify the main components of recombination by measurement. We have already discussed that it is quite difficult to separate the components of measured dc current and this is why we adopt the analysis of IS.

As discussed in Eq. (61), we can calculate the macroscopic recombination resistance as the derivative

$$R_r = \left(A \frac{\partial j_{rec}}{\partial V} \right)^{-1} = \left(Aq \frac{\partial j_{rec}}{\partial E_{Fn}} \right)^{-1} \quad (74)$$

In Fig. 13 we have indicated that recombination process in a DSC is the interfacial charge transfer of electrons in the ETM, to oxidized ions in the electrolyte or holes in the HTM. In order to perform model calculations, precise assumptions on the recombination current dependence both on the electron density and the concentration of electron acceptors in solution, or in HTM, c , are required. A simple way to formulate the recombination rate is a first order reaction, as in Eq. (5)

$$U_{rec} = k_{rec}cn \quad (75)$$

then the recombination current density is

$$j_{rec} = qLU_{rec} = qLk_{rec}cn \quad (76)$$

and we obtain from Eq. (74)

$$\left(R_r \right)^{-1} = \frac{ALq^2k_{rec}c}{k_B T} n \quad (77)$$

If we assume that electron recombination occurs from the conduction band energy level, this last equation can also be expressed as

$$R_r^{cb} = R_{r,0} \exp \left[- \frac{qV}{k_B T} \right] \quad (78)$$

Eq. (78) shows that the recombination resistance decreases as the applied forward bias increases, due to the increasing electron density that augments the recombination rate.

In the experimental results of measurements in DSC it is common to find an expression like in Eq. (78), but with a different exponent, that can be parameterized with a constant β

$$R_r = R_0' \exp\left[-\frac{q\beta V}{k_B T}\right] \quad (79)$$

We should remark that Eq. (79) is an empirical approximation that works well in restricted domains of bias voltage. The observed dependence of recombination resistance on bias may contain additional features, such as a valley, i.e. a minimum of resistance, at low potential,⁹² see below Fig. 36.

The parameter β in Eq. (79) obtains different denominations: it can be related to classical electrochemical behavior known as Tafel law, and it can also be associated with the nonideality factor of classic solar cell theory, i.e., $\beta = 1/m$ in Eq. (1). But it should be recognized that the Tafel law in electrochemistry usually corresponds to the voltage dependence of charge transfer rate at the metal/solution interface. In contrast, in Eq. (79) V is *not* an overpotential, but the Fermi level of electrons, thus the primary cause for the recombination resistance dependence on bias voltage in a DSC, is the increase of the electron density in the inorganic semiconductor, as it was already remarked before. These two causes for the exponential law are widely recognized in photoelectrochemistry of semiconductor electrodes.⁹³ Eq. (78) expresses such model in the case of ideal statistics for electrons. Eq. (79) corresponds to the fact that recombination current is not simply proportional to the total electron density. As mentioned, such deviations are common in many classes of solar cells, even in highly efficient silicon solar cells,⁹⁴ where the diode ideality factor often departs from 1.⁹⁵

Recombination in DSC, depends on a multitude of factors, and they are not easy to separate in experiments using working DSC devices. While no well established consensus has been achieved about fundamental quantitative description of recombination, we can provide a basic classification of the main elements determining recombination in the following way. Recombination is an interfacial charge transfer event at the surface between the semiconductor and the ionic/hole carrier. (Additionally, recombination from the substrate becomes important in some circumstances,⁹⁶ and this is also treated in the Applications Section). Since a distance for electron tunneling should be of the order of 1 nm, we can naturally separate the recombination flux in three elements:

- (1) Electrons reaching recombination sites in the semiconductor surface,
- (2) ions or holes reaching the surface from the electrolyte or hole conductor side, and
- (3) the interfacial events.

The electronic density in semiconductor nanoparticles in a DSC can be readily varied by potentiostatic control, and is accessible by several means, for example we can obtain separate information about this by determination of the chemical capacitance and transport resistance, that we may use as an input in the analysis of the recombination resistance. However, due to spatial and energetic disorder in the semiconductor, there are several electronic paths for charge transfer at the surface, which complicates the analysis, as further discussed below.

In contrast, as mentioned before, for redox ionic species in the electrolyte, the concentration is very high and cannot be varied in situ, maintaining the integrity of the solar cell. For the majority of studies the standard iodine/iodide was used as redox carrier. The overall recombination reaction is given by



The reaction (80) must consist on a multiple-step mechanism, very probably involving the species I_2 ,⁹⁷ and one of the steps will be rate determining. The oxidized species in the electrolyte may therefore be I_2 , and/or I_3^- . Also very important for DSC operation, is the regeneration of the oxidized dye, and this may involve a transient (dye⁺-iodide) intermediate complex,⁹⁸ though this process is difficult to access by IS.

The formulation of models of charge transfer requires to specify the probability of electron transfer from an electronic state at the energy level E to an acceptor species in the electrolyte with concentration c . This is usually given^{99,100} by the expression of the Marcus model

$$v_{el}(E) = k_0 \frac{2ck_B T}{\sqrt{4\pi\lambda k_B T}} \exp\left[-\frac{(E - E_{redox} - \lambda)^2}{4\lambda k_B T}\right] \quad (81)$$

where k_0 is a time constant for tunnelling, which is dependent on the distance of the acceptor to the surface,¹⁰¹ and λ is the reorganization energy.

It is well established that recombination rates are mainly affected by two factors: (1) the position of the semiconductor energy levels, with respect to the redox levels, and (2) treatments of the surface that intercept charge transfer from the semiconductor without decreasing the rate of photoinjection from excited dye molecules.⁸⁴ Recombination with

oxidized dye molecules is thought to be of minor relevance. However, as already mentioned, while a quantitative control of electron density is possible, the measured lifetime or recombination resistance still contains a combination of mechanisms that have not been ascertained in detail.

Leaving aside the complexity of individual charge transfer events, we discuss the density dependence of the recombination resistance analyzing the different electronic paths that may occur in the semiconductor surface in a DSC. Fig. 18(a) provides a possible outline of electronic states that participate in electron transfer at the surface.^{54,102,103} Consistent with the density of states that is measured by capacitance techniques, as indicated in Fig. 16, we assume that the surface may contain transfer states that we classify in three kinds: the transport (conduction band) states, an exponential distribution of surface states, and a monoenergetic deep surface state.

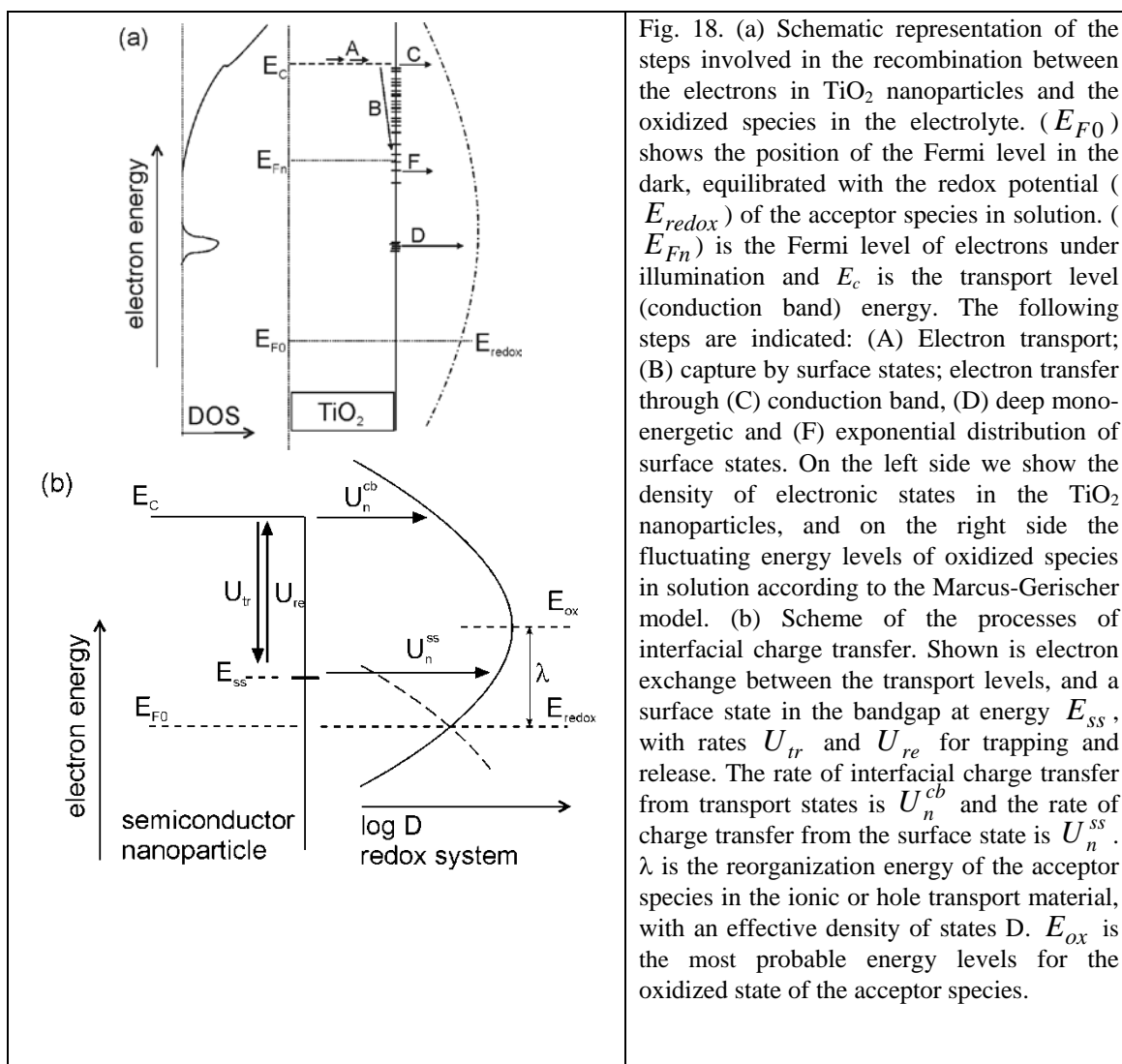


Fig. 18. (a) Schematic representation of the steps involved in the recombination between the electrons in TiO_2 nanoparticles and the oxidized species in the electrolyte. (E_{F0}) shows the position of the Fermi level in the dark, equilibrated with the redox potential (E_{redox}) of the acceptor species in solution. (E_{Fn}) is the Fermi level of electrons under illumination and E_c is the transport level (conduction band) energy. The following steps are indicated: (A) Electron transport; (B) capture by surface states; electron transfer through (C) conduction band, (D) deep monoenergetic and (F) exponential distribution of surface states. On the left side we show the density of electronic states in the TiO_2 nanoparticles, and on the right side the fluctuating energy levels of oxidized species in solution according to the Marcus-Gerischer model. (b) Scheme of the processes of interfacial charge transfer. Shown is electron exchange between the transport levels, and a surface state in the bandgap at energy E_{ss} , with rates U_{tr} and U_{re} for trapping and release. The rate of interfacial charge transfer from transport states is U_n^{cb} and the rate of charge transfer from the surface state is U_n^{ss} . λ is the reorganization energy of the acceptor species in the ionic or hole transport material, with an effective density of states D . E_{ox} is the most probable energy levels for the oxidized state of the acceptor species.

In Fig. 18(a) we appreciate that only transport states establish the electronic communication of the surface with the substrate. So in this model, there is a single channel for transport. But when the electrons arrive in the surface, the recombination current branches into several parallel channels. Fig. 18(b) shows more clearly the situation, by indicating in more detail the trapping and release events on a single surface state, that thereafter acts as recombination center.^{28,92}

It is clear now that in the situation of Fig. 18(b), the recombination current is no longer linearly dependant on the concentration of electrons in the transport state, n_{cb} , but it depends also on the density at the surface state, n_{ss} . In steady state n_{ss} depends uniquely on n_{cb} , but the dependence may be quite involved.^{102,103} In any case in the presence of two channels for charge transfer, the recombination rate is

$$U_n = U_n^{cb} + U_n^{ss} \quad (82)$$

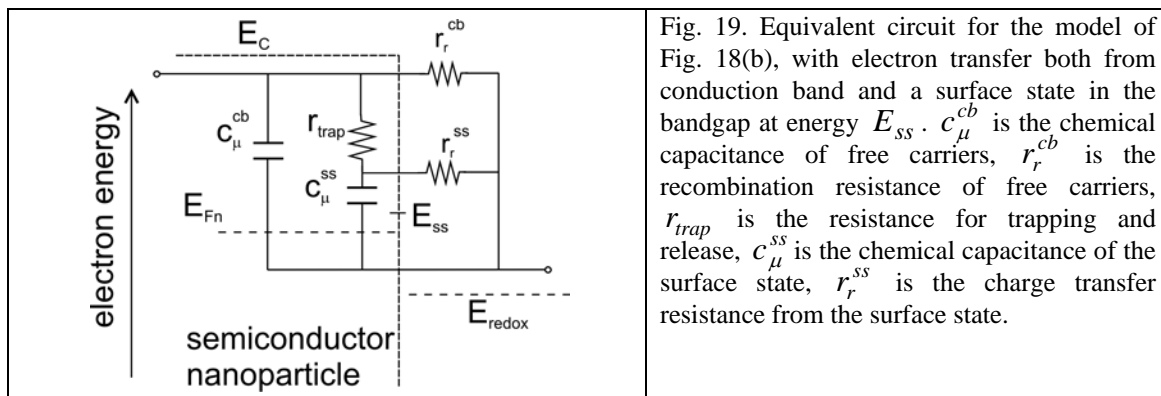
From the general form of the recombination resistance (per unit volume) in Eq. (61), we may write the reciprocal resistance as

$$\begin{aligned} r_r^{-1} &= q^2 \left(\frac{\partial \bar{U}_n^{cb}}{\partial E_{Fn}} + \frac{\partial \bar{U}_n^{ss}}{\partial E_{Fn}} \right) \\ &= \frac{q^2}{k_B T} \left(\frac{n_{cb}}{\tau_{cb}} + \frac{\partial \bar{U}_n^{ss}}{\partial E_{Fn}} \right) \end{aligned} \quad (83)$$

Here, τ_{cb} is the lifetime of conduction band electrons. The first term in parentheses in Eq. (83) recovers Eq. (78), while the second term introduces a different dependence.

Eq. (83) nicely shows that the different recombination branches immediately translate into *parallel* branches in the equivalent circuit for recombination. In order to obtain a detailed understanding of recombination mechanisms in DSCs, it is of critical importance to *separately* measure the different recombination paths. Is this possible using IS?

The answer to this question depends on the dynamic response of the different recombination channels. That is, do the different channel have associated different capacitances? This would provide spectral features for discriminating the channels in the IS data.



Surface states do have, in general, a separate capacitive component. This is related to the chemical capacitance of each state, that is observable depending on rates of trapping and release that are shown in Fig. 18(b), and determine the trap resistance.⁷⁵ Indeed, in the literature of photoelectrochemistry there are detailed treatment of the dynamic effects of surface states,^{13,14,104,105} and the equivalent circuit resulting from this approach is shown in Fig 19. Note in particular the resistances of the two recombination branches r_r^{cb} , r_r^{ss} , that corresponds to the two terms in Eq. (83). However, so far the dynamic effect of surface states in TiO₂ based DSC has not been clearly identified in experiments of IS. Therefore we need to work under the assumption of a quasistatic approximation.^{40,75} we assume that the trapping and release rates, U_{tr} and U_{re} , in Fig. 18(b) are so fast, that the density of the surface state, n_{ss} , remains at quasiequilibrium level in the measurement. But then we measure a unique recombination resistance that will contain the contribution from all the transfer channels present, i.e., r_r . The significance of the different channels has to be inferred from the steady state variation of the recombination resistance.⁹²

As suggested in Fig. 18(a), we should consider the charge transfer from a distribution of surface states $g_{ss}(E)$ in the semiconductor.^{102,103,106} The current per unit macroscopic area of an electrode of thickness L is

$$j_{rec} = qL \int_{E_{redox}}^{E_c} g_{ss}(E) f(E) v_{el}(E) dE \quad (84)$$

Here, $f(E)$ is the occupation of the surface state. In general we denote E_{Fn} the Fermi level of electrons in transport states. For electrons in surface states, the equilibrium statistics is more complex, and in general it is not possible to define a Fermi level.⁹² As mentioned above, if the trapping-release rate is sufficiently fast, we can assume that the surface state is in equilibrium with the transport states, and the

occupancy of both is described by Fermi-Dirac distribution, Eq. (67), with a common Fermi level.

The recombination resistance is

$$R_r^{ss}(E_{Fn})^{-1} = A \frac{dj_{rec}(E_{Fn})}{dV} = q^2 LA \int g_{ss}(E) v_{el}(E) \frac{df(E - E_{Fn})}{dE_{Fn}} dE \quad (85)$$

Applying the zero temperature limit of the Fermi-Dirac distribution, as before in Eq. (68), the following result is obtained

$$R_r^{ss}(E_{Fn})^{-1} = q^2 LA g_{ss}(E_{Fn}) v_{el}(E_{Fn}) \quad (86)$$

Eq. (86) states that the reciprocal charge-transfer resistance is proportional to the product of the density of surface states at the Fermi level, and the probability of electron transfer from such states. This result occurs because the resistance, as discussed before, is a differential quantity corresponding to the current gained by a small step of voltage. In Fig. 18(a), a small displacement of the Fermi level fills the surface states precisely at the Fermi level, hence the resistance detects only those states, as indicated in Eq. (86).

Assuming that $g_{ss}(E)$ has the exponential shape of Eq. (71) with parameters N_s and T_0 , the resistance in Eq. (86) takes the form⁶⁵

$$R_r^{ss}(E_{Fn}) = R_0 \exp \left[\frac{(E_{Fn} - E_{redox} - \lambda)^2}{4\lambda k_B T} - \frac{E_{Fn} - E_C}{k_B T_0} \right] \quad (87)$$

where

$$R_0 = \frac{T_0 \sqrt{\pi \lambda k_B T}}{e^2 LA k_0 c_{ox} N_s T} \quad (88)$$

Eq. (87) can also be expressed as

$$R_r^{ss}(E_{Fn}) = R_0 \exp \left[\frac{(E_{Fn} - E_{redox} - E_\mu)^2}{4\lambda k_B T} + \frac{E_C - E_{redox} - \lambda(1 + \alpha)}{k_B T_0} \right] \quad (89)$$

where

$$E_\mu = \lambda(1 + 2\alpha) = \lambda + \frac{2\lambda}{T_0} T \quad (90)$$

Fig. 20(b) shows the characteristic probability of electron transfer according to Marcus-Gerisher model. The probability increases with the driving force for the transition which is $E_{ss} - E_{redox}$ and is maximum at $E_{ox} = E_{Fn} - E_{redox} = \lambda$, where activationless charge transfer occurs. According to Eq. (89) the resistance dependence

on voltage $V = q(E_{Fn} - E_{redox})$, consists on a Gaussian function, centered at the energy E_μ indicated in Eq. (90). The center E_μ of the Gaussian, is shifted positive in the scale of the Fermi level, with respect to E_{ox} , by an amount $2\lambda\alpha$, in other words $E_\mu = E_{ox} + 2\lambda\alpha$. The behavior of $R_r(E_{Fn})$ in this model is illustrated in Fig. 20(a).

When the Fermi level is below the minimum E_μ , we obtain a useful approximation of Eq. (89)

$$R_r^{ss}(E_{Fn}) = R'_0 \exp\left[-\beta_1 \frac{(E_{Fn} - E_{redox})}{k_B T}\right] \quad (91)$$

where

$$\beta_1 = \frac{1}{2} + \alpha(T) \quad (92)$$

Therefore, this model satisfactorily explains the Tafel dependence indicated in Eq. (79). In addition β_1 is predicted to increase linearly with the temperature.

The model outlined should be taken as an example that a combination of charge transfer channels (in this case by a wide distribution of energies of the surface states) provides a new dependence of the recombination resistance on Fermi level (or electron density). Experimental application of this model will be discussed later on.

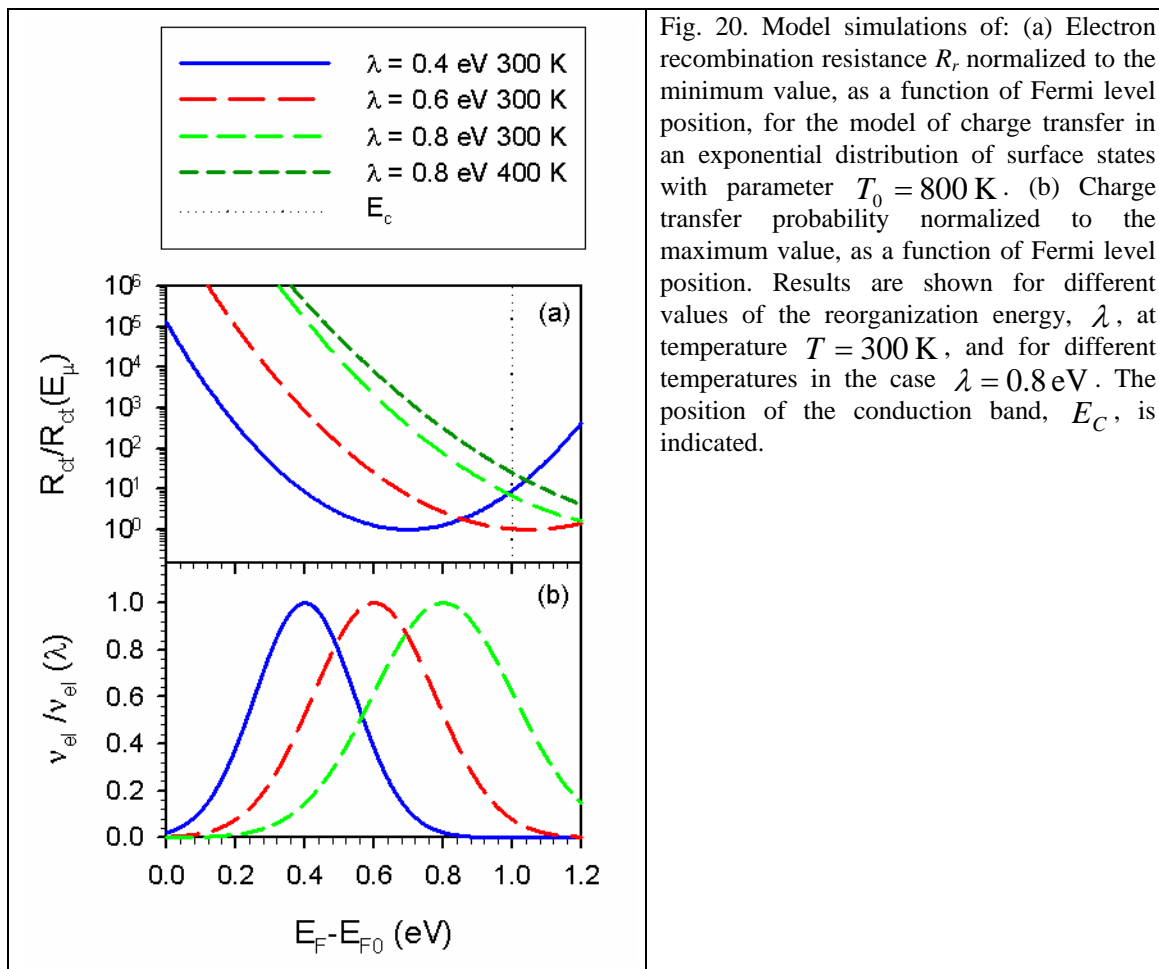


Fig. 20. Model simulations of: (a) Electron recombination resistance R_r , normalized to the minimum value, as a function of Fermi level position, for the model of charge transfer in an exponential distribution of surface states with parameter $T_0 = 800$ K. (b) Charge transfer probability normalized to the maximum value, as a function of Fermi level position. Results are shown for different values of the reorganization energy, λ , at temperature $T = 300$ K, and for different temperatures in the case $\lambda = 0.8$ eV. The position of the conduction band, E_C , is indicated.

5.4. The transport resistance

Obtaining high solar cell efficiency requires to absorb most of the incident photons. Depending on the absorption coefficient of the specific absorber, a certain thickness of the semiconductor is required. Therefore, photogenerated carriers must travel a certain distance to reach the contact, as indicated in Fig. 14(b), and this is often an important aspect of solar cell operation. Electron or hole transport is always driven by a gradient of the Fermi level, as discussed below, and therefore transport in the semiconductor is a loss of free energy of the carriers. In addition, the extraction of carriers to provide a photocurrent in the external circuit is in competition with recombination processes. Therefore it is important to determine the basic transport coefficients of the electronic carriers, such as the mobility, u_n , and the diffusion coefficient, D_n , since this allows us to evaluate the energy losses associated with carrier transport and the diffusion length.

The basic quantity that describes the transport features in IS is a transport resistance, r_t . We will describe the method to obtain D_n from r_t .

Diffusion under concentration gradients is a collective phenomenon, and in DSC and in disordered materials in general, diffusion involves electronic states with widely varying energies.⁶¹ A clear manifestation of this is the fact that in DSC the diffusion coefficient varies several orders of magnitude under modification of bias voltage.⁵⁶ Therefore, it is useful to carefully establish the meaning of measured transport quantities.

To discuss the motion of electrons in a semiconductor material, with concentration $n(x)$ at position x , we assume that the Fermi level, or electrochemical potential, of the electrons has two basic components:^{60,107}

$$E_{Fn} = E_C + \mu_n \quad (93)$$

The first one, E_C , is the energy of the edge of the conduction band (or transport level), which can be associated the Galvani (electrostatic) potential, ϕ , with respect to some suitable reference level, as follows

$$E_C = -q\phi \quad (94)$$

The second component in Eq. (93), μ_n , is the chemical potential of electrons. This is an entropic contribution that accounts for the dispersion of the carriers over all the available sites, and can be normally formulated in terms of the carrier density. If the species is distributed randomly in the available sites the following expression holds, which is equivalent to Eq. (67):

$$\mu_n = k_B T \ln \frac{n}{N_c - n} \quad (95)$$

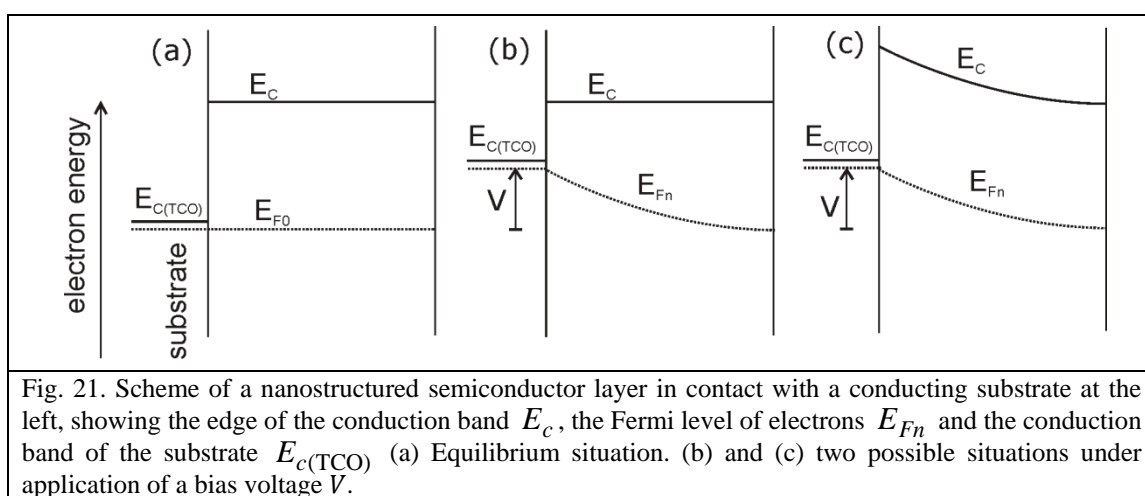
If the sites are far from saturated we obtain the ideal statistics

$$\mu_n = k_B T \ln \frac{n}{N_c} \quad (96)$$

which is equivalent to Eq. (15). Eq. (95) and (96) are very important instances of the chemical potential, but the diffusion theory formulated below is more generally valid for any μ_n .

Now let us consider the system of main interest here, a nanostructured metal-oxide semiconductor, surrounded with electrolyte that contains abundant ionic species of both signs of charge. Fig. 21(a) shows a scheme of such a semiconductor in equilibrium.

When a bias voltage V is applied in the substrate two basic situations may occur, shown in Figs. 21(b) and (c). Note that the voltage V in these figures is *positive* according to the convention of photovoltage used in this chapter, but it is *negative* according to the usual convention of electrochemistry. In Fig. 21(b) the voltage causes a change of concentration of the electrons in the semiconductor, i.e. a change of their chemical potential, and therefore induces a diffusion force. In Fig. 21(c), the bias voltage promotes a bending of the band, and this creates an electric field $F(x) = -\partial\phi/\partial x$ at position x , while the concentration of electrons remains constant everywhere. In this case the electrons move under drift in the electrical field.



What happens actually when we apply a voltage in a certain case, depends mainly on the conditions of *shielding*. In fact by applying a voltage at the contact, there is a difference of electrostatic potential that must be distributed somewhere into the film. The difference between Figs. 21(b) and (c) is that, in (b), the electrical field remains very close to the interface with the substrate, absorbed by a large change of the band offset $E_C - E_{C(TCO)}$. In contrast to this, in (c) $E_C - E_{C(TCO)}$ remains as in equilibrium and the electrical field enters deep into the semiconductor layer.

In DSC we usually employ electrolytes which have large (about 10^{20} cm^{-3}) concentration of ions. When electrons are injected into the nanostructured metal oxide, positive ions move to the surface of the charged nanoparticles and neutralize long range electrical fields. Therefore the change of electrical field occurs right at the substrate interface,¹⁰⁸⁻¹¹⁰ as in Fig. 21(b) and electron transport occurs mainly by concentration gradient, i.e. by diffusion. This is the case also in crystalline p-silicon solar cells, due to

the fact that injected electrons are much less than the majority carrier holes.⁹⁴

Nonetheless, a drift component is possible also in nanostructured semiconductors surrounded by electrolyte. We have indicated in Eq. (73) that the shielding ions may cause a local shift of the conduction band. If the shift is not homogeneous, it induces a macroscopic field in the semiconductor nanoparticulate network.^{29,111} However this effect is minor in liquid electrolyte-based DSC and we may usually neglect it.

In other devices, such as amorphous silicon solar cells,¹¹² and organic light-emitting diodes,¹¹³ the intrinsic carrier density in the semiconductor layer is very low, and is overwhelmed by the number of injected carriers, which determine the electrical field self consistently via Poisson equation. This is called the space-charge limited transport,¹¹⁴ and it is governed by drift transport, and in a certain sense, it is an opposite extreme of transport situation, in comparison with diffusion.

Diffusion. Turning our attention to the dominant conditions in DSC, we analyze diffusive transport of electrons.^{58,60,61} The driving force for diffusion is the gradient of the chemical potential of the electrons. In simple terms there are two forms of the diffusion law:

(1) In the Onsager form, a linear relationship is assumed¹¹⁵ between the diffusive flux and the gradient of the chemical potential

$$J_n = -\frac{nu_n}{q} \frac{\partial \mu_n}{\partial x} \quad (97)$$

The prefactor $L_n = nu_n / q$ is known as the Onsager coefficient.

(2) In the Fick form, diffusion is formulated in terms of the *concentration* gradient

$$J_n = -D_n \frac{\partial n}{\partial x} \quad (98)$$

The coefficient D_n in Eq. (98) is called the *chemical diffusion coefficient*.^{116,117} Comparing Eq. (97) and (98) we obtain the expression

$$D_n = \left(\frac{k_B T}{q} u_n \right) \left(\frac{n}{k_B T} \frac{\partial \mu_n}{\partial n} \right) \quad (99)$$

D_n contains two components: (i) a phenomenological coefficient u_n (the mobility) and (ii) the term $n \partial \mu_n / \partial n$, that accounts for the difference between a gradient in concentration, and a gradient in chemical potential. This last term is expressed in dimensionless form as the *thermodynamic factor* introduced by Darken¹¹⁸

$$\chi_n = \frac{n}{k_B T} \frac{\partial \mu_n}{\partial n} \quad (100)$$

The thermodynamic factor can be expressed with respect to the chemical capacitance as

$$\chi_n = \frac{q^2 n}{k_B T} \frac{1}{C_\mu} \quad (101)$$

Another way to approach the diffusion coefficient is to monitor the random walks of the electronic carriers. The resulting coefficient is termed the jump (or kinetic) diffusion coefficient, which is simply proportional to mobility:

$$D_J = \frac{k_B T}{q} u_n \quad (102)$$

It should be emphasized that D_J is closely related to the tracer diffusion coefficient, D^* . Now we can write the chemical diffusion coefficient as the product

$$D_n = \chi_n D_J \quad (103)$$

Alternatively, we have

$$D_n = \frac{k_B T}{q} \chi_n u_n \quad (104)$$

Eq. (103) is an statement of the generalized Einstein relation.⁶¹

The electron conductivity is

$$\sigma_n = n q u_n \quad (105)$$

Using Eqs. (101), (104) and (105), the conductivity can be expressed in terms of chemical diffusion coefficient and chemical capacitance as

$$\sigma_n = c_\mu D_n \quad (106)$$

Diffusion and drift. As mentioned above, in a system in which the electrochemical potential has the two components indicated in Eq. (93), we may view the electrical current as composed by the sum of conduction and diffusion currents

$$j_n = q n u_n F + q D_n \frac{\partial n}{\partial x} \quad (107)$$

Now Eq. (107) can be written as follows:

$$j_n = -n u_n \frac{\partial E_{Fn}}{\partial x} \quad (108)$$

This relationship states that the electrical current associated with one kind of carrier is proportional to the gradient of the electrochemical potential, E_{Fn} . This approach is usually employed in electronic device modeling.^{25,29}

The transport resistance. Now we can obtain an expression for the transport resistance that we measure in IS. We recall that we are interested in systems, such as a semiconductor layer of thickness L , that may be far from homogeneous in terms of the carrier distribution. Therefore, we want to determine the resistance, associated with a specific kind of carrier (e.g., electrons), in a small spatial distance Δx . Associated with this distance, is a difference of electrochemical potential, that we may express as a difference of *voltage* as $\Delta E_{Fn} = q\Delta\varphi_n$, see Eq. (50). Applying the transport equation, (108), we obtain

$$j_n = -\sigma_n \frac{\Delta\varphi_n}{\Delta x} \quad (109)$$

and therefore

$$R_t = -\frac{\Delta\varphi_n}{Aj_n} = \frac{\Delta x}{A(1-p)\sigma_n} \quad (110)$$

In Eq. (110) we appreciate that the transport resistance depends on the geometric dimensions of the semiconductor slab, and on the reciprocal conductivity.

Transport in a single level. Let us consider a semiconductor with a single transport level, in which the electron carriers are free from interactions. In this case the relation between the electrochemical potential and the carrier density is simply given by Maxwell-Boltzmann statistics, Eq. (17). Since this is the *ideal* statistics, the thermodynamic factor, chemical diffusion coefficient, etc., become considerably simplified.⁶¹ We have $\chi_n = 1$, thus $D_n = D_J = D_0$, we thus obtain Eq. (7) and the standard Einstein relation between diffusivity and mobility:

$$D_n = \frac{k_B T}{q} u_n \quad (111)$$

Multiple trapping transport. In classical multiple trapping transport¹¹⁹⁻¹²¹ we distinguish two classes of electronic states: the transport states above the mobility edge (that may be associated with extended states in the conduction band), and localized

states in the bandgap. Multiple trapping model describes the effect of trap levels over the rate of displacement through transport states. Such effect can be analyzed using the full set of transport-kinetic equations of the model, that provides the system's response in any required set of conditions. However, if trapping and detrapping are fast processes, we apply the quasi-equilibrium approach, that was discussed above in the analysis of surface states. Then electron trapping kinetics can be readily described in terms of electrons densities in transport and trap states, and this second approach will be adopted herein.⁴⁰ A detailed analysis⁷⁵ shows that in fact the first, general, approach reduces to the second one whenever the traps can be considered in quasi-equilibrium conditions.

In the transport states we have a number of carriers n_{cb} , the chemical capacitance c_{μ}^{cb} , and assuming ideal statistics, jump and chemical diffusion coefficients, $D_J^{cb} = D_n^{cb} = D_0$. The localized states (below the mobility edge), have a distribution $g_L(E)$, the number of carriers n_L , and the chemical capacitance c_{μ}^{traps} . Note the relationships for the total carrier density and total chemical capacitance, respectively:

$$n = n_{cb} + n_L \quad (112)$$

$$c_{\mu} = c_{\mu}^{cb} + c_{\mu}^{traps} = c_{\mu}^{cb} \left(1 + \frac{\partial n_L}{\partial n_{cb}} \right) \quad (113)$$

It can be shown⁶¹ that the jump diffusion coefficient is given by

$$D_J = \frac{n_{cb}}{n} D_0 \quad (114)$$

The thermodynamic factor can be written as

$$\chi_n = \left(1 + \frac{\partial n_L}{\partial n_{cb}} \right)^{-1} \quad (115)$$

Hence, the chemical diffusion coefficient has the general form⁵⁸

$$D_n = \left(1 + \frac{\partial n_L}{\partial n_{cb}} \right)^{-1} D_0 \quad (116)$$

Alternatively, we can write Eq. (116) as

$$D_n = \frac{c_{\mu}^{cb}(E_{Fn})}{c_{\mu}^{cb}(E_{Fn}) + c_{\mu}^{traps}(E_{Fn})} D_0 \quad (117)$$

The effect of trapping in the chemical diffusion coefficient is dominant when $\partial n_L / \partial n_{cb} \gg 1$. In this case the result is

$$D_n = \left(\frac{\partial n_{cb}}{\partial n_L} \right) D_0 \quad (118)$$

which can also be expressed

$$D_n = \frac{c_\mu^{cb}(E_{Fn})}{c_\mu^{traps}(E_{Fn})} D_0 \quad (119)$$

Eq. (118) shows that the chemical diffusion coefficient in the presence of traps is reduced by the relationship of free to trapped number of electrons for a small variation of the Fermi level.

We obtain the following result for the conductivity:

$$\sigma_n = D_n c_\mu^{traps} \quad (120)$$

This last equation is a formulation of the generalized Einstein relation that links the conductivity, the chemical diffusion coefficient and the chemical capacitance.^{61,122}

We can also express the conductivity in terms of the carrier density and jump diffusion coefficient

$$\sigma_n = \frac{q^2 n}{k_B T} D_J = \frac{q^2 n_{cb}}{k_B T} D_0 \quad (121)$$

Equation (120) can also be expressed as $\sigma_n = D_0 c_\mu^{cb}$. This shows that in multiple trapping model, the conductivity is determined exclusively by the transport level and is *completely independent* of the presence and distribution of traps. The steady-state conduction is not affected by the trapping process, because the traps remain in equilibrium.

Multiple trapping in exponential distribution. As mentioned before it is well established that nanostructured (anatase) TiO₂ used in DSC shows this type of distribution of states in the bandgap.^{51,53,83,84,123} We discuss the regime of electrochemical potentials in which the Fermi level is well below the conduction band. Hence the free electron density is much lower than trapped electrons number, $n_{cb}/n_L \ll 1$. It is easy to show⁶¹ that the thermodynamic factor is constant⁵⁸

$$\chi_n = \frac{n}{n_{cb}} \frac{\partial n_{cb}}{\partial n_L} = \alpha^{-1} \quad (122)$$

where $\alpha = T/T_0$. For the typical values of T_0 , $\chi_n \approx 5$ at room temperature. The calculation of the jump and chemical diffusion coefficient, gives, respectively^{58,61}

$$D_J = \alpha D_n \quad (123)$$

$$D_n = \frac{N_c T_0}{N_L T} \exp \left[(E_{Fn} - E_c) \left(\frac{1}{k_B T} - \frac{1}{k_B T_0} \right) \right] D_0 \quad (124)$$

The diffusion length is usually defined for transport in a single level, as

$$L_n^0 = \sqrt{D_0 \tau_0} \quad (125)$$

being τ_0 the electron lifetime. L_n^0 is a very useful quantity that indicates the average distance that an electron travels before undergoing a recombination event.

Transient techniques that induce a gradient of the Fermi level, such as IS, IMPS, etc., provide a determination of the chemical diffusion coefficient.¹²⁴ Therefore experimentally we do not have direct access to D_0 . Similarly, when we measure the electron lifetime by transient methods we do not observe directly the decay time of carriers in the transport level. Using again quasi-equilibrium approach, the trapping and detrapping effects introduce a delay factor so that measured quantity is a response time⁴⁰

$$\tau_n = \left(1 + \frac{\partial n_L}{\partial n_{cb}} \right) \tau_0 \quad (126)$$

If the carrier density is homogeneous, we can define a diffusion length L_n from the measured parameters D_n and τ_n . Combining Eqs. (116), (125) and (126) we obtain

$$L_n = \sqrt{D_n \tau_n} = L_n^0 \quad (127)$$

Therefore, the time constants determined by the transient or frequency techniques can be used to calculate the diffusion length in Eq. (125). Eq. (127) implies that despite the variation of D_n and τ_n , the diffusion length should be constant, since the variation of both quantities has the same origin in the delay by trapping factors.⁴⁰ However Eq. (127) should be used with some points of caution: (1) the time constants depend on local conditions of carrier density (or Fermi level), therefore both D_n and τ_n should be determined in the same conditions.¹²⁵ (2) The free carrier lifetime τ_0 in Eq. (126) may include also a combination of processes by the different electron transfer channels as discussed in Sec. 5.3. Such variation of τ_0 with voltage has no counterpart in D_n and therefore L_n will not be constant.

6. Transmission line models

6.1. General structure of transmission lines

Transmission line (TL) equivalent circuits as those shown in Fig. 1 are frequently

used in Electrochemistry in connection with porous electrodes or diffusion in active electrodes.^{41,43,46,126-128} Models for nanostructured semiconductor electrodes used in DSC are described in Refs.^{46,47,49,129}.

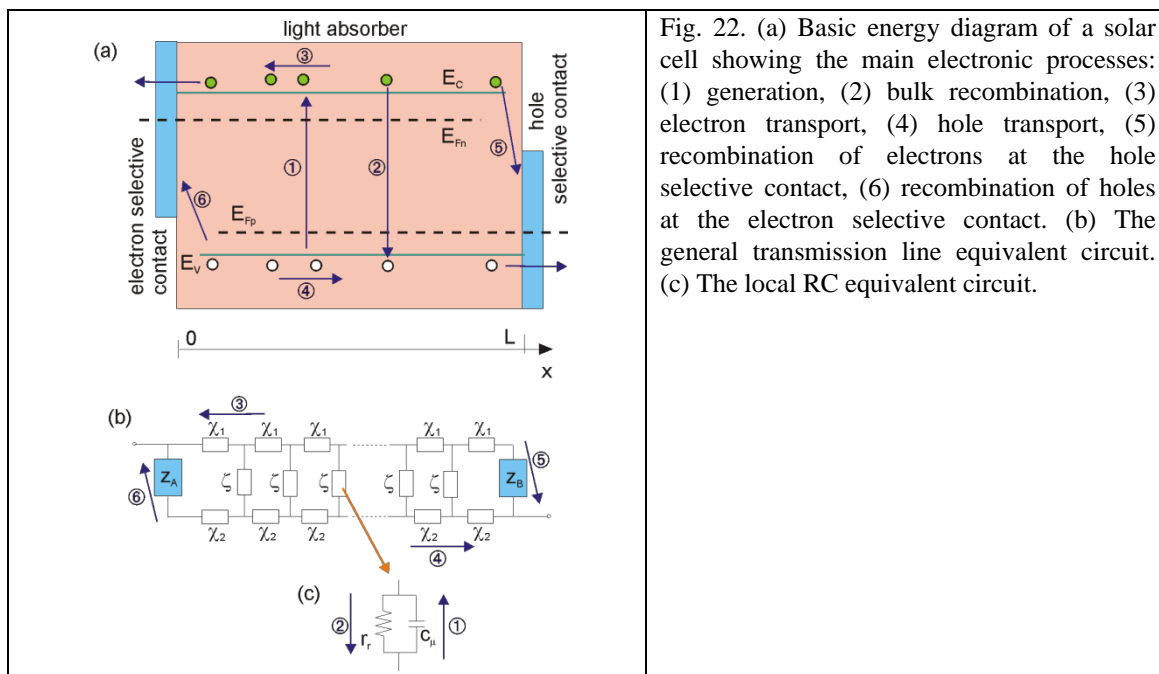


Fig. 22. (a) Basic energy diagram of a solar cell showing the main electronic processes: (1) generation, (2) bulk recombination, (3) electron transport, (4) hole transport, (5) recombination of electrons at the hole selective contact, (6) recombination of holes at the electron selective contact. (b) The general transmission line equivalent circuit. (c) The local RC equivalent circuit.

The use of TL equivalent circuits in solar cells is a consequence of the necessary spatial extension of the absorber to optimize the capture of the solar photons. This introduces the need to transport the photogenerated carriers towards the external contacts, as mentioned in Sec. 5.4. The situation, indicating the different electronic processes in an extended solar cell, is schematically shown in Fig. 22(a). Carriers generated must travel to the contact and this process competes with recombination. In addition, the outer contacts often introduce major recombination sites that must be controlled separately, since the recombination mechanism is usually different at these points.

The structure of Fig. 22(a) is a basic outline and can be realized in different ways. For example in crystalline Si solar cells electron and holes carriers travel in the same medium, and recombination at the back surface is a major point of concern.⁹⁴ Nanostructured hybrid solar cells and organic solar cells rapidly separate the charges to different transport media. Electrons and holes travel in different material phases,³³ while the transport is intercepted by charge transfer events. We will take Fig. 22(a) as a basic

reference to generally discuss the impedance models of solar cells with outer planar contacts.

Intuitively one can see that the local processes that were discussed in the fundamental model of Sec. 4.1 and Fig. 11, i.e. recombination resistance and chemical capacitance, are also present everywhere in Fig. 22(a). But due to the spatial extension, additional impedances are required to transfer the carrier from one point to the neighbor point.¹³⁰ There are, consequently, two horizontal channels for transport, corresponding to each kind of carrier. Thus one obtains the connection of Fig. 22(b) that is a TL. The TL model includes specific elements at the boundaries that account for the particular properties of recombination, at the point where one carrier should be blocked, and the other one withdrawn by the contact. Note that the TL model can also be adapted to heterogeneous models, as in porous electrodes or nanostructured solar cells. This is illustrated in Fig. 1.

In general, transport and recombination processes in solar cells with spatial extension should be described by highly nonlinear relations between the driving force (gradient or difference of electrochemical potentials) and carrier flux, such as Eq. (1). However, we have already discussed that IS uses a small perturbation over a steady state, hence all relations between difference of electrochemical potential and carrier flux are *linear*, the coefficient being a local impedance, and this is why the model may be represented as an ac equivalent circuit (we should recall that all the elements in Table 2 are linear impedances).

With reference to Fig. 22(b), we denote $\hat{\phi}_k$, the small perturbation of the electrochemical potential (in units of electrical potential) in channel k (where $k = 1, 2$), corresponding to the Fermi level of the respective carrier. We denote \hat{i}_k , the small perturbation of electrical current in channel k . As explained before, the impedance model is formulated with a set of linear relationships between $\hat{\phi}_k$ and \hat{i}_k . There are two kinds of such relationships. One kind describes variation of $\hat{\phi}_k$ with position in relation to current \hat{i}_k , in a single channel. We call such a coefficient χ_k , and it is related to the driving force for transport, so its archetypal form is a resistance (although more complex forms exist, associated to anomalous transport⁴⁸).

The other kind of relationship stands for a loss of current in one transport channel with gain in the other one. This current can basically occur (1) between different carriers in a homogeneous medium, Fig. 22, or (2) between carriers in different phases, Fig. 1.

The current, related to recombination and/or interfacial charge transfer, is in any case driven by the local difference of electrochemical potentials between the carriers. We describe this kind of process with local impedances ζ . The archetype element is an RC circuit if there is charge transfer or recombination, or just capacitance if these processes are not permitted.

The elements χ , distributed in the spatial direction of each channel, are continuously interrupted by interphase elements ζ . This combination, that corresponds to the physical probabilities for electronic events (i.e., either lateral or “vertical” displacement) in Fig. 22(a), gives rise to the characteristic ladder structure of a TL. Generally, linear equations for physical quantities varying in space with local dissipation are represented with transmission lines, for example, acoustic waves.¹³¹

In the model of Figure 22, considering a slab of thickness dx parallel to the macroscopic contact, we obtain the following equations:¹³²

$$\frac{d\hat{\phi}_1}{dx} = -\chi_1 \hat{i}_1 \quad (128)$$

$$\frac{d\hat{\phi}_2}{dx} = -\chi_2 \hat{i}_2 \quad (129)$$

$$\frac{d\hat{i}_1}{dx} = \frac{1}{\zeta} (\hat{\phi}_1 - \hat{\phi}_2) \quad (130)$$

$$\frac{d\hat{i}_1}{dx} + \frac{d\hat{i}_2}{dx} = 0 \quad (131)$$

The last equation describes the conservation of current.

It should be mentioned that a TL impedance model is derived from the preceding macrohomogeneous equations. Regardless of the morphological details of the active film, it is assumed that the carrier fluxes occur one-dimensionally, normal to the outer planar contacts. Therefore the TL must be regarded as a spatially continuous model in which the branching *does not* correspond to finite distances, or specific morphological elements in the system such as nanoparticles. Indeed, we have indicated before that the “voltage” in each channel is associated to the Fermi level (electrochemical potential) of one specific carrier, and the transport channel indicates the phase in which the displacement of such carrier occurs.

We have emphasized in Fig. 11 the importance of the selective contacts. In the TL model this is represented by the boundary conditions that complement Eqs. (128)-(131).

To realize ideal selective contacts in Fig. 22(a), the electrons must be blocked at $x = L$ and the holes at $x = 0$. Therefore

$$\hat{i}_1(L) = 0 \quad (132)$$

$$\hat{i}_2(0) = 0 \quad (133)$$

The electrode impedance Z is given by

$$\hat{\phi}_1(0) - \hat{\phi}_2(L) = Z \hat{i}_0 \quad (134)$$

where $\hat{i}_0 = \hat{i}_1 + \hat{i}_2$ is the ac electric current flowing through the cell. From Eqs. (128-134) the following expression is obtained:⁴⁹

$$Z = \frac{\chi_1 \chi_2}{\chi_1 + \chi_2} \left(L + \frac{2\lambda}{\sinh(L/\lambda)} \right) + \lambda \frac{\chi_1^2 + \chi_2^2}{\chi_1 + \chi_2} \coth(L/\lambda) \quad (135)$$

where $\lambda = [\zeta / (\chi_1 + \chi_2)]^{1/2}$.

But if the outer boundaries are not perfectly selective, then there is some flow of current between the two channels at the endpoints, that we may associate with surface recombination. Therefore in the general case we can use the following boundary conditions:⁴⁹

$$\hat{\phi}_1(0) - \hat{\phi}_2(0) = Z_A \hat{i}_2(0) \quad (136)$$

$$\hat{\phi}_1(L) - \hat{\phi}_2(L) = Z_B \hat{i}_1(L) \quad (137)$$

Z_A and Z_B are specific impedances describing charge transfer/recombination, and polarization at the boundaries. The reflecting boundary conditions of Eqs. (132) and (133) can now be stated with the particular form

$$Z_{boundary} \rightarrow \infty \quad (\text{all frequencies}) \quad (138)$$

where $boundary = A, B$. Notice that the reflecting boundary condition of Eq. (138) corresponds to an open circuit.

The general expression of the TL model with the generalized boundary conditions is the following:⁴⁹

$$Z = \frac{1}{\chi_1 + \chi_2} \left[\lambda(\chi_1 + \chi_2)S_\lambda + (Z_A + Z_B)C_\lambda + \frac{1}{\lambda(\chi_1 + \chi_2)} Z_A Z_B S_\lambda \right]^{-1} \left\{ \begin{aligned} &L\lambda\chi_1\chi_2(\chi_1 + \chi_2)S_\lambda + \chi_1[\lambda\chi_1S_\lambda + L\chi_2C_\lambda]Z_A + \chi_2[\lambda\chi_2S_\lambda + L\chi_1C_\lambda]Z_B \\ &+ \frac{1}{\chi_1 + \chi_2} \left[2\chi_1\chi_2 + (\chi_1^2 + \chi_2^2)C_\lambda + \frac{L}{\lambda}\chi_1\chi_2S_\lambda \right] Z_A Z_B \end{aligned} \right. \quad (139)$$

where the shorthand notation $C_\lambda = \cosh(L/\lambda)$ and $S_\lambda = \sinh(L/\lambda)$ has been used.

Several particular cases of Eq. (139) may be examined.

First, if we have the following conditions: (i) $Z_A \rightarrow \infty$ and $Z_B \rightarrow \infty$ at all frequencies and (ii) large conductivity in channel 2 so that the lower transport channel becomes short-circuited, then the standard double-channel TL of Eq. (135) is recovered.

Second, we assume again two conditions: (i) $Z_A \rightarrow \infty$ (reflecting boundary) and (ii) large conductivity in channel 2 so that the lower transport channel becomes short-circuited, i.e. $\chi_2 = 0$. Then we obtain the TL shown in Fig. 23(b). The following expression results:

$$Z = \lambda\chi_1 \frac{\lambda\chi_1 + Z_B \coth(L/\lambda)}{Z_B + \lambda\chi_1 \coth(L/\lambda)} \quad (140)$$

This model is also applied for diffusion with special boundary condition.¹³³

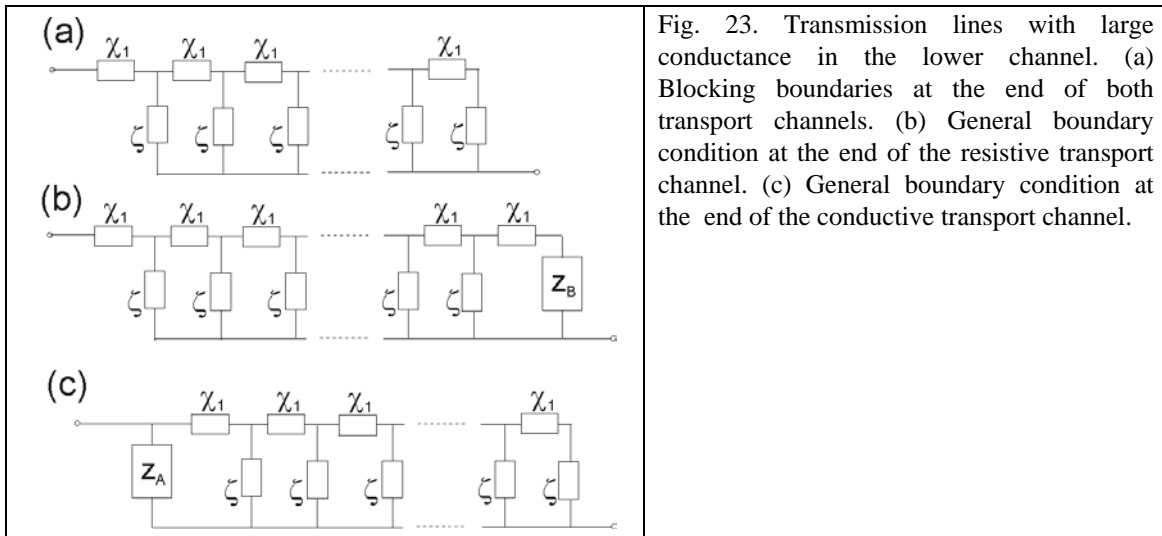


Fig. 23. Transmission lines with large conductance in the lower channel. (a) Blocking boundaries at the end of both transport channels. (b) General boundary condition at the end of the resistive transport channel. (c) General boundary condition at the end of the conductive transport channel.

Next we apply blocking boundary conditions at *both* ends of the transport channels in

the TL. We set $Z_A \rightarrow \infty$, $Z_B \rightarrow \infty$ in Eq. (140), and $\chi_2 = 0$ in Eq. (135), and we get the TL shown in Fig. 23(a), with the impedance

$$Z = \lambda \chi_1 \coth(L/\lambda) \quad (141)$$

Experimentally it is not easy to separate the transport elements in both channels of the TL.¹³⁴ Normally one channel is much more conducting than the other one, and thus the simple expression in Eq. (141) is undoubtedly the most widely used type of TL model.

Finally, Fig. 23(c) shows the case in which the generalized boundary condition is at the end of the more conductive transport channel. Note that the TL impedance is simply the parallel connection of Z_A and Eq. (141).

TL models with three transport channels have been also solved analytically.¹²⁹

6.2. General diffusion transmission lines

We turn our attention to the scheme of a DSC in Fig. 14(b) where electrons diffuse in a nanostructured semiconductor surrounded with redox electrolyte that provides for charge compensation and electrostatic shielding. We extend Eq. (4) in the following way:

$$\frac{\partial n_{cb}}{\partial t} = -\frac{\partial J_n}{\partial x} - U_n - \frac{\partial n_L}{\partial t} \quad (142)$$

Here J_n is the flux of free carriers at position x that relates to the gradient of concentration by Eq. (7), where D_0 is the diffusion coefficient of the free electrons in extended states. The third term at the right in Eq. (142) stands for trapping of the free carriers in localized states. Eq. (142) must be complemented with dynamic equations of the traps.⁷⁵

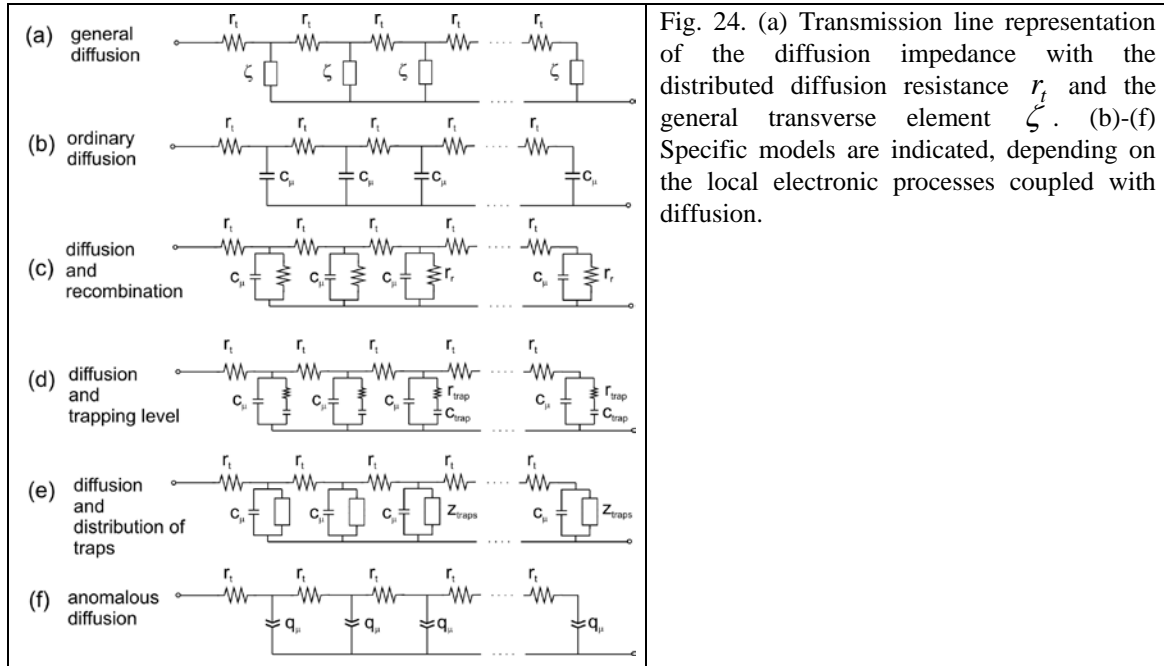


Fig. 24. (a) Transmission line representation of the diffusion impedance with the distributed diffusion resistance r_t and the general transverse element ζ . (b)-(f) Specific models are indicated, depending on the local electronic processes coupled with diffusion.

The analysis of diffusion impedance models has been presented in several works.^{47,48,135} The solution of Eq. (142) for small ac perturbation, with a blocking boundary condition, is the general expression of the diffusion impedance in a film of thickness L ,

$$Z(s) = [\zeta(s)r_t]^{1/2} \coth\{L[\zeta(s)r_t]^{1/2}\}. \quad (143)$$

where $s = i\omega$. This last equation corresponds to the TL shown in Fig. 24(a), that is a specific instance of Eq. (141). In Eq. (143) r_t is the resistivity of the material (or *distributed* transport impedance, per unit length per area) ($\Omega \cdot \text{m}$),

$$r_t = A(1-p)R_t / L \quad (144)$$

where R_t is the macroscopic transport resistance of the film of geometric area A . In accordance with Eq. (110), r_t is the reciprocal to the electronic conductivity σ_n

$$r_t = \sigma_n^{-1} \quad (145)$$

We recall that the conductivity is given by Eq. (121)

The element ζ in Eq. (143) and Fig. 24(a), adopts different forms, depending on the local processes included in the model (trapping, recombination, etc.). For example recombination, introduces a vertical resistance, Fig. 24(c),⁴⁷ and trapping, introduces the RC series connection, Fig. 24(d).^{74,75,135} In general each term that implies carrier loss from the transport level in Eq. (142), produces an additional parallel branch in ζ . So

one can obtain a variety of TL models that represent diffusion in a restricted layer coupled with additional processes, as shown in Fig. 24(b)-(e).

The element in common to all these TLs is the chemical capacitance that occurs in ζ . The origin of the chemical capacitance is the charging term at the left of Eq. (142), and this was explicitly shown in Eq. (59). It is not surprising that diffusive transport must produce always a chemical capacitance in ac conditions. A difference of potential between neighbor points in Fig. 24(b), in reality represents a difference of chemical potential. Therefore, neighbor chemical capacitors obtain different charge, i.e., concentration. This concentration gradient drives the transport of carriers across the transport resistance.¹³⁰

The model in Fig. 24(e) is special because the standard chemical capacitance is replaced by CPEs, and this is related to anomalous diffusion⁴⁸ that often occurs in disordered systems.

We discuss in more detail the simplest (ordinary) diffusion model, with no traps and no recombination, shown in Fig. 24(b). In this model the distributed admittance ζ^{-1} consists on the chemical capacitance

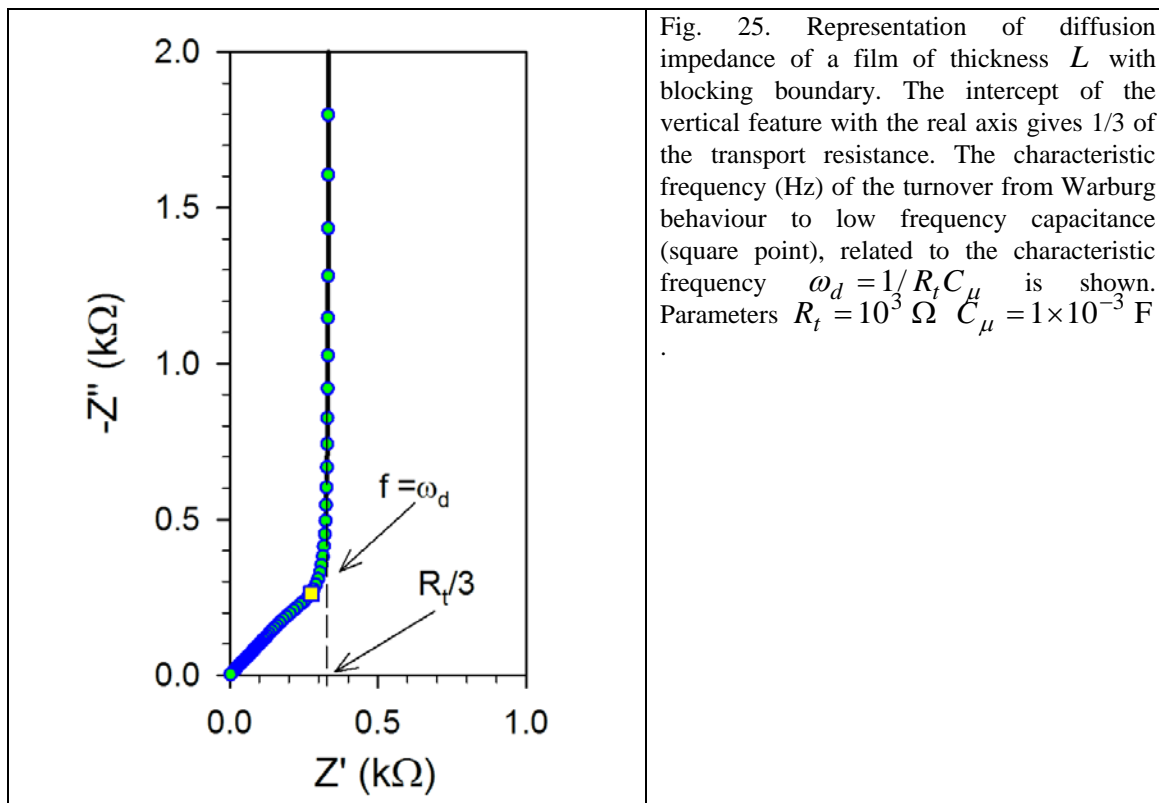
$$\zeta^{-1} = [C_{\mu}^{cb} / A(1-p)L]s \quad (146)$$

Here, C_{μ}^{cb} is the macroscopic chemical capacitance previously derived in Eq. (55). Eq. (146) gives

$$Z(s) = R_t (\omega_d / s)^{1/2} \coth[(s / \omega_d)^{1/2}] \quad (147)$$

The characteristic transport frequency ω_d is the reciprocal of the transit time through the layer of thickness L ,

$$\omega_d = \frac{D_0}{L^2} = \frac{1}{R_t C_{\mu}^{cb}} \quad (148)$$



The impedance spectrum of diffusion in a restricted layer is shown in Fig. 25. At high frequencies the spectrum exhibits a 45° line. In semi-infinite diffusion this 45° line extends indefinitely to low frequencies and is termed a Warburg impedance. In spatially restricted diffusion, at frequencies lower than ω_d there is a change of the shape of the spectrum, and Eq. (148) may be approximated as

$$Z = \frac{1}{3}R_t + \frac{1}{iC_\mu^{cb}\omega} \quad (149)$$

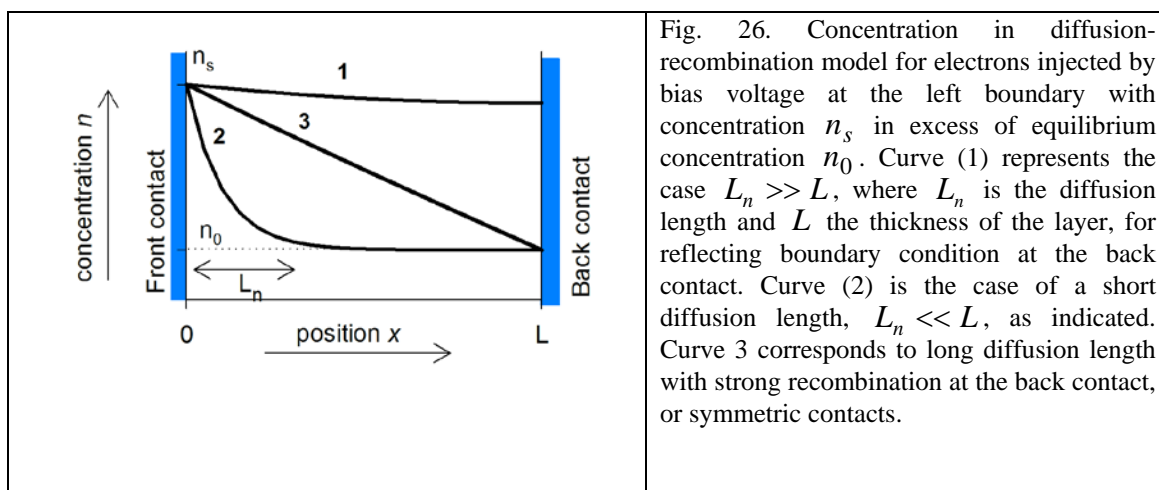
Therefore, at low frequencies the impedance becomes capacitive, and the capacitance is of course the chemical capacitance of the whole layer. The low frequency resistance is $R_t/3$. This is an important feature, since the electronic conductivity of the semiconductor layer can be directly extracted from R_t .

6.3. Diffusion-recombination transmission line

The main TL model for DSC is the diffusion-recombination model of Fig. 24(c).⁴⁷ In fact this model arises from that of Fig. 11, with ideal selective contacts, complemented with the diffusive transport, that introduces the resistances along the upper channel. This model has been applied in DSC,^{51,65} and to crystalline Si solar cells (with the addition of

surface recombination).⁹⁴

For the interpretation of the impedance of diffusion-recombination it is useful to first discuss the carrier distribution in steady state conditions. We have already introduced the diffusion length, L_n , that is defined in Eq. (125), and indicates the average distance that generated or injected electrons travel before recombining. Influence of L_n in the carrier distribution is illustrated in Fig. 26, for a semiconductor forward biased at the left contact in dark conditions.^{47,136} For long diffusion length and reflecting boundary (1), the carrier profile is nearly homogeneous. For short diffusion length (2), a gradient of carriers of the size of the diffusion length is built from the injection point. Another crucial factor is the rate of recombination at the back surface. If the rate is large (3), excess carriers cannot be maintained at this boundary, and a gradient of the size of the semiconductor layer is built.



The case of interest for DSC and solar cells in general is the diffusion-recombination impedance with a reflecting boundary condition at the end of the electron transport channel, i.e. Fig. 24(c). Recombination process introduces a recombination resistance in parallel with the chemical capacitance in the TL.⁴⁷ The transverse ζ -impedance in Eq. (143) in this case is

$$\zeta = \frac{r_r}{1 + s/\omega_{rec}} \quad (150)$$

The characteristic frequency of recombination is

$$\omega_{rec} = \tau_0^{-1} \quad (151)$$

where τ_0 is the free electron lifetime, and the distributed recombination resistance is given by

$$r_r = LA(1-p)R_r = LA(1-p)\frac{\tau_0}{C_\mu} \quad (152)$$

Here R_r is the macroscopic recombination resistance of the layer, that was discussed in Sec. 5.3. The impedance adopts the form⁴⁷

$$Z(\omega) = \left(\frac{R_t R_r}{1 + i\omega / \omega_{rec}} \right)^{1/2} \coth \left[(R_t / R_r)^{1/2} (1 + i\omega / \omega_{rec})^{1/2} \right] \quad (153)$$

The impedance spectra of the model of Eq. (153) are shown in Fig. 27. In contrast with Fig. 25, the spectra of diffusion-recombination, are resistive at low frequencies. This is due to the fact that recombination introduces a dc conduction path. There are two competing processes now, the transport across the layer (ω_d) and the carrier loss by recombination (ω_{rec}). The shape of the spectra is regulated by the factor relating the characteristic frequencies, that can be expressed in several alternative ways⁴⁷

$$\frac{\omega_d}{\omega_{rec}} = \frac{R_r}{R_t} = \left(\frac{L_n}{L} \right)^2 \quad (154)$$

The diffusion-recombination impedance provides two basic kinds of spectra, according to the conditions of Eq. (154). The spectrum for $R_t < R_r$, is shown in Fig. 27 (b)-(c), and corresponds to the carrier profile (1) shown in Fig. 26. This is the desired case for an efficient DSC at moderate forward bias.⁶⁵ The opposite case, for strong recombination, for $R_t > R_r$, is shown in Fig. 27(e). This relates to case (2) in Fig. 26. The intermediate spectrum for $R_t \approx R_r$ is shown in Fig. 27(d).

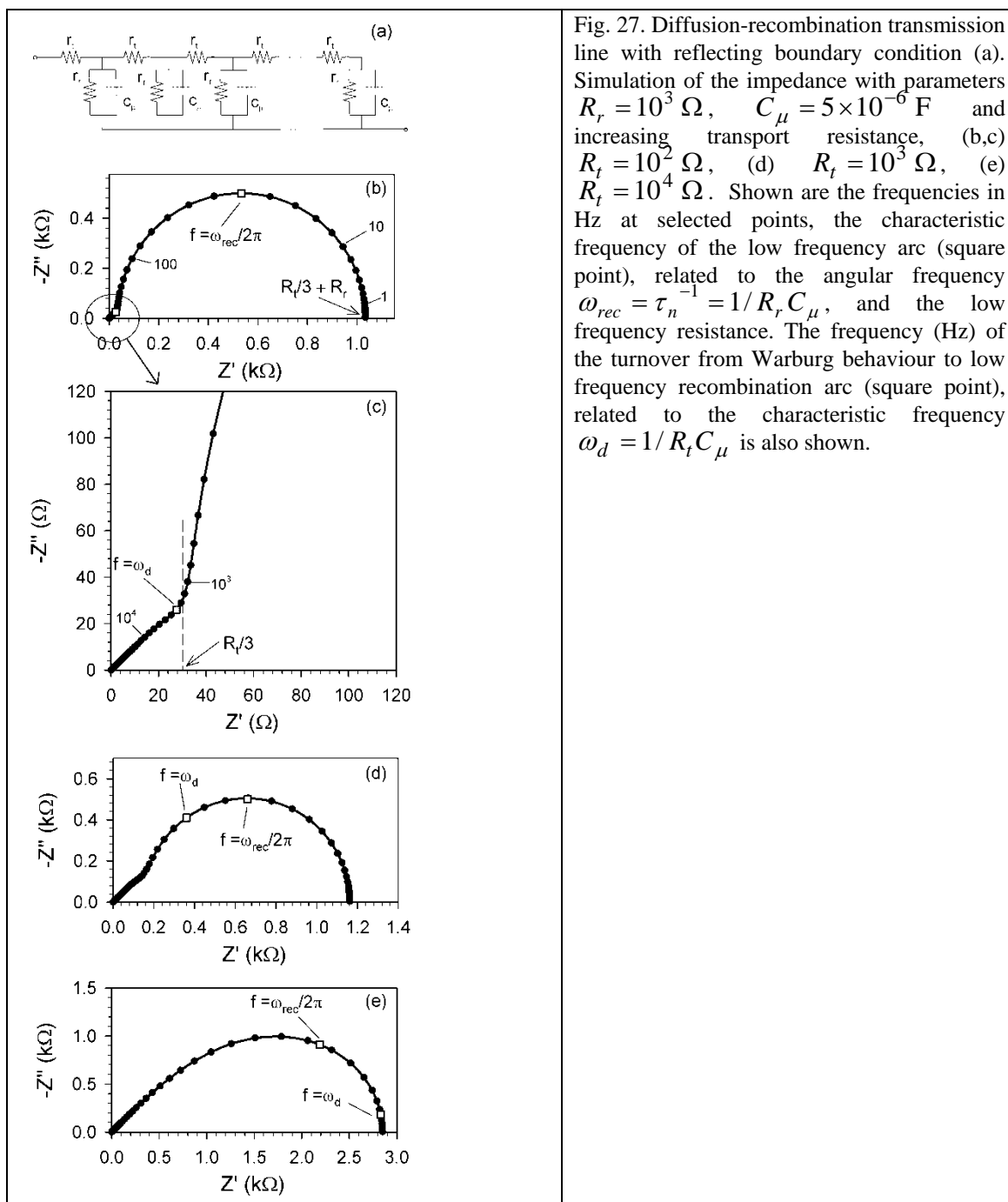


Fig. 27. Diffusion-recombination transmission line with reflecting boundary condition (a). Simulation of the impedance with parameters $R_r = 10^3 \Omega$, $C_\mu = 5 \times 10^{-6} \text{ F}$ and increasing transport resistance, (b,c) $R_t = 10^2 \Omega$, (d) $R_t = 10^3 \Omega$, (e) $R_t = 10^4 \Omega$. Shown are the frequencies in Hz at selected points, the characteristic frequency of the low frequency arc (square point), related to the angular frequency $\omega_{rec} = \tau_n^{-1} = 1/R_r C_\mu$, and the low frequency recombination resistance. The frequency (Hz) of the turnover from Warburg behaviour to low frequency recombination arc (square point), related to the characteristic frequency $\omega_d = 1/R_t C_\mu$ is also shown.

The spectrum of Fig. 27(b) has two features. At low frequency there is a recombination arc, which is the parallel connection of R_r and C_μ . The impedance at low frequency is given by the expression

$$Z = \frac{1}{3} R_t + \frac{R_r}{1 + i\omega / \omega_{rec}} \quad (155)$$

The other feature is the diffusion Warburg, which is a small feature in the high

frequency part of Fig. 27(a), clearly visible in the enlarged plot of Fig. 27(b), where we can see the start of the curvature of the capacitive part of Fig. 25 due to recombination. As indicated in Eq. (155), in the spectrum of Fig. 27(b) we can determine the electronic conductivity from $R_t / 3$, i.e., the resistance at the turnover, and this method has been effectively applied in experiments.^{52,65}

On the other hand, in the case of strong recombination ($\omega_{rec} \gg \omega_d$ or $L_n \ll L$) the injected carriers penetrate a restricted extent in the layer, and the boundary condition is irrelevant. The spectrum adopts the form of the Gerischer impedance,

$$Z = \left(\frac{R_t R_r}{1 + i\omega / \omega_{rec}} \right)^{1/2} \quad (156)$$

shown in Fig. 27(e). When the carrier distribution is strongly inhomogeneous, the chemical capacitance and recombination resistance depend on position. Furthermore, additional current generators are required to correctly describe the impedance function.

130

6.4. Parameters of diffusion-recombination model

Equation (153) is one way to write the diffusion-recombination impedance, but of course one can use other sets of parameters: the chemical capacitance, the chemical diffusion coefficient, etc. This may eventually lead to some confusion⁶⁴ and it is important to establish very clearly what is the primary information that can be obtained from the impedance spectra. We recall that recombination arc in Fig. 27(b), is a fundamental requirement of a solar cell impedance model, as discussed before in Fig. 11. However the Warburg part in Fig. 27(b) may or not be observed. So there are two basic situations.

First, the case that Warburg part is clearly observed at high frequency, in addition to the recombination arc. By “observing” we mean that there is strong evidence that the spectra display this feature, although it may be hidden by other elements.¹³⁷ But if the diffusion part is indeed detected, the impedance model provides three basic parameters: the recombination resistance R_r , the chemical capacitance C_μ , and the transport resistance R_t . If the semiconductor shows a wide distribution of traps, then in quasi-static approximation Eq. (153) is also valid but we measure the total chemical capacitance that is dominated by C_μ^{traps} , as discussed in Sec. 5.2. In any case there are *three independent impedance parameters* that can be derived from the model.

From these parameters we can additionally obtain:

(a) the electron conductivity, as discussed in Eqs. (144) and (145);

(b) the chemical diffusion coefficient, D_n ,

$$D_n = \frac{1}{R_t C_\mu} = \frac{\omega_d}{L^2} \quad (157)$$

This last equation corresponds to the generalized Einstein relation $\sigma_n = D_n c_\mu^{traps}$ that was given in Eq. (120).

(c) the electron lifetime, given in Eq. (126), that is obtained as follows

$$\tau_n = R_r C_\mu = \omega_{rec}^{-1} \quad (158)$$

We should further mention that for “long” diffusion length, we can assume that transmission line elements are basically uniform, so that macroscopic resistances and capacitance are simply related to the respective distributed TL elements by the film dimensions. While in the case of strong recombination, simulation with spatially variable elements is generally required.¹³⁰

If, in addition, we have independent information about the position of the conduction band, we can also derive the free carrier diffusion coefficient and lifetime, using Eq. (119) and (126).

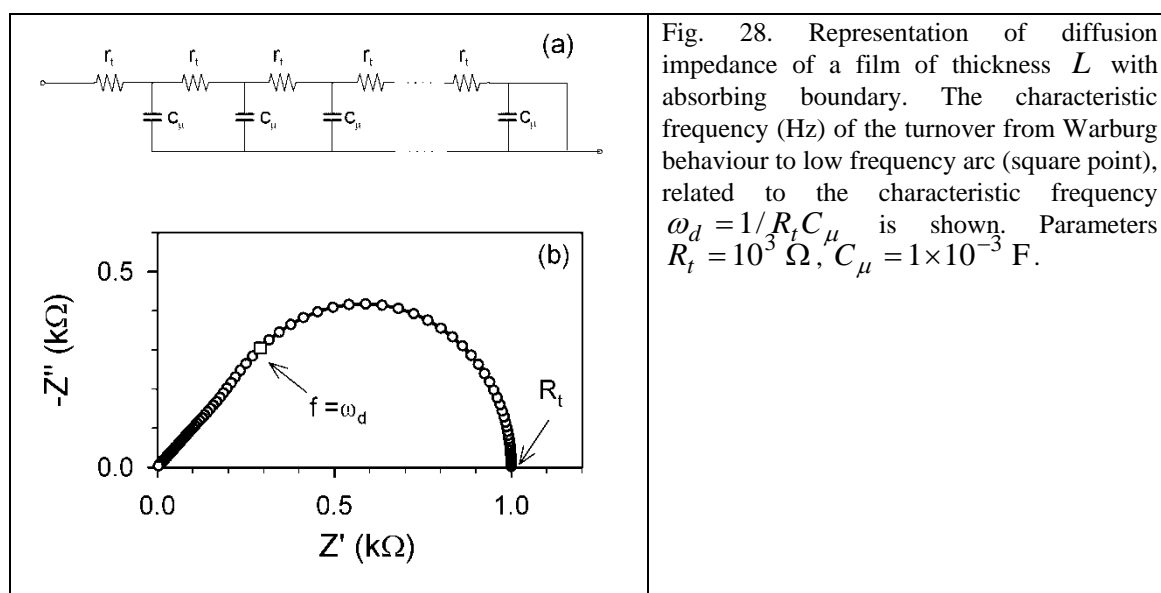
Suppose now that the diffusion, Warburg part of Fig. 27(b) is *not* observed. Then we have *two independent impedance parameters*: recombination resistance R_r , and the trap-dominated chemical capacitance C_μ . There is no information at all on electron transport. In fact the main reason why the Warburg part is not detected is that the conductivity is very high and transport resistance becomes very low. So in this case, conductivity and chemical diffusion coefficient, simply cannot be derived from the data.

6.5. Effect of boundaries on the transmission line

So far we have treated the impedance of diffusion with coupled processes, and with the condition of the reflecting boundary at the end of the diffusion zone. Case (3) in Fig. 26 shows a different situation. There is strong recombination at the final boundary, and the carriers must remain at the equilibrium level. The corresponding TL has a short-circuit at the end of the transport channel, as indicated in Fig. 28. The impedance can be obtained from (140) with $Z_B = 0$, and the result is

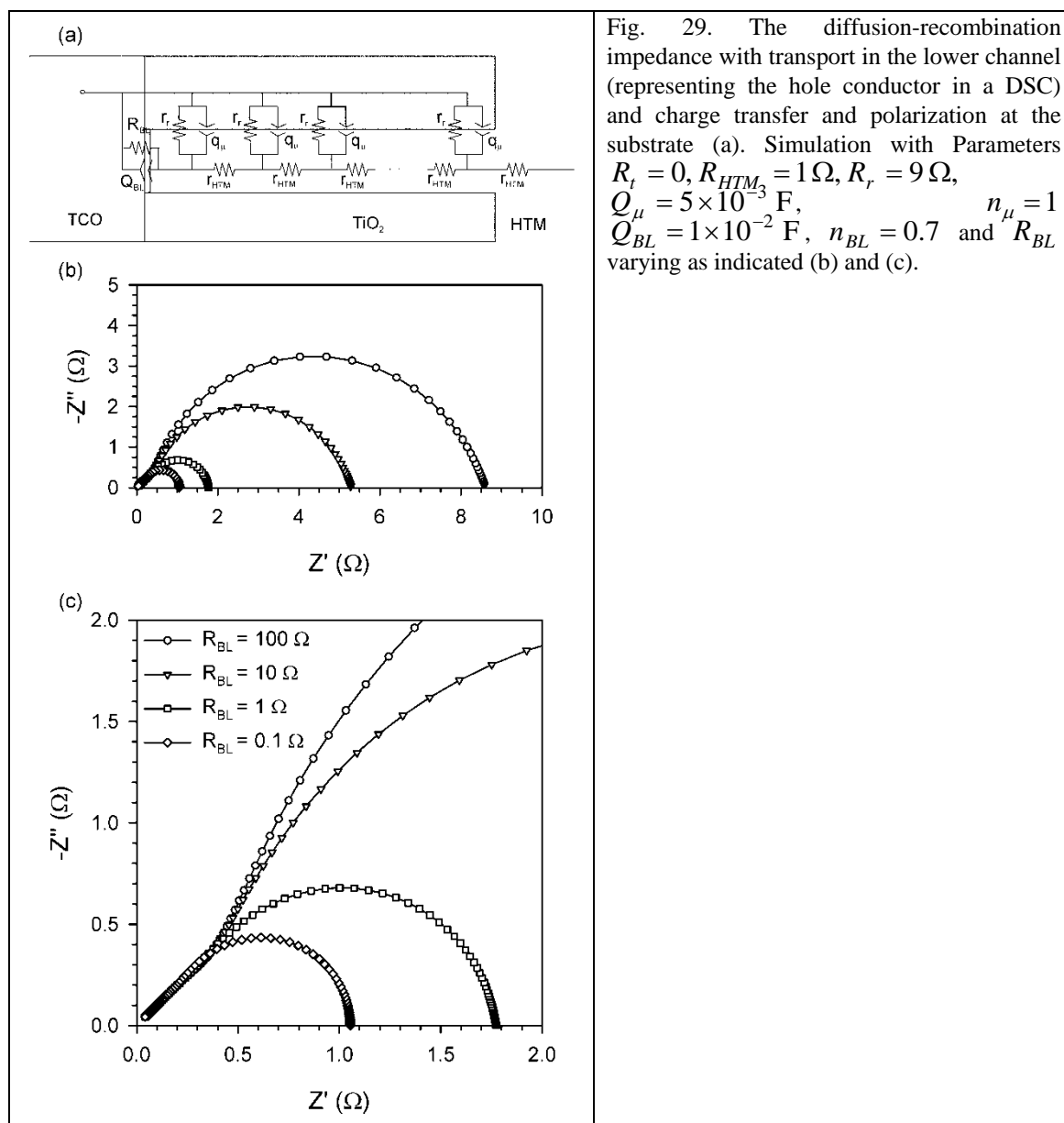
$$Z = R_t (i\omega / \omega_d)^{-1/2} \tanh[(i\omega / \omega_d)^{1/2}] \quad (159)$$

The impedance spectrum is shown in Fig. 28. There is a diffusion Warburg part at high frequencies, but at low frequencies the impedance is obviously conductive through the transport channel. Eq. (159) also corresponds to diffusion between symmetric electrodes, and this allows to determine the diffusion coefficient of ions in viscous electrolytes for DSCs.⁶⁶



In Fig. 11(c) we have commented in general the effect of recombination at one boundary of the solar cell. We can provide now a more quantitative picture of this effect using the TL model with a general boundary condition of Fig. 23(b), described in Eq. (140). As an example, Fig. 29 represents a DSC with a solid hole conductor, in which the more resistive transport channel is the organic conductor, so that the resistance of nanostructured TiO_2 is set to 0. In the contact of the organic conductor with the substrate, there is a resistive/capacitive interface, describing the direct charge transfer through the substrate. This is a short circuit that must be avoided in DSCs, where the only transfer path must be the distributed interface of TiO_2 /organic conductor. In Fig. 29(a) and (b) we present simulations of the spectra with a variation of the charge transfer resistance at the substrate. In fact the “shunt” resistance R_{BL} at the substrate can be highly variable, since the potential in the substrate changes and one can expect Butler-Volmer behaviour.⁵¹ When R_{BL} is large, the substrate plays no role at all, and we

obtain the spectrum of diffusion-reaction impedance shown in Fig. 27(b). But when R_{BL} becomes less than the bulk recombination resistance, the current flows predominantly through the substrate, and the TL model becomes similar to that of Fig. 28. The observation of a transition from one type of spectrum to another one, may be useful in practice to determine the dominant resistance at each bias voltage.



7. Applications

In this section we will apply the models and concepts explained above, to describe

the experimental results obtained for the IS measurements of several samples of DSC. Firstly the specific equivalent circuit models that have been found more useful to fit the impedance spectra of DSCs will be described. Subsequently, results obtained from these fits will be analyzed and contrasted with theory predictions. Finally, consequences of the IS data analysis on the performance of the DSCs will be commented.

The main objective is to provide the main hints and ideas for the practical application of the IS technique on devices based on this technology and similar ones.

Before starting, we want to remember the sign criteria for the bias potential that is used in this chapter. A nanostructured TiO_2 film will be always the working electrode, therefore illumination of the sample will produce a positive current under short circuit and a negative photopotential. Consistent with the previous sections, the sign of the potential will be reversed and all the equations will be written taking into consideration this change of sign.

7.1. Liquid electrolyte cells

The impedance spectra obtained for DSCs with liquid electrolyte as hole conductor based on both liquid solvents and ionic liquids, may be adjusted to the general transmission line model of Fig. 30.^{51,52,65,66}

In this model, we have used the transmission line of Fig. 24(c) that describes diffusion electrons in the TiO_2 together with the recombination with the holes in the liquid electrolyte. For DSC device application this TL is combined with a number of elements accounting for the different interfaces in the device.

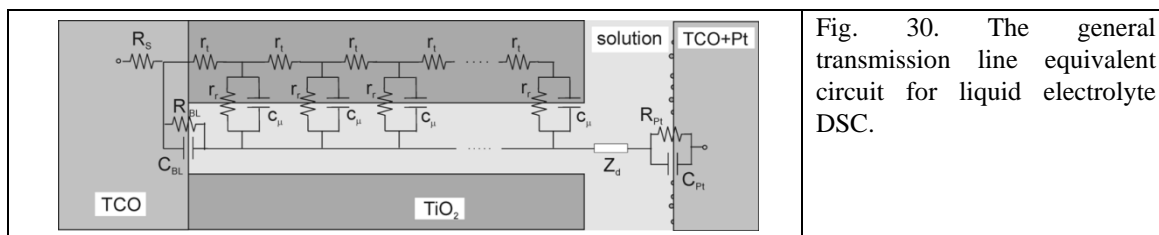


Fig. 30. The general transmission line equivalent circuit for liquid electrolyte DSC.

In addition to the elements of the TL appearing in Fig. 24(c), the following elements occur in the general equivalent circuit of DSCs (Fig. 30):

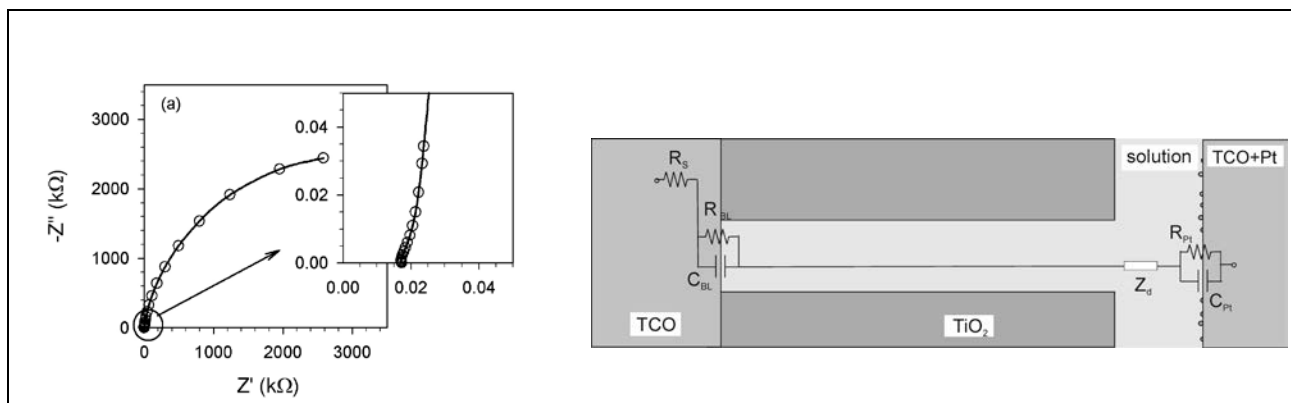
- The charge-transfer resistance R_{Pt} and interfacial capacitance C_{Pt} at the counter electrode/electrolyte interface. R_{Pt} is the resistance to regenerate the

I_3^- into I^- at the counter electrode while C_{Pt} is the Helmholtz capacitance at this interface.

- The charge-transfer resistance R_{BL} and the capacitance C_{BL} for electron recombination and charge accumulation at the contact between the part of the substrate uncovered by the colloids of TiO_2 , also known as back-layer (BL), and the electrolyte. R_{BL} represents the charge losses at the BL, while C_{BL} is the capacitance of the BL/electrolyte interface, which generally takes values similar to C_{Pt} .
- The resistance R_{CO} and the capacitance C_{CO} at TCO/ TiO_2 interface, i.e., at the nanoparticles connected to the substrate (not shown in Fig. 30).⁵⁰ These equivalent circuit elements are significant only if the contact between the semiconductor and the substrate is not ohmic.
- The resistance R_S of the conducting glass (TCO), which is associated to the sheet resistance of the TCO and the geometry of the cell.
- Finally the element Z_d accounting for diffusion of the redox species in the electrolyte: e4ay3

$$Z_d = R_d \frac{\tanh[(j\omega / \omega_d)^{1/2}]}{(j\omega / \omega_d)^{1/2}} \quad (160)$$

This is the same as Eq. (159) with $R_d = R_t$, the diffusion resistance associated to this process and ω_d the characteristic frequency of the diffusion, from which the diffusion coefficient of ions in the electrolyte may be calculated through $D = l^2 \omega_d$, with l the effective diffusion length ($l = L/2$).¹⁹



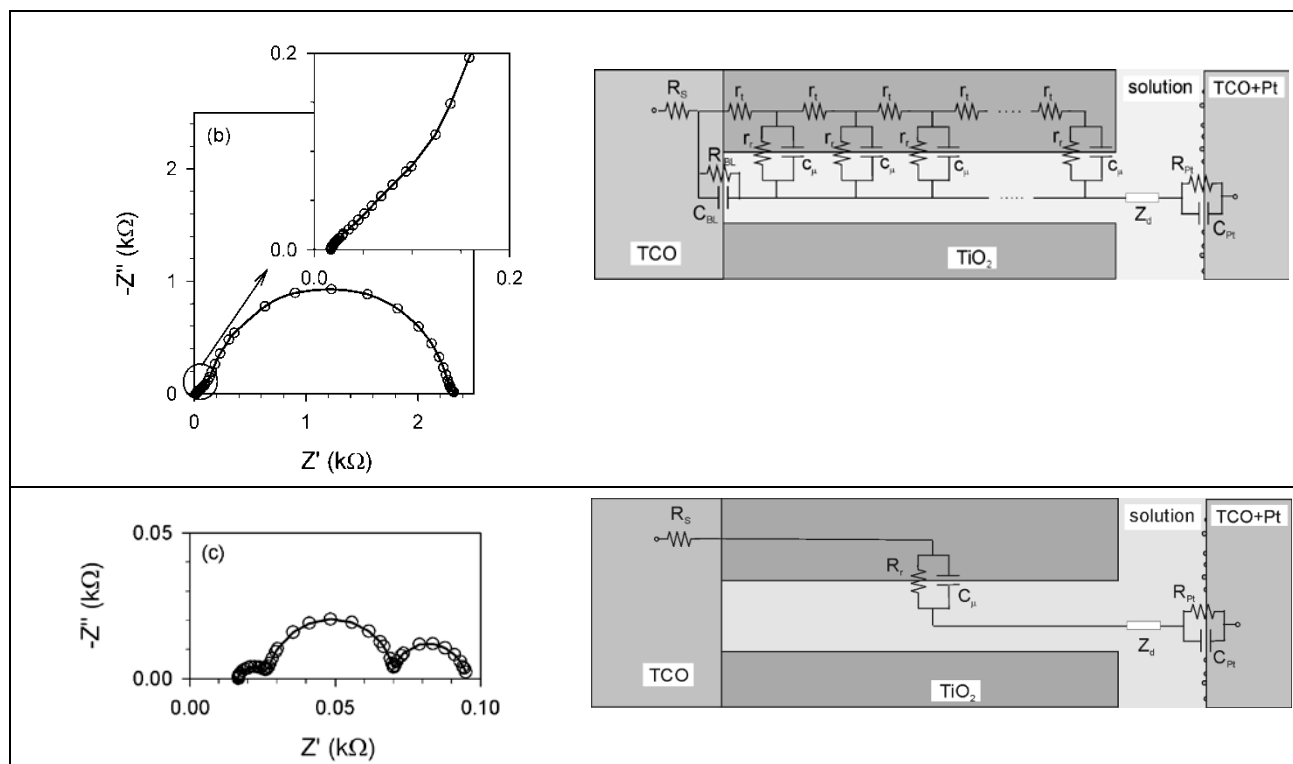


Fig. 31. Experimental IS spectra of a ionic liquid DSC (left) and simplified equivalent circuit models (right) used to fit them at different potentials in the dark. (a) At low potentials, here 0.25 V, a large arc given by the charge recombination and capacitance of the back layer dominates the impedance. At high frequencies, the small deformation in the inset of the spectrum is due to the CE. Diffusion may not be observed. (b) At intermediate potentials, here 0.55 V, the characteristic spectrum of the transmission line is observed and the complete equivalent circuit is needed to fit the impedance. (c) At high potentials, here 0.7 V, transport resistance becomes negligible and three arcs may be observed: the high frequency one associated to the counter electrode, the central one to recombination at TiO_2 surface and the last one at low frequencies to the diffusion process.

In practice, the general model of Fig. 30 may be simplified, and if possible this is very convenient, in order to reduce the number of parameters used in the fitting process.^{51,66} A first approach is to consider that the contact between the TCO and the TiO_2 is ohmic. Thus R_{CO} and C_{CO} may be suppressed. The second and most significant simplification of the model is due to the changes produced by the applied potential. The position of the Fermi level at the contact between the TCO and the TiO_2 is controlled by the external potential. Therefore we may modulate the conductivity of TiO_2 , yielding to the variety of behaviours found for the IS of DSCs shown in Fig. 31.

At low forward or reverse potentials, resistance of the TiO_2 will tend to infinite, thus contribution from the TiO_2 nanoparticles to the IS spectrum is expected to be negligible. In these conditions, as it is plotted in Fig. 31 (a), the main contribution to the IS spectrum will come from the charge transfer from the uncovered layer of the TCO (coated or not) at the bottom of the porous film. In most of the cases, at these potentials,

only a high resistance arc from the parallel combination of the R_{BL} and the C_{BL} may be appreciated while the counter electrode contribution is hidden or appears as a small deformation at the high frequency limit of this arc, inset in Fig. 31(a). The contribution of diffusion in electrolyte occurs at so low frequencies that it is not possible to be observed.

It should be emphasized that in a reverse-biased DSC, the measured current is due to charge transfer from the exposed substrate or BL to electrolyte (see below, Fig. 36),¹³⁸ while the TiO_2 is totally insulating and does not participate in the current. By these reasons, Eq. (14), that describes well the saturation current in semiconductor diodes, is not useful in DSCs.

At intermediate potentials, Fig. 31(b), the TiO_2 contributes with its full resistance and chemical capacitance. The whole transmission line equivalent circuit is needed to fit the IS data. In this case, with $R_t < R_r$, the diffusion of electrons in the TiO_2 may be observed at high frequencies as the Warburg feature, with a slope close to 1, in the inset of Fig. 31(b). (Often, the observed slope is slightly less than 1, and CPE elements are used for the chemical capacitor in order to accurately fit the data.⁴⁶) The low frequency semicircle is the result of the parallel association of the electron chemical capacitance C_μ (or Q_μ) with the charge-transfer resistance, R_r , along the TiO_2 phase. Z_d appears as a small deformation at the lowest frequencies and still is negligible. At the lower potentials of this intermediate region, R_t may be larger than R_r . In this case, the impedance of the semiconductor will behave as a Gerischer impedance element, like, Fig 27(e), Eq (156).

At higher potentials, the Fermi level in the TiO_2 may approach the conduction band enough to yield a very high concentration of electrons in the semiconductor. Then the resistance of TiO_2 becomes negligible and the transmission line equivalent circuit is reduced to a single R-C circuit, Fig. 31(c). In this situation, that is typically observed at potentials near or higher than open circuit, the impedance plots show typically three arcs as in Fig. 31(c). The high frequency arc is due to the counter-electrode charge transfer resistance and Helmholtz capacitance (R_{Pt} and C_{Pt}) parallel combination, the second arc is due to the recombination resistance at the TiO_2 /electrolyte interface and the chemical capacitance of the TiO_2 , and the third arc, that appears at the lower frequencies, is due to the impedance of diffusion in the electrolyte. The width of each of these arcs corresponds to R_{Pt} , R_{ct} and R_d respectively, while the initial displacement of the arcs

from the origin corresponds to the contribution from R_S .

We should remember that normally the transport resistance becomes quite small at high forward bias, though in some conditions it could be measured.¹³⁹ In general a separate technique based on lateral transport between two parallel electrodes is needed to measure the electron conductivity in TiO_2 at high bias.⁸¹

It has to be noted that with good electrolytes (i.e. CH_3CN based), in which diffusion coefficient is high, the third, low frequency arc may merge with the central one, yielding to a unique deformed arc. If R_d is small enough, the third arc becomes negligible.

7.2. Experimental IS parameters of DSCs

As mentioned previously, an important tool for interpretation is to monitor the variation of impedance parameters under varying bias voltage. Here we discuss the basic parameters of DSC, capacitances and resistances. We present an overview of the typical behaviour that is obtained for DSCs and we discuss the experimental results in connection with the concepts and models described in previous sections. At the end of the section, the practical way to obtain fundamental physico-chemical parameters such as diffusion coefficient, lifetime and diffusion length is given.

We should recall that the models for IS parameters on electrons in the metal oxide, are usually described with respect to the Fermi level as a parameter. Therefore, in the representation of these parameters it is important to identify the part of the voltage associated with the rise of Fermi level, by subtraction of other voltage drops such as series resistance, counter electrode, and electrolyte contributions. This practice will be followed in the magnitudes represented in this Section, for a better comparison with the theories.

7.2.1 The chemical capacitance

Typically DSC capacitance presents 3 regimes of behavior, as shown in Fig. 32. At low potentials the dominating capacitance is the combination of the capacitances from CE and BL (whether it is coated with a thin insulating layer or not). Additional contribution may be due to C_{CO} if the contact is not ohmic.⁵⁰ At intermediate potentials, the dominating capacitance is the chemical capacitance of TiO_2 , which shows a characteristic exponential variation with the potential. Eventually, at very high potentials, the capacitance of the DSC may tend to reach the surface Helmholtz

capacitance of the $\text{TiO}_2/\text{electrolyte}$ interface, C_H , that becomes smaller than C_μ at these high potentials,⁸⁷ see Eq. (73).

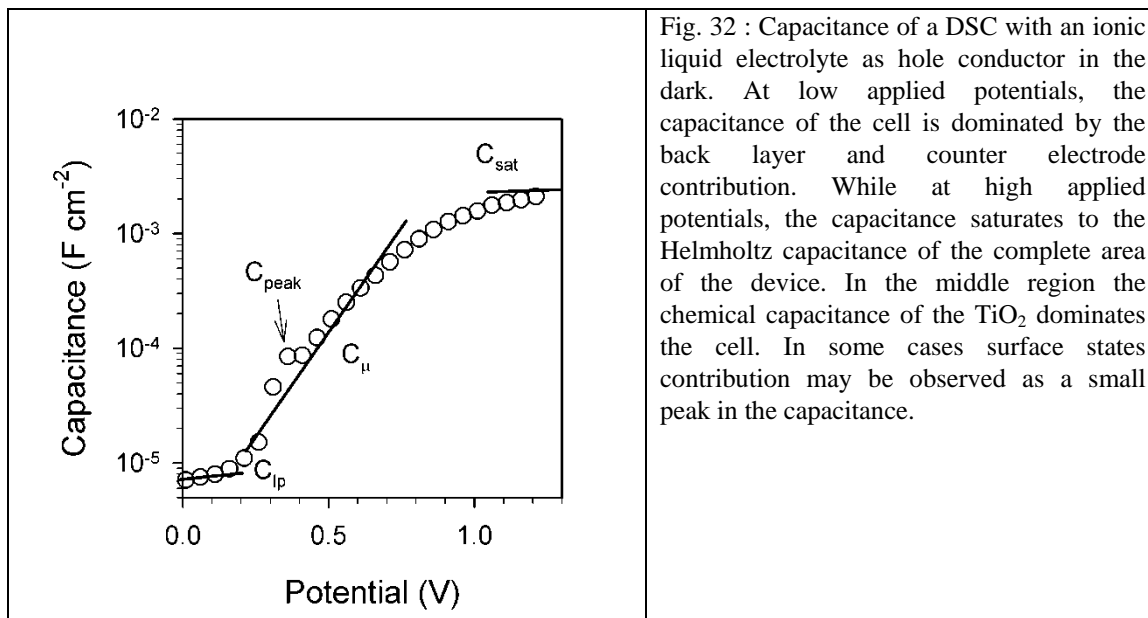
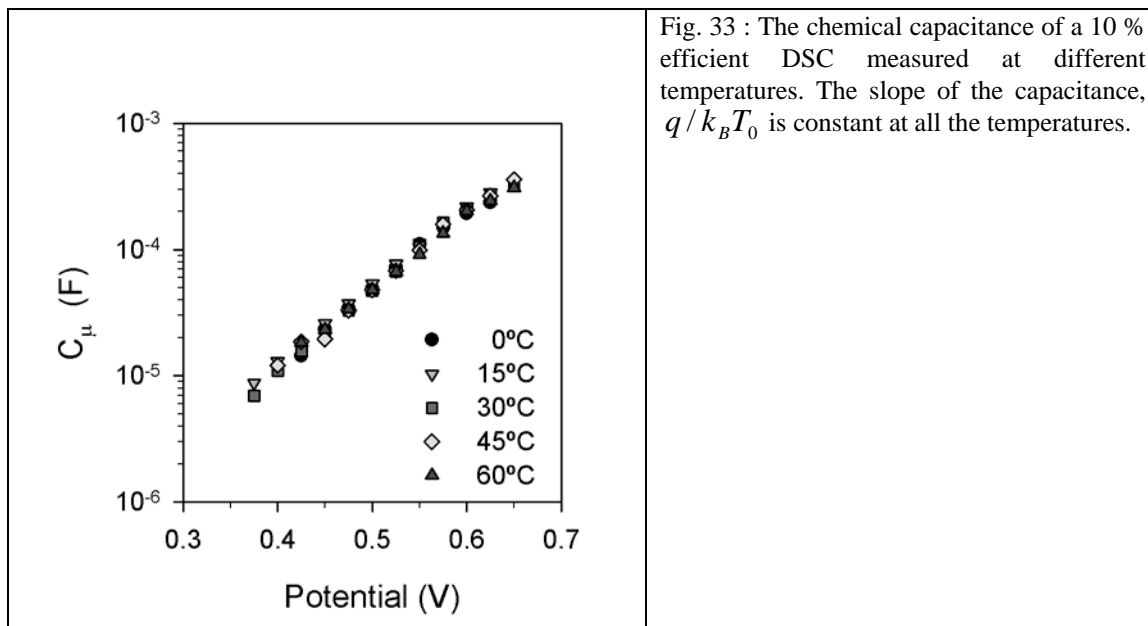


Fig. 32 : Capacitance of a DSC with an ionic liquid electrolyte as hole conductor in the dark. At low applied potentials, the capacitance of the cell is dominated by the back layer and counter electrode contribution. While at high applied potentials, the capacitance saturates to the Helmholtz capacitance of the complete area of the device. In the middle region the chemical capacitance of the TiO_2 dominates the cell. In some cases surface states contribution may be observed as a small peak in the capacitance.

In many cases, a small peak of capacitance is observed at the potentials where C_μ starts to dominate.¹⁴⁰ This peak is assigned to sub-bandgap localized states due to defects in the surface (dangling bonds, dislocations, etc.).¹⁴¹⁻¹⁴³

According to Eq. (70), the chemical capacitance describes the exponential trap distribution below the conduction band edge. This $g(E)$ is governed by the characteristic parameter of the distribution T_0 . As explained in Fig. 15 the measured chemical capacitance is governed by the DOS at the Fermi level, and this should be independent of the temperature (provided that the position of the conduction band does not change with the temperature). Experimental data of the capacitance of a 10% efficient DSC taken at different temperatures,⁶⁵ shown in Fig. 33, agree very well with the theory, providing $T_0 = 830 \pm 30$ K.



At potentials near and higher than V_{oc} (near 1 sun illumination) other contributions to the overall capacitance of the cell may be observed at the lowest frequencies. It is important to identify them as the contribution from diffusion in the electrolyte. A Bode plot of the real part of the capacitance shown in Fig. 34, may help us to determine these contributions. At low applied potentials, the low frequency limit of the capacitance is dominated by BL and CE contribution. When the bias potential is raised, the chemical capacitance contribution dominates. At the highest potentials appears the contribution from diffusion in the electrolyte. The apparent decrease of the capacitance at high frequencies (BL and CE) in the high potential plots is associated with the decrease of the charge transfer resistances in the cell as stated in Eq. (42).

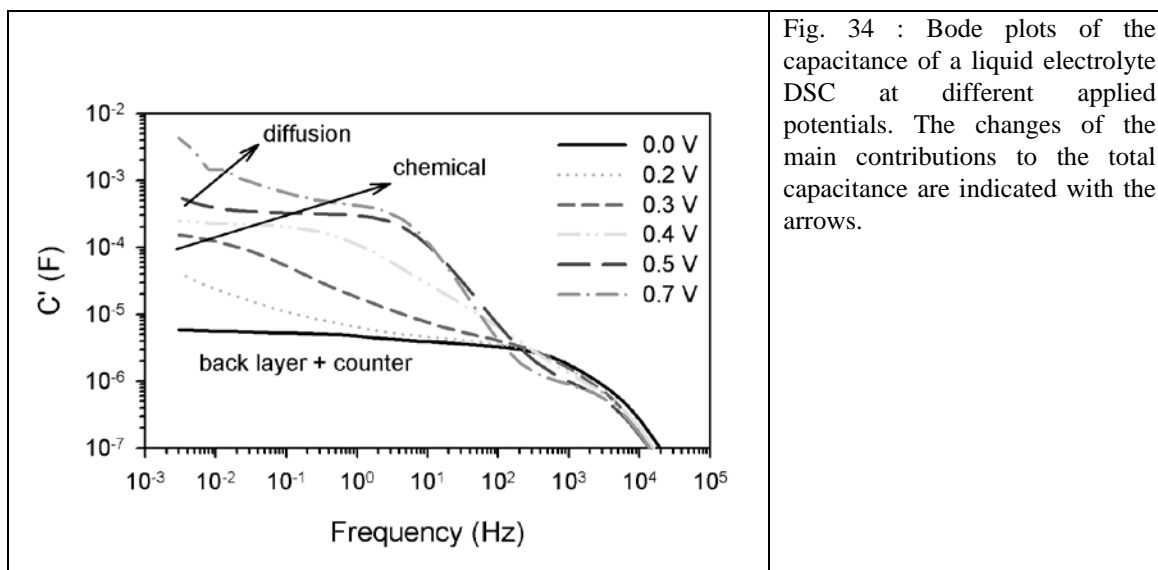


Fig. 34 : Bode plots of the capacitance of a liquid electrolyte DSC at different applied potentials. The changes of the main contributions to the total capacitance are indicated with the arrows.

In other cases, it may be observed that as the applied potential is increased, the overall capacitance drops and eventually becomes negative at the lower frequencies, as commented before in Fig. 9. An example of this is shown in Fig. 35.⁷⁶ Normally, the consequence of this effect is a limitation in the efficiency of the solar cells due to low frequency inductive contributions.

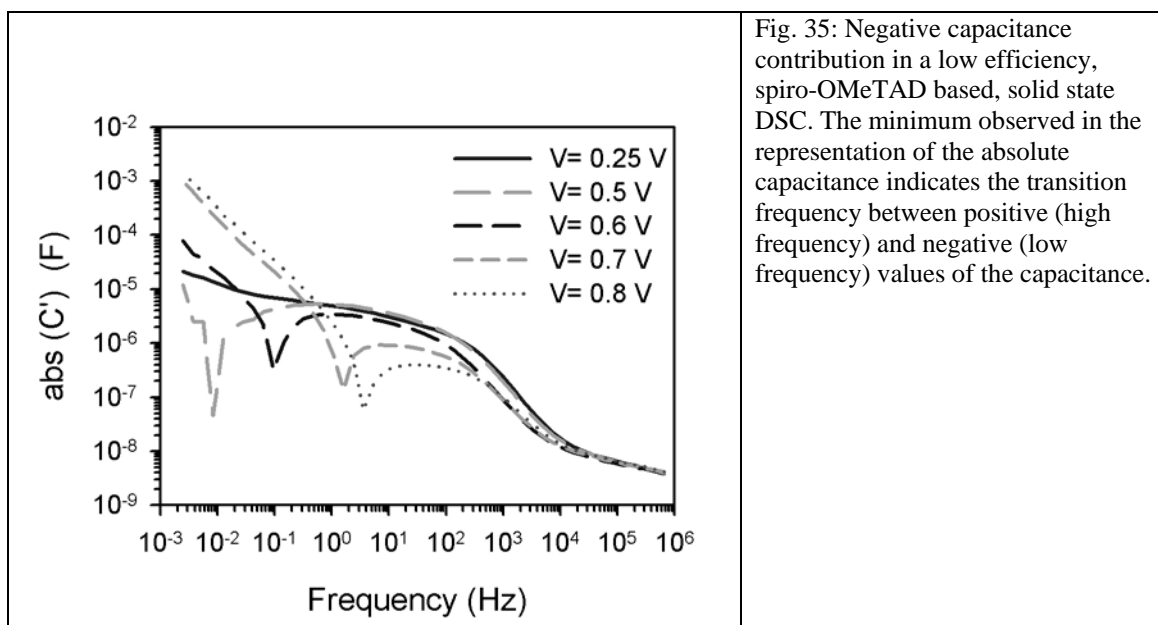


Fig. 35: Negative capacitance contribution in a low efficiency, spiro-OMeTAD based, solid state DSC. The minimum observed in the representation of the absolute capacitance indicates the transition frequency between positive (high frequency) and negative (low frequency) values of the capacitance.

7.2.2 The recombination resistance

The behavior of the overall recombination resistance R_r typically follows the trends shown in Fig. 36. At low potentials, charge transfer from the BL dominates. The BL may have different responses depending on the treatments received: precoating with

sputtered layers of dense TiO_2 , TiClO_4 treatments, polymeric coatings after film formation, etc.^{96,144} The slope of R_{BL} , generally small, is a function of both the presence of coatings and electrolyte composition. In these cases, it is easy to confuse R_{BL} with the constant R_{shunt} used in standard semiconductor based solar cells,⁷¹ as their effect on j - V curve is very similar. But we must emphasize the electrochemical origin of R_{BL} and the fact that its value is far from being constant.

At higher potentials electrons injected in TiO_2 activate the transport in this medium. The dominant mechanism of charge losses in the DSC is the recombination of the electrons from the TiO_2 large surface to the HTM. From Butler-Volmer relationship, the dependence of charge transfer resistance with the potential follows Eq. (79), yielding to a linear dependence of R_r from TiO_2 in the semi-logarithmic plot of Fig. 36.

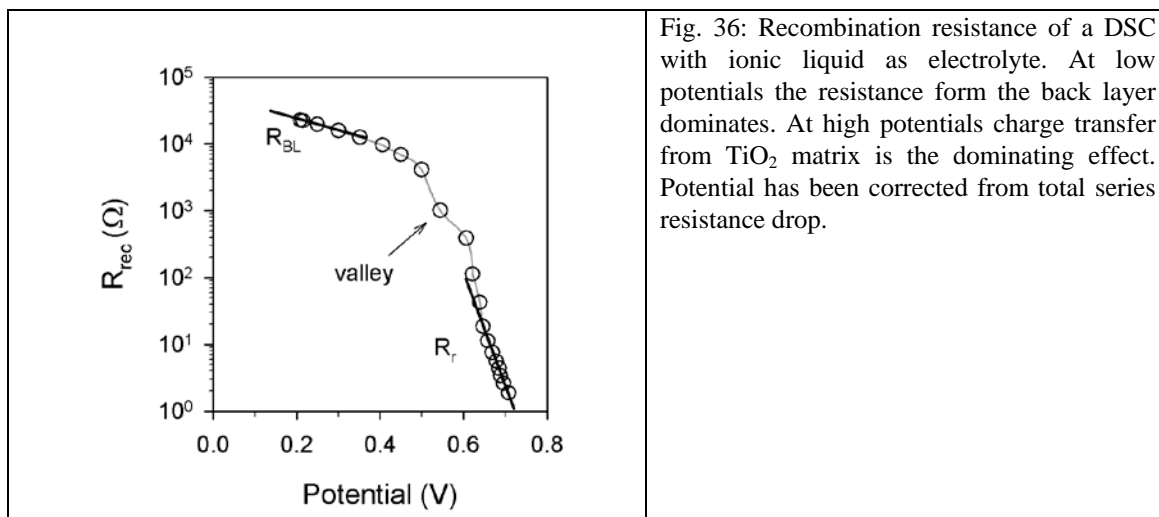


Fig. 36: Recombination resistance of a DSC with ionic liquid as electrolyte. At low potentials the resistance from the back layer dominates. At high potentials charge transfer from TiO_2 matrix is the dominating effect. Potential has been corrected from total series resistance drop.

In some cases, a valley (arrow in Fig. 36) in R_r , appears at the same potential than the peak in the capacitance of Fig. 32. This indicates recombination through the TiO_2 surface localized states described in the capacitance.⁹² In defective or aged cells, this valley may become a dominant element in the cell, and may affect in a very important manner the j - V curve.¹⁴⁵

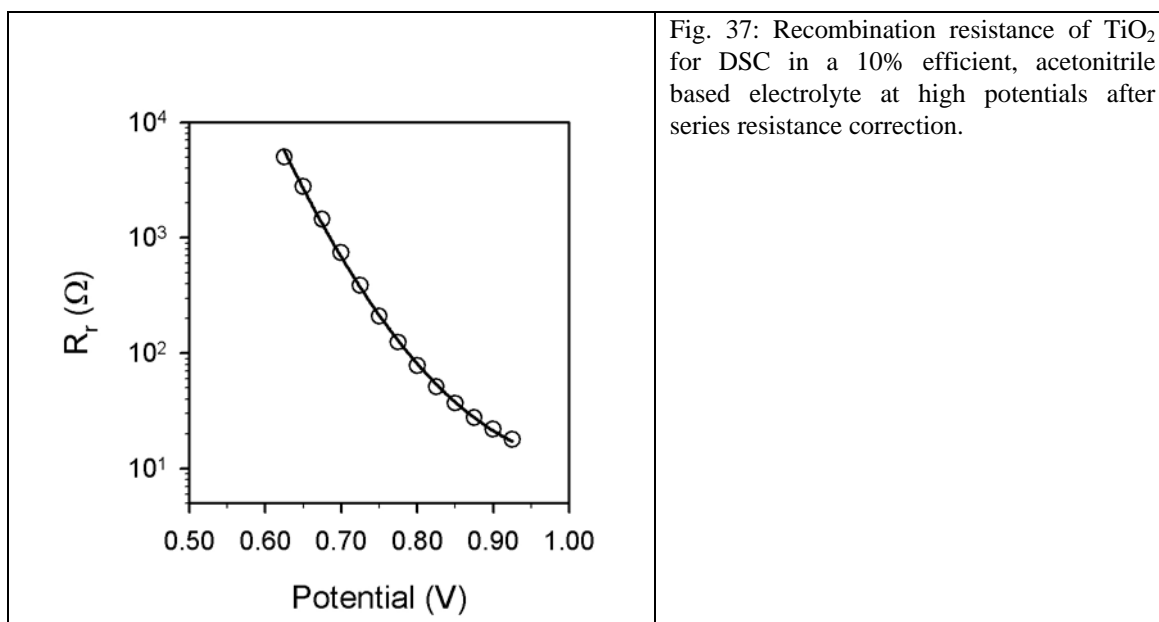
In cells where the applied potentials are higher than certain level, that depends on the redox couple used, it is needed to use the more generalized Marcus model for charge transfer resistance described by Eq. (87). In terms of the potential, Eq. (87) may be written as

$$R_r = R_0' \exp \left[-\frac{1}{k_B T} \left(q\beta V - \frac{(qV)^2}{4\lambda} \right) \right], \quad (161)$$

with

$$R_0' = \frac{T_0 \sqrt{\pi \lambda k_B T}}{q^2 L k_0 c_{ox} N_s T} \exp \left[\frac{E_C - E_{redox}}{k_B T_0} + \frac{\lambda}{4k_B T} \right] \quad (162)$$

Note that Eq. (161) provides the exponential dependence on bias indicated in Eq. (79) only if $qV \ll \lambda$, while for high enough potentials R_r deviates from the linear behavior, as shown in Fig. 20. An example of the bending of R_r is shown in Fig. 37. Using Eq. (161), a value of $\lambda = 2.0 \pm 1.2$ eV was obtained.



If we focus now the attention on the effects of temperature on R_r , it can be observed in Fig. 38 that as the temperature rises, both the overall value of the charge transfer and its slope drop.

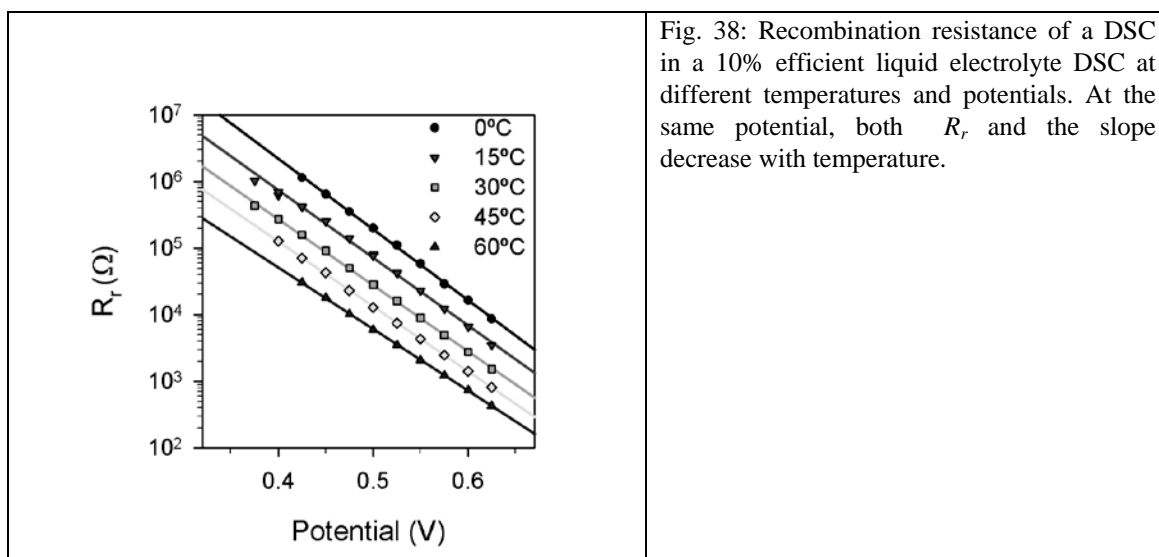


Fig. 38: Recombination resistance of a DSC in a 10% efficient liquid electrolyte DSC at different temperatures and potentials. At the same potential, both R_r and the slope decrease with temperature.

These results agree with theoretical predictions given by Eqs. (89), (161) and (162). In detail, the smaller value of R_r is the consequence of the temperature dependence of R'_0 , stated in Eq. (162). Using the values of R'_0 obtained from data in Fig. 38, from the Arrhenius plot of Fig. 39 it is possible to obtain a more accurate estimation of the value of $\lambda = 2.5 \pm 0.2$ eV. This high value of λ helps to obtain a large value of R'_0 that, as we will see later, is very important to obtain a high V_{oc} in a DSC.

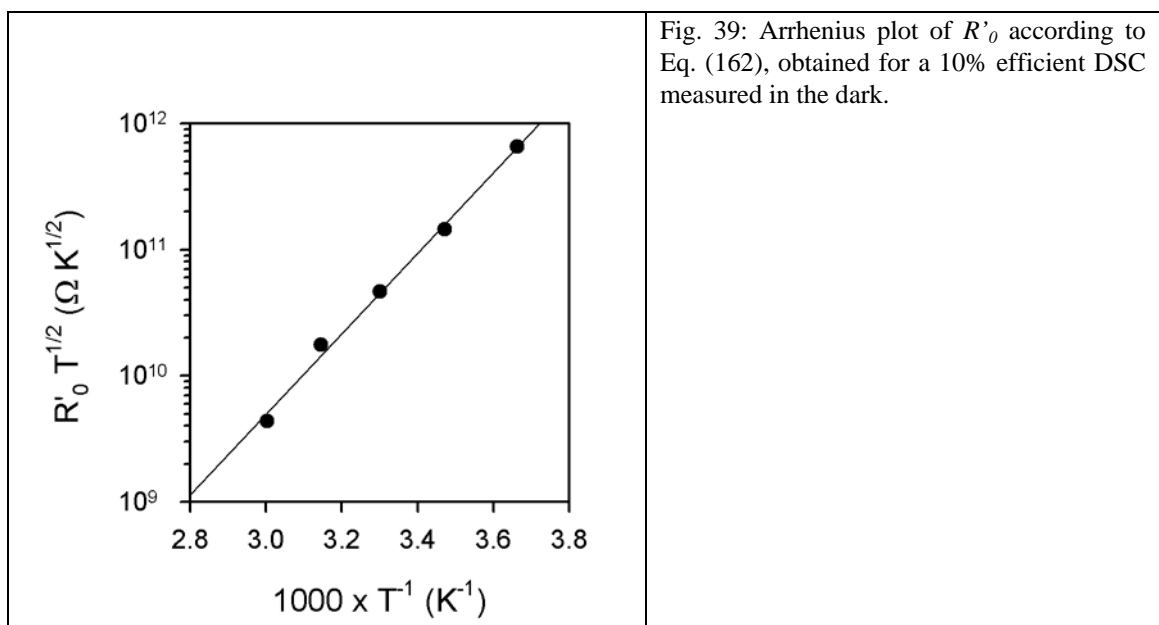


Fig. 39: Arrhenius plot of R'_0 according to Eq. (162), obtained for a 10% efficient DSC measured in the dark.

The change in the slope of R_r allows to analyse the linearity of the dependence of the transfer coefficient, β , with the distribution coefficient, α , predicted in Eq. (92). The fit

of data shown in Fig. 40 provides the experimental value

$$\beta = \frac{2}{3} \left(\frac{1}{2} + \alpha \right) \quad (163)$$

This result is similar as that stated in Eq. (92), but with a prefactor 2/3. The error in the dots makes it difficult to establish the theory without a more detailed study.

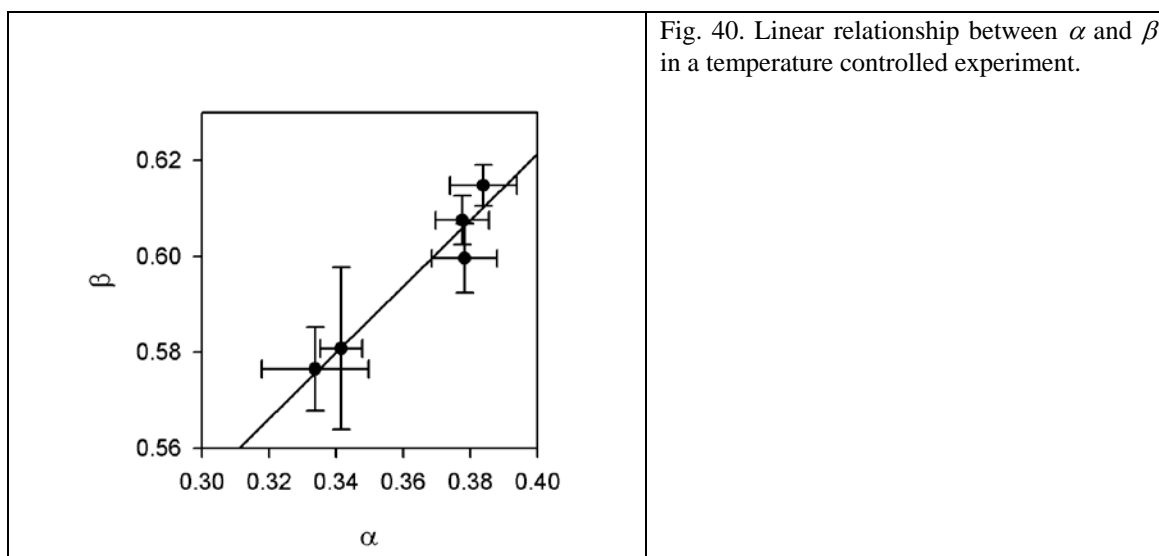


Fig. 40. Linear relationship between α and β in a temperature controlled experiment.

As it will be shown later, the lowering of R_r has a tremendous impact in the j - V curve, through the diminution of the V_{oc} . Also the slight change in the slope of R_r affects the efficiency of the cell. Most of this effect is in reducing the fill factor.

Often, IS measurements are used to compare modifications in the electrolyte, dyes, TiO_2 surface coating, etc., to evaluate the performance and properties of DSCs components and preparation routes. In general the main factor governing the performance of reasonably efficient DSCs is R_r . But it should be recognized that R_r is determined by two different aspects: the energetics and the kinetics. In Eqs. (161) and (162) these are respectively represented by the position of the TiO_2 conduction band, E_c , and the charge transfer constant k_0 . For comparing different DSC⁵¹ it is essential to distinguish both effects, and the main tool for this is the capacitance, which immediately reveals a shift of the conduction band.⁸⁷ Fortunately, the two parameters, capacitance and recombination resistance, can be routinely measured with IS, and they should be jointly analyzed when some DSC parameter is varied. If the *transport* resistance can also be measured, then a change of the conduction band readily produces changes of the conductivity at a given bias. This will be discussed shortly in more detail. Therefore in

this case we can check the displacement of the conduction band both by transport resistance and capacitance, and the results are then very reliable.

7.2.3 The transport resistance

In general both the electron and hole transport media present in the DSC may contribute with their transport resistance to the overall resistance of the cell. The different nature of the materials used for the transport of both the electrons and the holes, yields to different behaviours in their transport properties. Here the characteristic conducting properties of each of the main materials that are currently being used to build the DSCs are described.

The electron conductor

In DSC made from colloidal TiO₂, IS allows to obtain the electron transport resistance in the window of potentials (usually 200 or 300 mV) where the full transmission line behavior is observed, i.e., Fig. 31(b).

As stated in Eq. (110), the conductivity of electrons in the TiO₂ may be calculated from electron transport resistance, as

$$\sigma_n = \frac{L}{A(1-p)R_t} \quad (164)$$

Assuming that the mobility is constant and according to Eq. (84), the conductivity is exclusively dependent on the number of free electrons in the conduction band, yielding to

$$\sigma_n = \sigma_0 \exp\left[\frac{E_{F_n} - E_C}{k_B T}\right]. \quad (165)$$

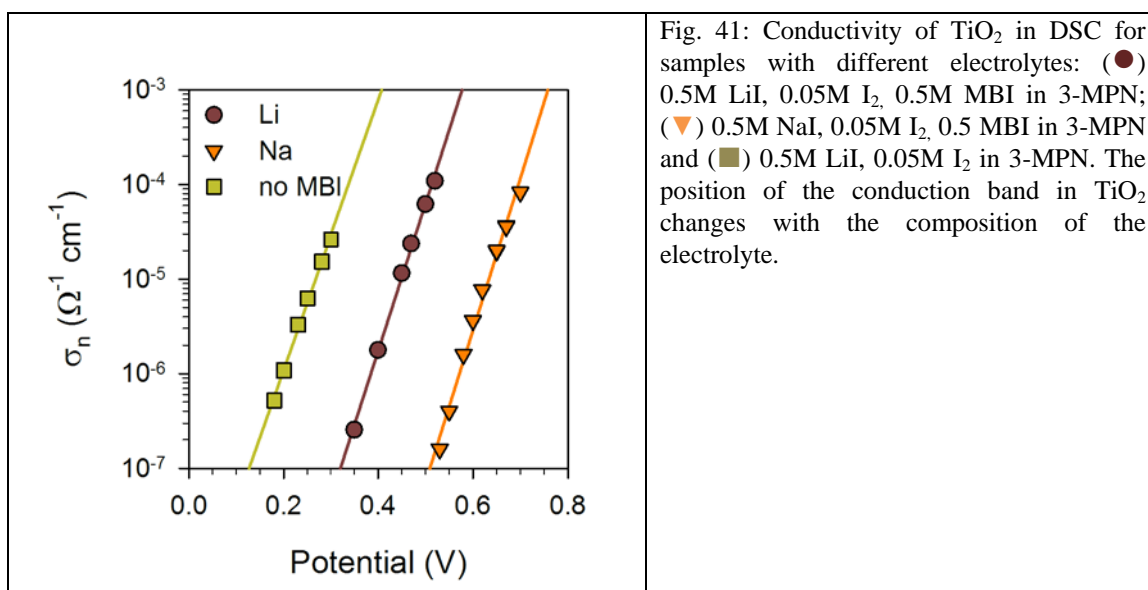
with σ_0 a constant. Then, the electron transport resistance, taking into account Eq. (18), may be written as

$$R_t = R_{t0} \exp\left[-\frac{q}{k_B T} V\right], \quad (166)$$

where R_{t0} is a constant.

Therefore, the conductivity (or R_t , if geometrical factors do not change) provides a reasonable reference of the position of the Fermi Level of the electrons (E_{F_n}) with respect to the conduction band edge (E_C) in different samples.

As mentioned before, the composition of the electrolyte, the dye used for the sensitization of the cell or the preparation method of the TiO_2 may affect the position of the conduction band. Thus the conductivity constitutes a useful index of the changes of the position of the conduction band of TiO_2 . In Fig. 41 the changes in the conductivity due to the different composition of the electrolytes may be observed. Thus, the addition of 0.5M MBI to an electrolyte containing 0.5M LiI, 0.05M I_2 in 3-MPN produces a $\Delta E_C \approx 0.2$ V. If in this new electrolyte Li is substituted by Na, a further $\Delta E_C \approx 0.2$ V is produced.



An additional effect of MBI in the DSC used in Fig. 41 is the increase of efficiency of the cell which changed from 2% in the cell without MBI to a 5% in the cells with MBI. This increase was attributed to the additional TiO_2 surface coating provided by the MBI that reduces the charge losses (increasing R_r).⁵¹

A final remark to take into consideration is that the slope of the conductivity (and R_r), $q/k_B T$, is dependent on the temperature and may change from a value near 40 V^{-1} to 25 V^{-1} upon illumination.⁶⁵

The transport resistance in the hole conductor

In liquid electrolytes, the contribution to the resistance of the hole conductor may be extracted from the diffusion resistance of the electrolyte observed in the impedance. Normally the resistance of electrolyte diffusion is decoupled from the general

transmission line model. When the diffusion coefficient is high enough the third arc associated to this process may overlap with the second one associated to recombination. In many cases, i.e. when acetonitrile is used as electrolyte and the cell spacer between semiconductor film and CE is thin ($< 40 \mu\text{m}$), R_d is small and diffusion may be completely hidden by recombination.

The increase of temperature decreases the viscosity of the electrolytes, causing an increase in the diffusion coefficient and a decrease in the diffusion resistance that favors the performance of the DSCs. As may be seen in Fig. 42, this effect also occurs when the illumination intensity is increased as illumination heats up the solar cells.

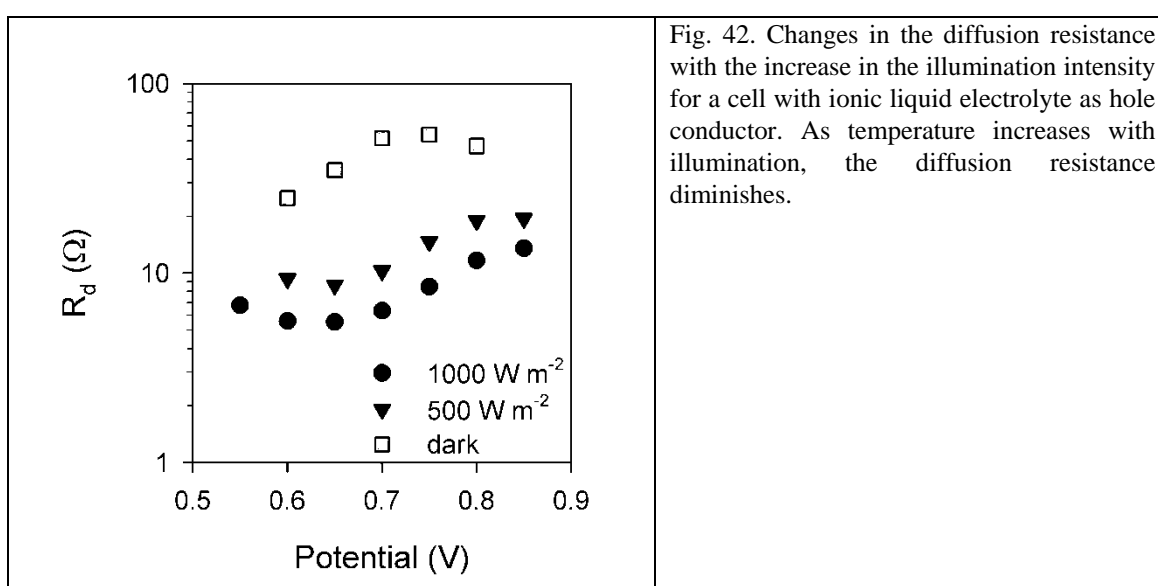
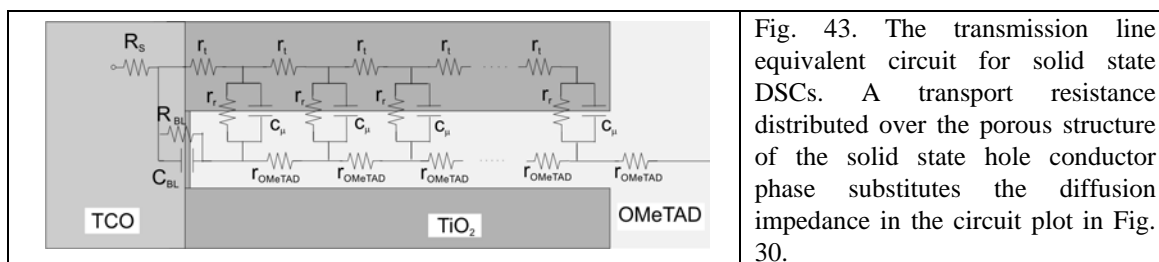


Fig. 42. Changes in the diffusion resistance with the increase in the illumination intensity for a cell with ionic liquid electrolyte as hole conductor. As temperature increases with illumination, the diffusion resistance diminishes.

The minimum of R_d in Fig. 42 for measurements under illumination occurs at V_{oc} , where the current flowing through the cell is 0.⁶⁶

In solid state cells with spiro-OMeTAD as hole conductor, the resistance of the hole conductor is higher than in the case of liquid electrolytes. At the same time the capacitance of the spiro-OMeTAD is not so high. As a consequence, the characteristic frequencies of the transport of electrons and holes are comparable and it is not possible to simplify the transmission line model as it can be done for liquid electrolytes. Now, the resistance of the hole conductor needs to be added in the path of the holes as shown in Fig. 43.



To be able of comparing the transport resistances obtained for the different hole transport media, first it is needed to normalize all of them to the geometric area. Data in Fig. 44 shows that R_{HTM} in the widely used HTM spiro-OMeTAD is around one order of magnitude higher than in the the liquid electrolyte, and this provides significant losses that decrease performance, due to the contribution of this resistance to the R_{series} and its strong effect over the FF.

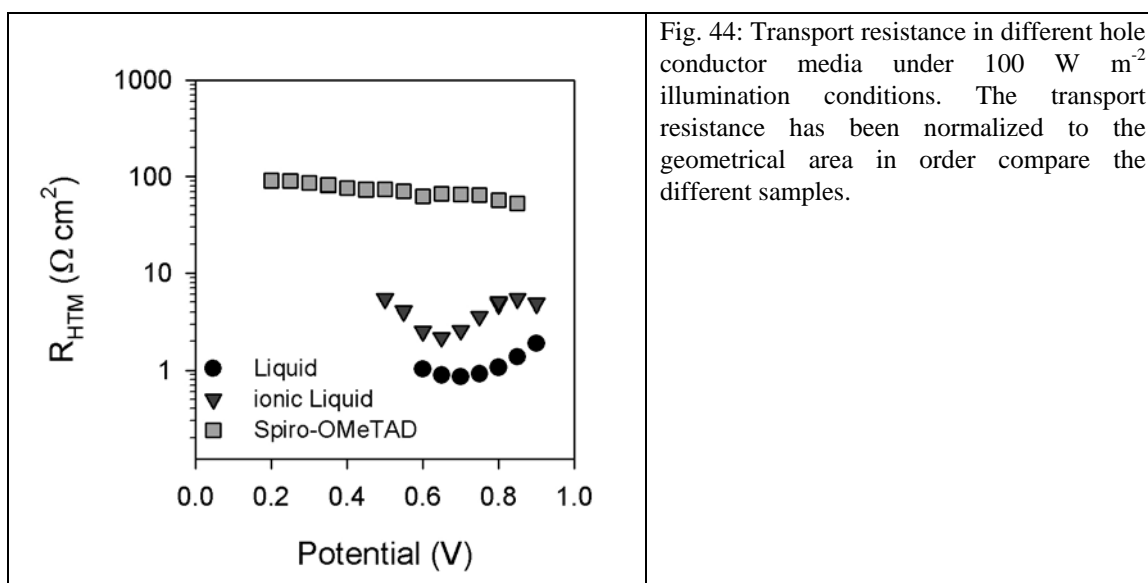


Fig. 44 also shows that the diffusion resistance of the liquid electrolytes present a minimum value at V_{oc} , as remarked before. The increase of current increases the resistance to higher values as the saturation current is approached. In the case of spiro-OMeTAD, the conductivity increases as the population of holes increases due to a slight displacement of the E_{Fp} with the applied potential

7.2.4 Time constants and diffusion length

As stated in Eqs. (157), (158) and (142), with the parameters obtained from impedance spectra, R_t , R_r and C_μ , we can calculate the basic electron transport and recombination parameters: D_n , τ_n and L_n . These last set of parameters are frequently used in the literature, due to several reasons.

The chemical diffusion coefficient D_n can be related to fundamental models for transport in disordered materials.^{61,139,146} Further, the main time constants of the DSC,⁴⁰ i.e. the transit time $\tau_d = L^2 / D_n$ and the electron lifetime, τ_n , can be calculated by several independent methods (as explained in the chapter by Peter), such as IMPS,⁵⁶ IMVS,^{28,147} V_{oc} decays,^{54,57} and this is useful to validate the results obtained by any of the methods. Finally, comparing τ_d and τ_n , or L_n with respect to L , is a useful tool to evaluate the collection efficiency of the DSC.¹⁴⁸⁻¹⁵⁰

Before we describe the characteristic behavior of these parameters, we remark, as in Eq. (47), that the use of constant phase elements (given by Q_μ , n) instead of C_μ in the fits of IS data, requires a more general definition of the kinetic constants derived from the basic impedance parameters. The diffusion coefficient of Eq. (157) has to be calculated using

$$D_n = \frac{L^2}{(R_t Q_\mu)^{1/n}}, \quad (167)$$

and Eq. (158) given for lifetime of electrons in TiO_2 has to be re-written as

$$\tau_n = (R_r Q_\mu)^{1/n}, \quad (168)$$

Equating this expression to Eq. (64) it is possible to calculate an equivalent capacitance as

$$C_\mu = \frac{(R_r Q_\mu)^{1/n}}{R_r} \quad (169)$$

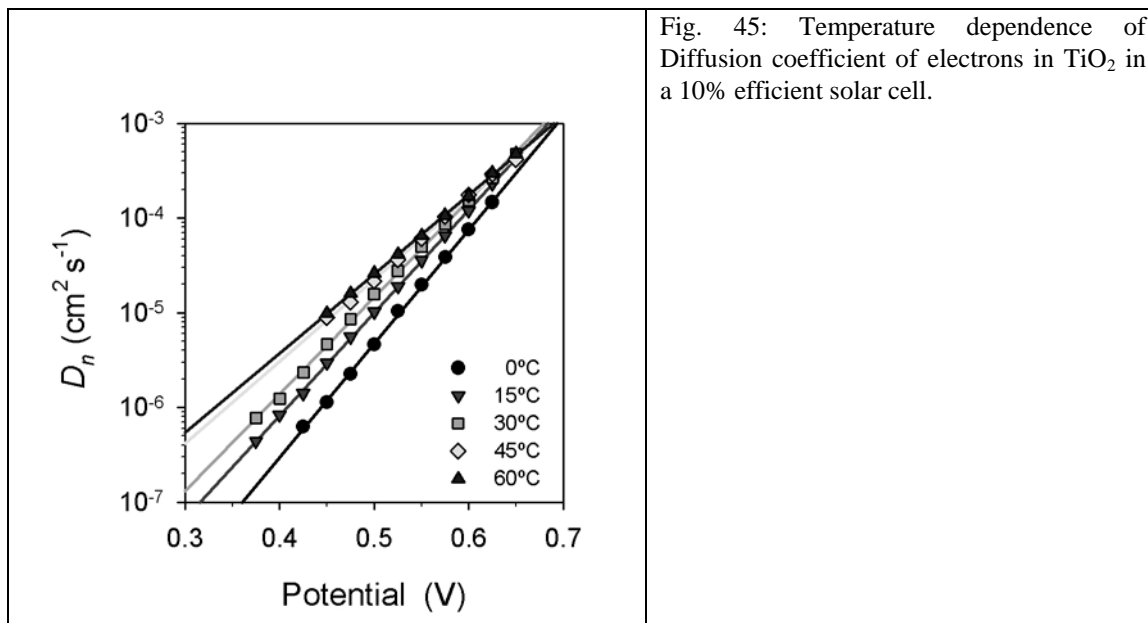
Finally, the diffusion length of Eq. (154), now is given by

$$L_n = L(R_r / R_t)^{1/2n}. \quad (170)$$

Note that all these expressions take the form derived previously when $n = 1$. Similar corrections may be used to calculate the characteristic regeneration time or interfacial capacitance at the counter electrode.

Diffusion coefficient data measured at different temperatures and calculated using Eq. (167) are shown in Fig. 45.⁶⁵ Very good agreement with Eq. (124) is found, with the slope of the plot being $[1 - \alpha] / k_B T$. Similar variation of the chemical diffusion

coefficient with the temperature have been reported in other works with high efficiency DSC.¹⁵¹



These results support the idea that the transport mechanism in the nanostructured TiO₂ is dominated by multiple trapping of electrons from the conduction band in the localized available states below this band.^{40,65,119} This theory has been confirmed by several methods^{124,152-154} and is currently the most accepted one.

The time constants are frequently used to compare the characteristics and quality of different solar cells.¹⁵⁵ The next data shown in this section will use the values of D_n , τ_n and L_n data obtained from IS with this purpose. But again we must remark that factors such as the method of preparation of the materials or the electrolyte composition change the position of the conduction band of the metal oxide with respect to the Fermi level or redox potential of the hole conductor. This fact implies that the potential is not always a good reference for comparing the response of the different cells. It is more convenient to represent the different data with respect to the relative position between the Fermi level and the conduction band, $E_{Fn} - E_C$. The rationale for this is that the kinetic parameters should be compared in conditions of equivalent number of electrons in the various solar cells. One way to correct this change is to displace the applied potential by the amount ΔE_C produced in each sample, however this quantity is not always available. As given by Eq. (165), it is reasonable to take the electron conductivity as a reference of the

energy difference between E_{Fn} and E_C . Thus the characteristics of the samples may be compared when the conduction band is filled with the same amount of electrons (i.e., $E_{Fn} - E_C = \text{constant}$).

Using this procedure we present in Fig. 46 the diffusion coefficient, lifetime and diffusion length of several DSCs. Three of them that were made with different liquid electrolytes are named L5Li, L10 and L11 and yielded efficiencies of 5%, 10% and 11%, respectively. The DSC denoted IL7 was a 7% efficient cell with an ionic liquid electrolyte and the solar cell Ometad4, was a solid state spiro-OMeTAD based DSC, 4% efficient.

Note that the data have been taken from measurements in the dark in order to obtain a reasonably sufficient number values of the transport resistance. Under high illumination intensities it becomes very difficult to distinguish the contribution of R_t to the impedance spectra from other resistive elements.

The diffusion coefficients of the different samples, Fig. 46(a) take very similar values in all the cases. Therefore, factors such as the hole conductor composition or charge screening ions have a small effect on electron transport. The situation may be different when strong forward current flows in a DSC.

Remarkable differences between samples of high and low efficiency may be observed from the lifetime data shown in Fig. 46(b). As a consequence, also important changes are observed in the diffusion length plot in Fig. 46(c).

The samples with lower efficiencies (Ometad4 and L5Li) presented the shorter lifetimes and diffusion lengths. It is clear in this case that the efficiency is to be limited by the greater losses they present with respect to the high efficiency samples. In particular, in the case of the spiro-OMeTAD based solid state DSC, maximum diffusion length is limited to 3 μm , what determines the portion of the film thickness that is actually able to collect charge efficiently.

Samples with efficiencies between 7% and 11% (IL7, L10 and L11) presented very similar characteristics in the dark, and it is not straightforward to find the reason yielding to their difference in efficiency. In the case of the sample with 11% efficiency, it may be distinguished a slightly higher lifetime and diffusion length, that means a slightly better quality of the film. Assuming a similar behavior of these parameters under illumination, the differences in the efficiencies of the cells have their origin in the differences of the dye absorption (K19 in IL7 and N719 in L10 and L11) and electron

injection into the TiO_2 , that provides higher values of current and potential.⁶⁸

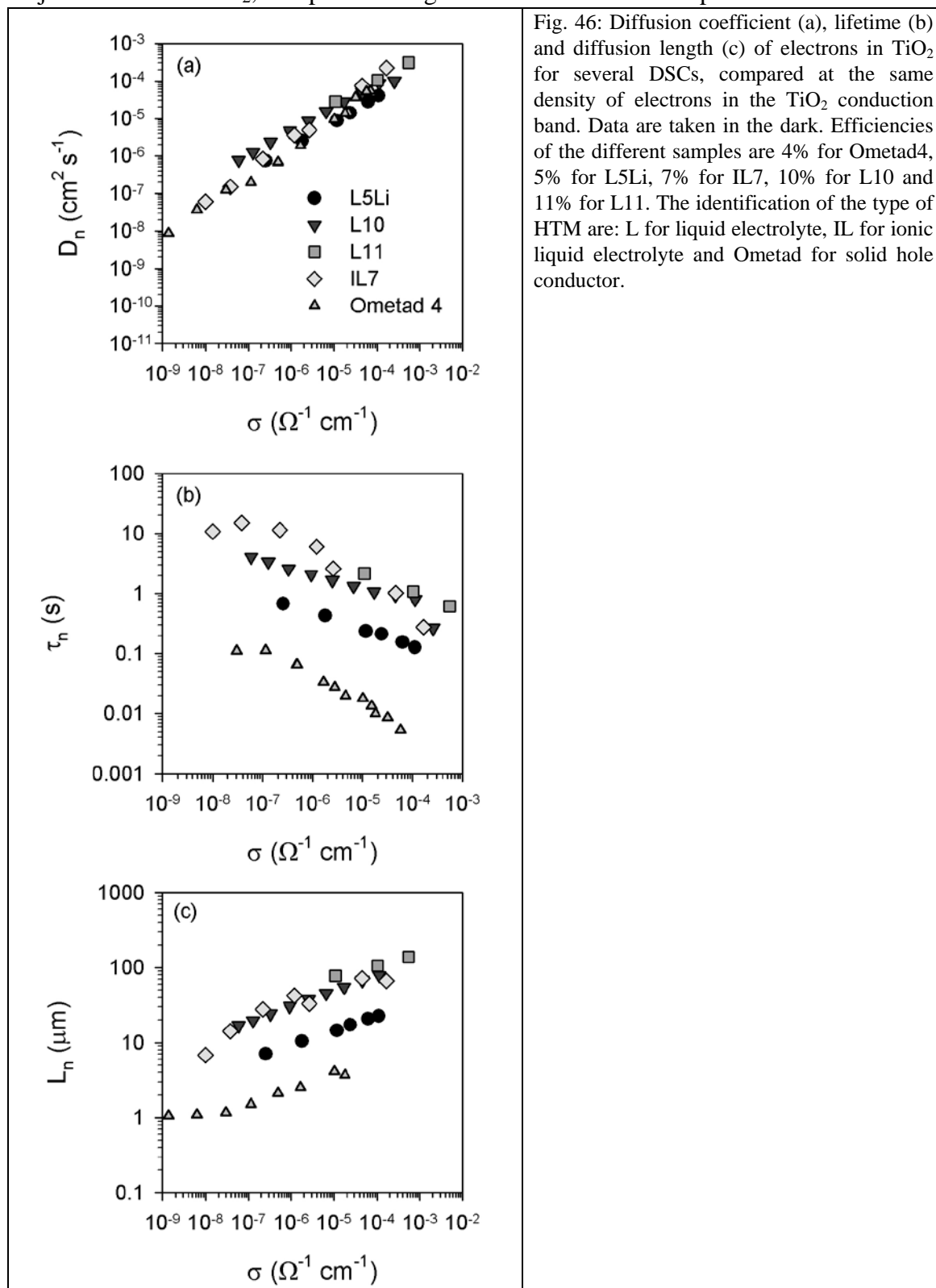


Fig. 46: Diffusion coefficient (a), lifetime (b) and diffusion length (c) of electrons in TiO_2 for several DSCs, compared at the same density of electrons in the TiO_2 conduction band. Data are taken in the dark. Efficiencies of the different samples are 4% for Ometad4, 5% for L5Li, 7% for IL7, 10% for L10 and 11% for L11. The identification of the type of HMT are: L for liquid electrolyte, IL for ionic liquid electrolyte and Ometad for solid hole conductor.

While it is customary to analyze the performance of DSC in terms of the time

constants mentioned before, and this is convenient in some respects (especially if the diffusion length is short), it should be emphasized that the differences in the characteristics of the DSCs shown in Fig. 46 have their origin in the values of the recombination resistance, as can be seen in Fig. 47. To compare the different cells, it is important to use the volumetric recombination resistance. Thus, the recombination resistance rises from Ometad4 sample to L5Li and then to the rest of the samples. Consistent with the highest energy conversion efficiency, L11 is the one that has the higher r_r .

Therefore, concerning DSC performance in general it should be concluded that once the dye provides the charge injection level in the cell (and assuming that dye regeneration is fast), it is the charge transfer from TiO_2 to the hole conductor the main process that determines the potential of a particular cell to perform at a certain efficiency. This aspect will be treated in more detail in last section.

In particular, in the case of the spiro-OMeTAD solid state solar cell, any enhancement of the cell has to deal with an increase of R_{rec} or the use of materials with higher conductivity that allow to increase the diffusion length of carriers in the metal-oxide semiconductor.

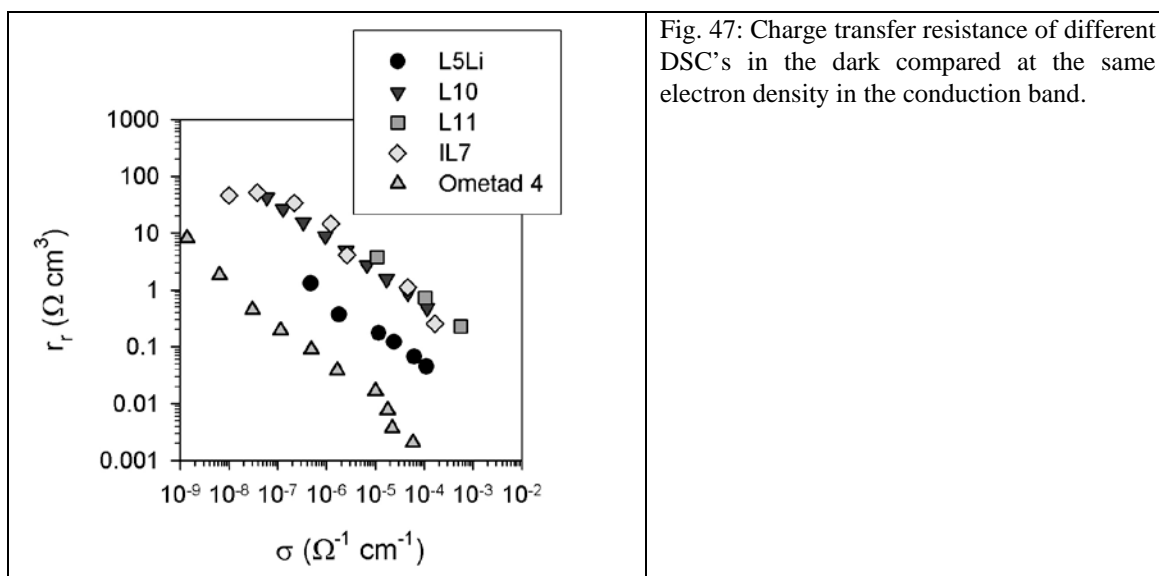


Fig. 47: Charge transfer resistance of different DSC's in the dark compared at the same electron density in the conduction band.

7.3 Nanotubes

It is believed that an improvement in the structural order of the electron conducting

metal oxide networks may enhance their electronic transport characteristics, and provide better efficiency of DSCs. A number of structures have been prepared and used including nanorods, whiskers, and nanotubes, among which the last ones are the most promising.¹⁵⁶⁻¹⁶¹ In this section we will describe results on carrier transport and charge accumulation in TiO₂ and ZnO nanotubes.

7.3.1 TiO₂ nanotubes

IS measurements have been performed to study the behavior of the electrical properties in a 10 μm long TiO₂ nanotube of 100 nm external diameter and 22 nm wall thickness.⁶⁷ Measurements were done in an aqueous solution at pH 11 in order to analyze the transport and accumulation of charge in the nanotubes.

Experimental IS data were adjusted to model of Fig. 31(b), without counter electrode contribution, obtaining the values of capacitance and transport resistance shown in Fig. 48. The data presented correspond to two consecutive measurements over the same nanotubes. As can be seen in the figure, the parameters obtained, provided very different behaviours. These results are explained by a different doping level of the nanotubes in the two sets of measurements. The fresh sample showed the typical exponential dependence of transport resistance and capacitance found and modeled in Eqs. (72) and (121) for nanocolloidal samples. However in the second measurement the “aged” sample retains the charge accumulated in the first one.⁶⁷ Doping has been produced by protons in the electrolyte during the first cycle and as a consequence both the capacitance and the resistance tend to be constant for a wide range of potentials.

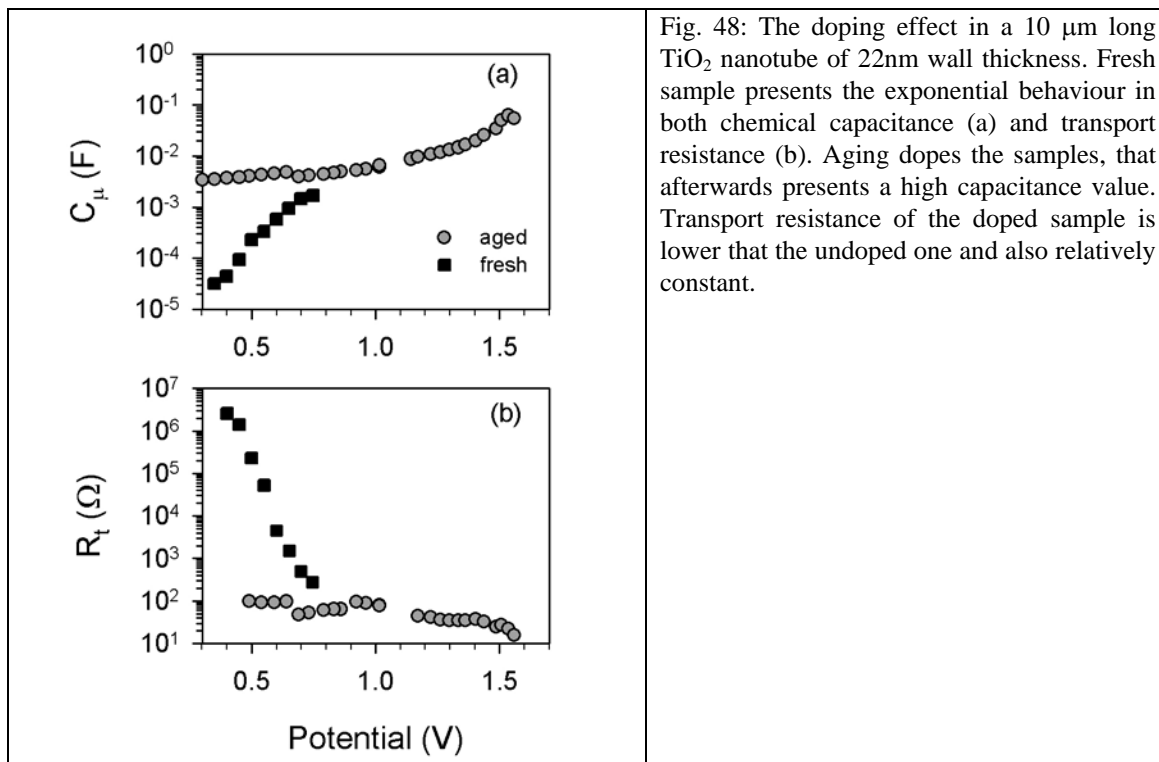


Fig. 48: The doping effect in a 10 μm long TiO_2 nanotube of 22nm wall thickness. Fresh sample presents the exponential behaviour in both chemical capacitance (a) and transport resistance (b). Aging dopes the samples, that afterwards presents a high capacitance value. Transport resistance of the doped sample is lower that the undoped one and also relatively constant.

These data reveal that the nanotubes present a great tendency to become doped. However, transport resistance remained with a relatively high value even after doping. This causes the diffusion length for DSCs made from these nanotubes to maintain values around 10 μm , which is a low value with respect the original expectations.

7.3.3 ZnO nanotubes

Zinc oxide is a wide bandgap semiconductor often proposed for the construction of DSC. Its facility in self organization, forming a variety of shapes such as nanotubes, nanorods, whiskers, etc, makes it very attractive for many applications. However in the DSC some problems of stability in the ZnO have been reported as it tends to dissolve. Still, it is a very good candidate to be used in solid state DSCs.¹⁶²

In Fig. 49 the conductivity of 63 μm long nanotubes of ZnO (nt-ZnO) with 16 nm of wall thickness is compared with that of TiO_2 . The first result observed is that when comparing the conductivity of the nt-ZnO in an inert electrolyte and in a DSC configuration, the conduction band in the nt-ZnO is displaced towards higher potentials. The second observation is that the conductivity in nt-ZnO is much larger than in the case of TiO_2 either in nanotube or nanocolloidal configuration. ZnO is believed to have the conduction band at a similar level than TiO_2 ¹⁶³ and therefore the increase of the conductivity should be attributed to a higher mobility of electrons in the nt-ZnO rather

than a shift in the conduction band.

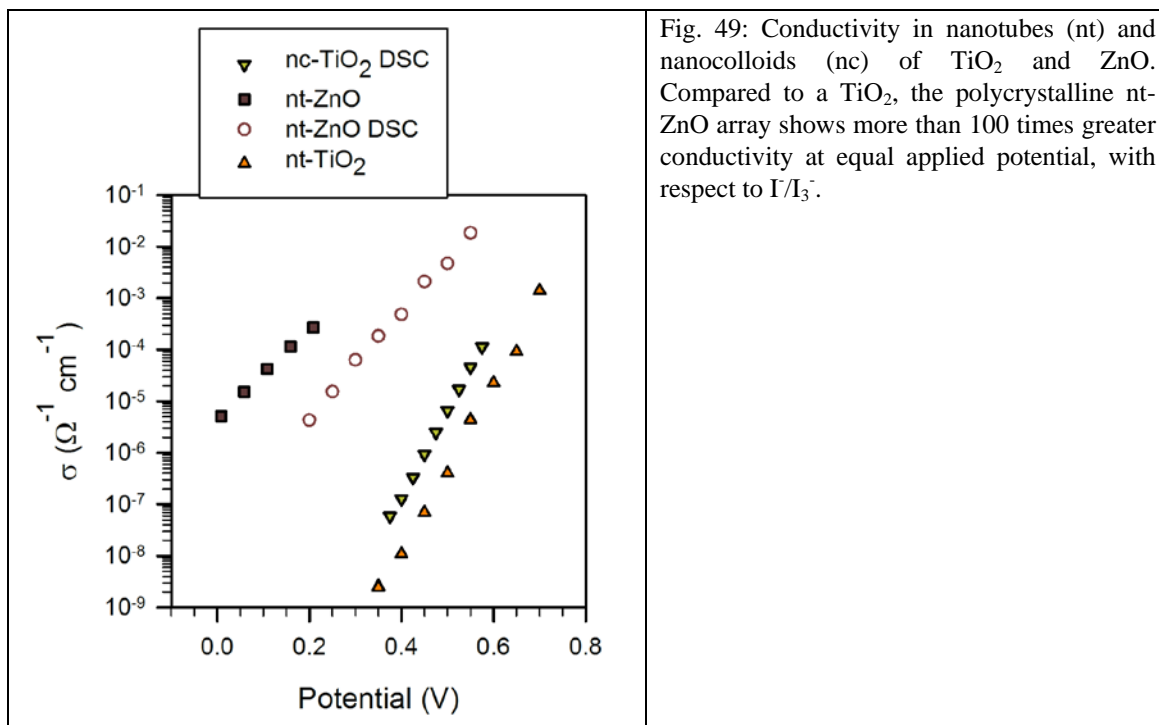


Fig. 49: Conductivity in nanotubes (nt) and nanocolloids (nc) of TiO₂ and ZnO. Compared to a TiO₂, the polycrystalline nt-ZnO array shows more than 100 times greater conductivity at equal applied potential, with respect to I/I₃.

As a consequence of this improved conductivity, the calculated diffusion length of electrons in the nt-ZnO shown in Fig. 50, is several orders of magnitude greater than in the TiO₂. This is an important result with respect to photovoltaic performance as it renders the cell tolerant to much faster electron recombination kinetics and thus an ideal candidate for solid state DSC's.¹⁶²

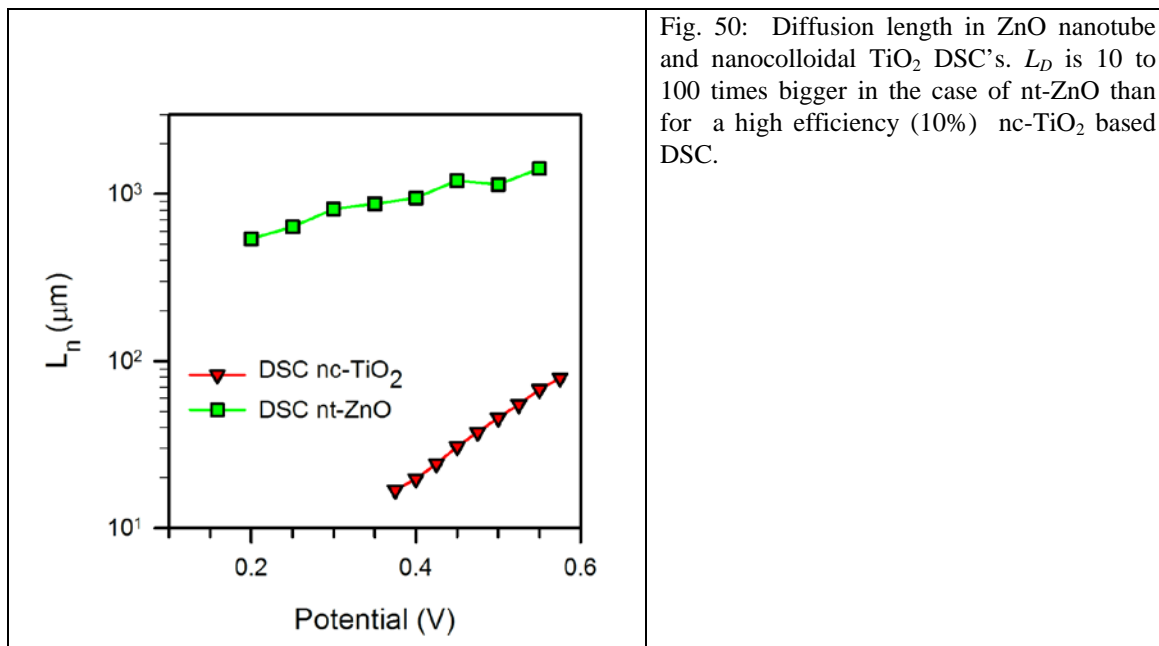


Fig. 50: Diffusion length in ZnO nanotube and nanocolloidal TiO₂ DSC's. L_D is 10 to 100 times bigger in the case of nt-ZnO than for a high efficiency (10%) nc-TiO₂ based DSC.

7.4. Effects of the impedance parameters on the j-V curves

An important practical application of the parameters obtained from impedance is the interpretation of the j-V curves of the solar cells. Since solar cells operate at steady state it is very important to determine the causes of the current density-potential response, which describes the solar cell performance. We have anticipated in Sec. 3 that IS is able to discern the separate factors determining stationary operation of the solar cell. Having described in detail the different resistances that are typically found in DSC as well as their interpretation, in this final section we describe the effects that these resistances have on the performance of the solar cells.^{67,71} In previous sections we have amply used ac equivalent circuits, formed by combinations of linear elements, that allow us to interpret the spectral shape of impedance data.

It is also useful to design a single circuit valid for dc conditions, and we will show here the extension of the circuit in Fig. 5, for DSC. To this end we have to take into consideration several electrochemical interfaces that exist in a DSC. As a consequence the diode in the model of Fig. 5 is substituted by as many recombining resistances as different interfaces are present in the device. There are two interfaces that may lose the photogenerated charge, the TiO₂/electrolyte, described by r_r^{dc} , and the back layer at the bottom of the nanoporous matrix, given by r_{BL}^{dc} , as shown in Fig. 51. To simplify this last model, all the charge transfer losses may be grouped in a single recombination

resistor representing the parallel association of the two contributions, $r_{rec}^{dc} = r_{BL}^{dc} \parallel r_r^{dc}$.

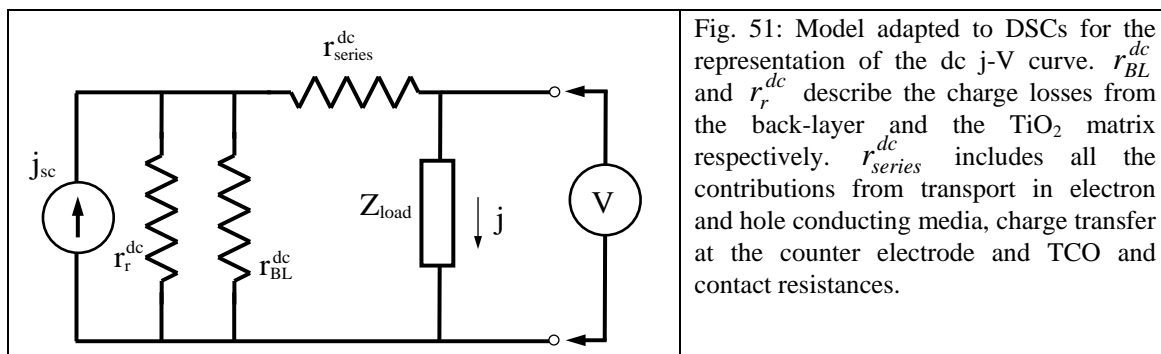


Fig. 51: Model adapted to DSCs for the representation of the dc j-V curve. r_{BL}^{dc} and r_r^{dc} describe the charge losses from the back-layer and the TiO_2 matrix respectively. r_{series}^{dc} includes all the contributions from transport in electron and hole conducting media, charge transfer at the counter electrode and TCO and contact resistances.

Note that the resistances included in Fig. 51 should be applied in dc conditions. In contrast to this, resistances derived from IS are valid only for a small perturbation of the voltage. As stated by Eq. (25), it is necessary to integrate the low frequency resistance, R_{dc} obtained from impedance spectra at different potentials to regenerate the j-V curve.⁶⁶

In the case of DSC, R_{dc} is the sum of two contributions: R_{rec} and R_{series} .

R_{rec} accounts for the overall recombination resistance associated to the cell losses with two main contributions, the charge transfer resistance from the colloid uncovered substrate and from the TiO_2 surface.

$$R_{rec} = R_{BL} \parallel R_r. \quad (171)$$

The series resistance is related to the sum of all the dissipative resistances contributions, thus

$$R_{series} = R_S + R_{Pt} + R_d + R_t / 3 + R_{co}. \quad (172)$$

In solid state DSCs, R_d may be substituted by $R_{HTM} / 3$

It has to be kept in mind, as amply discussed in previous sections, that R_r , R_{BL} and R_{series} are not constant values. To obtain their equivalent dc values of Fig. 51 we need to integrate these ac contributions. Therefore for a certain current j passing through the cell we have

$$r_{series}^{dc} = \frac{1}{j_{sc} - j} \int_{j_{sc}}^j R_{series} di \quad (173)$$

$$r_{rec}^{dc} = \frac{1}{j_{sc} - j} \int_{j_{sc}}^j R_{rec} di \quad (174)$$

Alternatively, to determine the dc contribution of the resistances at a certain applied

potential we can write

$$r_{series}^{dc} = \frac{1}{V} \int_0^V \frac{dV}{R_{series}} \quad (175)$$

$$r_{rec}^{dc} = \frac{1}{V} \int_0^V \frac{dV}{R_{rec}} \quad (176)$$

It is convenient to discuss here the existence of a shunt resistance in DSCs. In crystalline silicon solar cells, r_{shunt} is a constant resistance that accounts for leakage currents crossing the cell.⁷¹ Recent studies have revealed that r_{shunt} may change with the measuring conditions, though these variations are not fully understood.⁹⁵ In DSC the closer element to r_{shunt} is r_{BL} , however it has to be taken into consideration that r_{BL} is a variable resistor which depends on the potential. It may be obtained from

$$r_{BL}^{dc} = \frac{1}{V} \int_0^V \frac{dV}{R_{BL}} \quad (177)$$

with R_{BL} following a Tafel response as the current losses occurring at the back layer/electrolyte interface. Therefore to apply the dc models used in crystalline silicon solar cells in DSCs, we have to substitute r_{shunt} in Fig. 5 by another diode governed by an ideality factor given by the transfer coefficient characteristic of the back layer. This is the two diode model approach used in other types of solar cells.^{164,165}

Once the contributions of the different parameters are identified it is possible to clarify how they influence the j - V curves.

Effect of series resistance

In Fig. 52, the effect of series resistance on the j - V curve is shown. The rise in r_{series}^{dc} decreases the FF and, consequently, the efficiency of the solar cell. If r_{series}^{dc} is too large, also j_{sc} becomes affected. The same effect occurs with large photogenerated currents: the higher the current crosses the cell, the greater the potential drop due to the series resistance corrections is produced and thus the FF and efficiency drop.

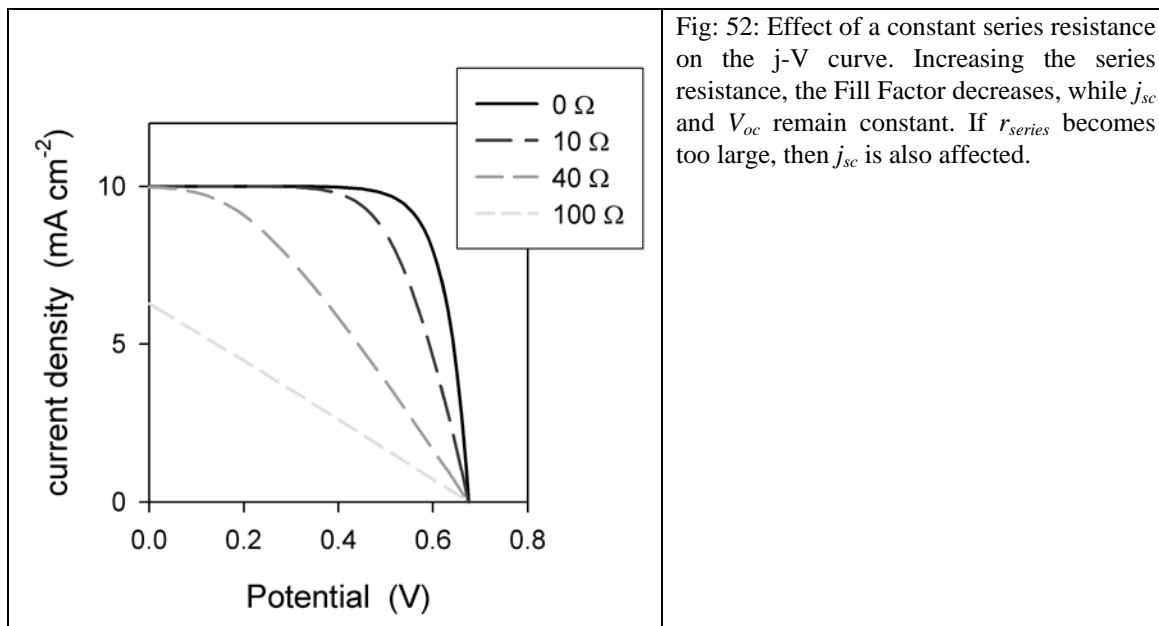


Fig: 52: Effect of a constant series resistance on the j-V curve. Increasing the series resistance, the Fill Factor decreases, while j_{sc} and V_{oc} remain constant. If r_{series} becomes too large, then j_{sc} is also affected.

The series resistance is a very important limiting factor in solar cells, specially if the objective is to scale up to large area cells or the use of dyes with enhanced injection properties. In these cases, a correct choice of the geometric design and the materials used to collect the charge and regenerate the dyes is needed to minimize this resistance.

From another point of view, once the cell is made, we may use the integrated series resistance, to evaluate the improvements that could be obtained eliminating partial or completely r_{series}^{dc} . To do this we just need to subtract the ohmic drop at series resistance from the applied potential from to obtain the corrected potential:

$$V_c = V - i r_{series}^{dc} = V - \int_0^i R_{series} di \quad (178)$$

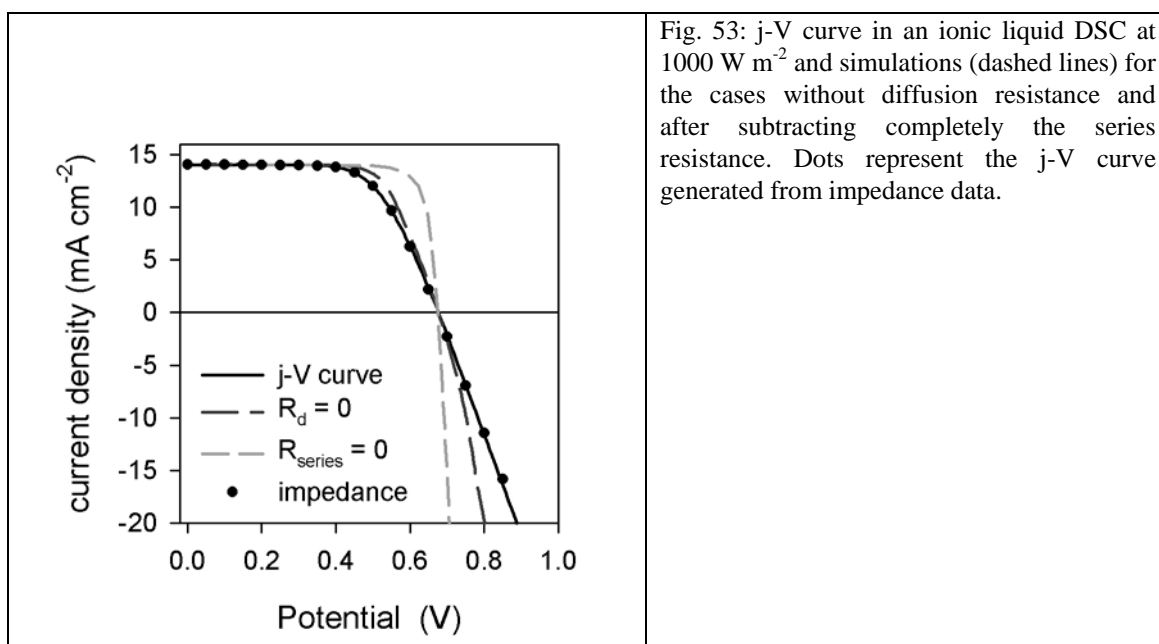


Fig. 53: j-V curve in an ionic liquid DSC at 1000 W m^{-2} and simulations (dashed lines) for the cases without diffusion resistance and after subtracting completely the series resistance. Dots represent the j-V curve generated from impedance data.

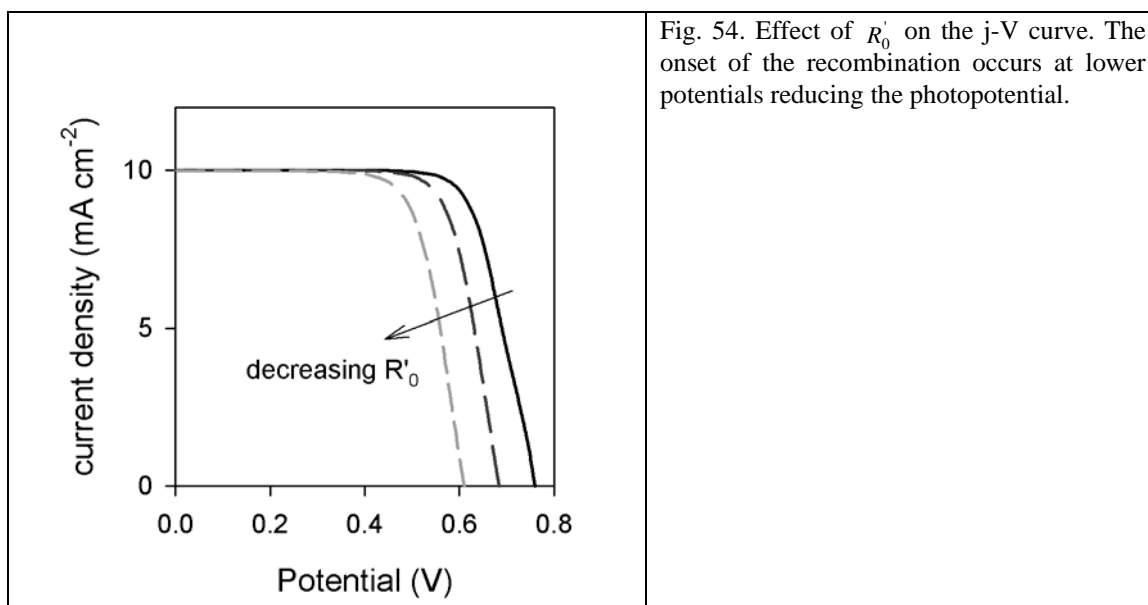
In Fig. 53 the improvements that could be obtained by eliminating different series resistance contributions in a real solar cell are presented. We find that if we could eliminate the diffusion resistance (grey long dashed line), the FF, and thus the efficiency would increase in a 9%. If we could completely eliminate the the total series resistance (light grey short dashed line), then the improvement would be a 28%. The main contribution to the reduction in FF (15%) has to be attributed to the TCO resistance.

Effects related to recombination resistance.

In a DSC, the charge injection is determined by the dye and its interaction with the hole and electron conducting media, providing the maximum current density attainable by the solar cell. As the recombination resistance is the element that determines how the generated charge may be lost, *this* is the parameter that will limit the maximum performance attainable for the solar cell. This maximum efficiency will be then modulated by the series resistance effect as just mentioned above.

Assuming that R_{BL} is large, recombination is dominated by R_r . According to Eqs. (25), (87) and (162) there are a number of factors that affect the j - V curve through the recombination resistance:

- i) A decrease in the absolute value of R'_0 diminishes de photopotential, as shown in Fig. 54.



- ii) A low transfer factor β diminishes the FF of the DSC an thus the maximum

efficiency that may be obtained from it, as indicated in Fig. 55(a)

- iii) However, partially compensating this loss of FF, lower values of β , increase the photopotential as shown in Fig. 55(b). This increase in V_{oc} is due to a lower slope in the dependence of R_r with the potential, Eq. (79), that yields a lower recombination at higher values of the potential.

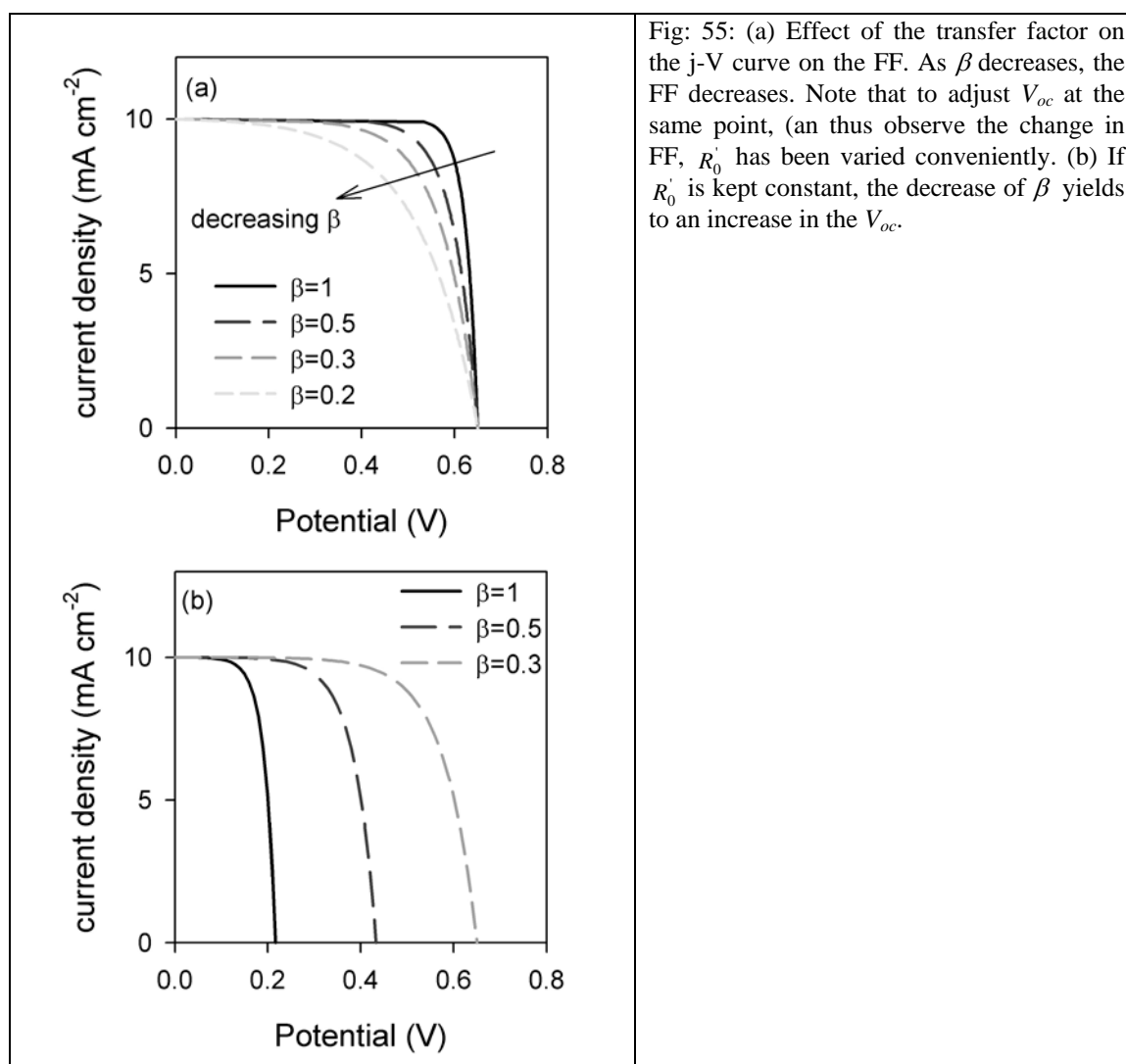


Fig: 55: (a) Effect of the transfer factor on the j-V curve on the FF. As β decreases, the FF decreases. Note that to adjust V_{oc} at the same point, (an thus observe the change in FF, R_0' has been varied conveniently. (b) If R_0' is kept constant, the decrease of β yields to an increase in the V_{oc} .

Effect of increasing temperature.

Increasing the temperature reduces both the charge transfer at the counter electrode and diffusion resistance in the electrolyte, thus reducing the series resistance of the cell.⁶⁶ In solid state solar cells a similar effect occurs, as increasing the temperature reduces hole transport resistance in spiro-OMeTAD.⁶⁸ These reductions contribute to increase the FF of the solar cell.

However, according to Eq. (162) and as shown in Fig. 38, a temperature rise diminishes R_0' what produces a decrease of photopotential, Fig. 54.

The sum of all these contributions produces an increase of the solar cell efficiency when rising the temperature, with a smooth decrease above 30°C. This has been shown in data by Sony Corp. As the slope of R_r with potential is smaller than in the case of semiconductor solar cells, the loss in efficiency with temperature is also smaller.

In summary, the advantage of using IS is that it is possible to distinguish which are the individual electrical contributions influencing the performance of the working cells without destroying them. It is thus possible to identify which are the limiting processes in the cells and to focus the research efforts to enhance the solar cell efficiency in the specific physico-chemical and material properties that need to be improved.

Acknowledgments

This work has benefited from collaborations with many colleagues and friends and we are very grateful to all of them for the discussions and joint work that allowed us to progress in the understanding of the properties of DSCs. Our special gratitude pertains to Professors Michael Grätzel, Craig Grimes, Anders Hagfeldt, Joseph T. Hupp, Arie Zaban, Shaik M. Zakeeruddin and Doctors Gerrit Boschloo, Germà Garcia-Belmonte, Ivan Mora-Seró and Emilio Palomares.

Appendix : properties of measured DSCs

The measurements shown in this work have been performed with a potentiostat PGSTAT-30 equipped with an impedance module FRA from Autolab. Illumination was provided by a 150 W Xe lamp and a commercial 25W halogen lamp for the impedance measurements. j - V characteristics of the samples were taken under 1000 W cm^{-2} 1 sun conditions provided by a 150 W Xe lamp with light filters to adjust the illumination to air mass 1.5 conditions and using a 0.16 cm^2 mask. In the case of solid state cell the mask had 0.13 cm^2 . Low light intensity illumination conditions for impedance measurements was provided by a commercial 50 W halogen lamp for liquid electrolyte cells and by a high intensity white led for solid state cells. High light intensity illumination conditions were provided by the 150 W Xe lamp without air mass filters.

Table 3: Measurements where done over samples with the following characteristics:

Sample	L2noMBI	L5Li	L5Na	IL7	L10	L11	OMeTAD
n-TiO ₂ layer (μm)	7.5	8.1	7.0	6.8	12	12	1.8
Scatter layer (μm)	0	0	0	4	2	4	0
Dye	N3	N3	N3	K19	N719	N719	Z907
Electrolyte	H10a	H10b	H10c	Z380	Z300	Z300	Solid
Area (cm^2)	0.48	0.48	0.48	0.28	0.28	0.28	0.128
Porosity	70%	70%	72%	68%	68%	68%	68%
V_{oc} (V)	0.31	0.58	0.70	0.71	0.80	0.86	0.86
J_{sc} (mA cm^{-2})	12.6	12.3	9.6	14.0	17.5	17.0	9.1
FF	0.52	0.66	0.67	0.71	0.73	0.76	0.51
Efficiency (%)	2	5	5	7	10	11	4

The different dyes and hole conductor media indicated in Table I have the following specifications:

The dyes:

- N3, *cis*-bis(isothiocyanato) bis (2,2'-bipyridyl-4, 4'-dicarboxylato)-

ruthenium(II).

- K-19, Ru-(4,4'-dicarboxylic acid-2,2'-bipyridine)(4,4'-bis(*p*-hexyloxystyryl)-2,2'-bipyridine)(NCS)₂, coadsorbed with phenylpropionic acid (PPA).
- N719, *cis*-di(thiocyanato)-*N,N'*-bis(2,2'-bipyridyl-4-carboxylic acid-4'-tetrabutylammonium carboxylate) ruthenium (II).
- Z907, *cis*-di(thiocyanato)-(2,2'-bipyridyl-4,4'-dicarboxylic acid)(4,4'-dinonyl-2,2'-bipyridyl)-ruthenium(II), coadsorbed with GBA.

The hole or ion conducting media:

- H10a for 0.5M lithium iodide (LiI), 0.05M I₂ in 3-methoxypropionitrile (3-MPN), H10b the same as H10a plus 0.5M 1-methylbenzimidazole (MBI) and H10c for 0.5M Sodium iodide (NaI), 0.05M I₂, and 0.5M MBI in 3-MPN.
- Z380 for N-methylbenzimidazole 0.5 M, guanidinium thiocyanate 0.12 M and iodine (I₂) 0.2 M in a mixture of 1-methyl-3-propylimidazolium iodide & 1-methyl-3-ethylimidazolium thiocyanate, 65%:35% volume ratio.
- Z300 for 0.6 M butylmethylimidazolium iodide, 0.03 M I₂, 0.10 M guanidinium thiocyanate and 0.50 M 4-*tert*-butylpyridine in the mixture of acetonitrile and valeronitrile, 85%:15% volume ratio.
- Solid for (2,2',7,7'-tetrakis(N,N-di-*p*-methoxyphenyl-amine)-9,9'-spiro-bifluorene (spiro-OMeTAD) hole conductor solved in chlorobenzene at a concentration 170mM together with 13 mM Li[(CF₃SO₄)₂N], 110mM 4-*tert*-butyl-pyridine and spin casted 30 s at 2000 rpm.

References

- (1) O' Regan, B.; Grätzel, M. *Nature* **1991**, *353*, 737.
- (2) Gabrielli, C. *Identification of Electrochemical Processes by Frequency Response Analysis*; Solartron Technical Report (<http://www.solartronanalytical.com>), 1980.
- (3) Losee, D. L. *J. Appl. Phys.* **1975**, *46*, 2204.
- (4) Gomes, W. P.; Vanmaekelbergh, D. *Electrochim. Acta* **1996**, *41*, 967.
- (5) Tomkiewicz, M. *Electrochim. Acta* **1990**, *35*, 1631.
- (6) Morrison, S. R. *Electrochemistry at Semiconductor and Oxidized Metal Electrodes*; Plenum Press: New York, 1980.
- (7) Nozik, A. J.; Memming, R. *J. Phys. Chem.* **1996**, *100*, 13061.
- (8) Gerischer, H. *Electrochim. Acta* **1990**, *35*, 1677.
- (9) Kelly, J. J.; Memming, R. *J. Electrochem. Soc.* **1982**, *129*, 730.
- (10) Vanmaekelbergh, D. *Electrochim. Acta* **1997**, *42*, 1135.
- (11) Fajardo, A. M.; Lewis, N. S. *J. Phys. Chem. B* **1997**, *101*, 11136.
- (12) Freund, T.; Morrison, S. R. *Surf. Sci.* **1968**, *9*, 119.
- (13) Allongue, P.; Cachet, H. *J. Electroanal. Chem.* **1984**, *176*, 369.
- (14) Li, J.; Peter, L. M. *J. Electroanal. Chem.* **1985**, *193*, 27.
- (15) Oskam, G.; Vanmaekelbergh, D.; Kelly, J. J. *J. Electroanal. Chem.* **1991**, *315*, 65.
- (16) Zaban, A.; Meier, A.; Gregg, B. A. *J. Phys. Chem. B* **1997**, *101*, 7985.
- (17) van de Lagemaat, J.; Park, N.-G.; Frank, A. J. *J. Phys. Chem. B* **2000**, *104*, 2044.
- (18) Kern, R.; Sastrawan, R.; Ferber, J.; Stangl, R.; Luther, J. *Electrochim. Acta* **2002**, *47*, 4213.
- (19) Hauch, A.; Georg, A. *Electrochim. Acta* **2001**, *46*, 3457.
- (20) Södergren, S.; Hagfeldt, A.; Olsson, J.; Lindquist, S. E. *J. Phys. Chem.* **1994**, *98*, 5552.
- (21) Dloczik, L.; Ieperuma, O.; Lauerman, I.; Peter, L. M.; Ponomarev, E. A.; Redmond, G.; Shaw, N. J.; Uhlendorf, I. *J. Phys. Chem. B* **1997**, *101*, 10281.
- (22) Gärtner, W. *Phys. Rev.* **1959**, *116*, 84.
- (23) Schwarzburg, K.; Willig, F. *J. Phys. Chem. B* **1999**, *28*, 5743.
- (24) Cahen, D.; Hodes, G.; Grätzel, M.; Guillemoles, J. F.; Riess, I. *J. Phys. Chem. B* **2000**, *104*, 2053.
- (25) Gregg, B. A. *J. Phys. Chem. B* **2003**, *107*, 4688.
- (26) van de Lagemaat, J.; Frank, A. J. *J. Phys. Chem. B* **2000**, *104*, 4292.
- (27) Pichot, F.; Gregg, B. A. *J. Phys. Chem. B* **2000**, *104*, 6.
- (28) Schlichthörl, G.; Huang, S. Y.; Sprague, J.; Frank, A. J. *J. Phys. Chem. B* **1997**, *101*, 8141.
- (29) Vanmaekelbergh, D.; de Jongh, P. E. *J. Phys. Chem. B* **1999**, *103*, 747.
- (30) Franco, G.; Gehring, J.; Peter, L. M.; Ponomarev, E. A.; Uhlendorf, I. *J. Phys. Chem. B* **1999**, *103*, 692.
- (31) Markvart, T.; Landsberg, P. T. *Physica E* **2002**, *14*, 71.
- (32) Würfel, P. *Physica E* **2002**, *14*, 18.
- (33) Bisquert, J.; Cahen, D.; Rühle, S.; Hodes, G.; Zaban, A. *J. Phys. Chem. B* **2004**, *108*, 8106.
- (34) Würfel, P. *Physics of Solar Cells. From Principles to New Concepts*; Wiley: Weinheim, 2005.
- (35) Bisquert, J. *Phys. Chem. Chem. Phys.* **2003**, *5*, 5360.
- (36) Nelson, J. *Phys. Rev. B* **1999**, *59*, 15374.
- (37) Rose, A. *Concepts in Photoconductivity and Allied Problems*; Interscience: New York, 1963.
- (38) Marshall, J. M. *J. Non-Cryst. Solids* **1996**, *198-200*, 182.
- (39) Scher, H.; Montroll, E. W. *Phys. Rev. B* **1975**, *12*, 2455.
- (40) Bisquert, J.; Vkhrenko, V. S. *J. Phys. Chem. B* **2004**, *108*, 2313.

- (41) de Levie, R. *Electrochim. Acta* **1963**, 8, 751.
- (42) Mackinnon, W. R.; Haering, R. R. in *Modern Aspects of Electrochemistry*; White, R. E., Bockris, J. O. M., Conway, B. E., Eds.; Plenum Press: New York, 1983; Vol. 15; pp 235.
- (43) Albery, W. J.; Elliot, C. M.; Mount, A. R. *J. Electroanal. Chem.* **1990**, 288, 15.
- (44) Chidsey, C. E. D.; Murray, R. W. *J. Phys. Chem.* **1986**, 90, 1479.
- (45) Brumleve, T. R.; Buck, R. P. *J. Electroanal. Chem.* **1981**, 126, 73.
- (46) Bisquert, J.; Garcia-Belmonte, G.; Fabregat-Santiago, F.; Ferriols, N. S.; Bogdanoff, P.; Pereira, E. C. *J. Phys. Chem. B* **2000**, 104, 2287.
- (47) Bisquert, J. *J. Phys. Chem. B* **2002**, 106, 325.
- (48) Bisquert, J.; Compte, A. *J. Electroanal. Chem.* **2001**, 499, 112.
- (49) Bisquert, J. *Phys. Chem. Chem. Phys.* **2000**, 2, 4185.
- (50) Fabregat-Santiago, F.; Garcia-Belmonte, G.; Bisquert, J.; Bogdanoff, P.; Zaban, A. *J. Electrochem. Soc.* **2002**, 150, E293.
- (51) Fabregat-Santiago, F.; Bisquert, J.; Garcia-Belmonte, G.; Boschloo, G.; Hagfeldt, A. *Sol. Energy Mater. Sol. Cells* **2005**, 87, 117.
- (52) Fabregat-Santiago, F.; Garcia-Belmonte, G.; Bisquert, J.; Zaban, A.; Salvador, P. *J. Phys. Chem. B* **2002**, 106, 334.
- (53) Fabregat-Santiago, F.; Mora-Seró, I.; Garcia-Belmonte, G.; Bisquert, J. *J. Phys. Chem. B* **2003**, 107, 758.
- (54) Bisquert, J.; Zaban, A.; Greenshtein, M.; Mora-Seró, I. *J. Am. Chem. Soc.* **2004**, 126, 13550.
- (55) Fabregat-Santiago, F.; García-Cañadas, J.; Palomares, E.; Clifford, J. N.; Haque, S. A.; Durrant, J. R.; Garcia-Belmonte, G.; Bisquert, J. *J. Appl. Phys.* **2004**, 96, 6903.
- (56) Fisher, A. C.; Peter, L. M.; Ponomarev, E. A.; Walker, A. B.; Wijayantha, K. G. U. *J. Phys. Chem. B* **2000**, 104, 949.
- (57) Zaban, A.; Greenshtein, M.; Bisquert, J. *ChemPhysChem* **2003**, 4, 859.
- (58) Bisquert, J. *J. Phys. Chem. B* **2004**, 108, 2323.
- (59) Peter, L. M. *J. Phys. Chem. C* **2007**, 111, 6601.
- (60) Bisquert, J. *Phys. Chem. Chem. Phys.* **2008**, 10, 49.
- (61) Bisquert, J. *Phys. Chem. Chem. Phys.* **2008**, 10, 3175.
- (62) Wang, Q.; Moser, J.-E.; Grätzel, M. *J. Phys. Chem. B* **2005**, 109, 14945.
- (63) Hoshikawa, T.; Kikuchi, R.; Eguchi, K. *J. Electroanal. Chem.* **2006**, 588, 59.
- (64) Adachi, M.; Sakamoto, M.; Jiu, J.; Ogata, Y.; Isoda, S. *J. Phys. Chem. B* **2006**, 110, 13872.
- (65) Wang, Q.; Ito, S.; Grätzel, M.; Fabregat-Santiago, F.; Mora-Seró, I.; Bisquert, J.; Bessho, T.; Imai, H. *J. Phys. Chem. B* **2006**, 110, 19406.
- (66) Fabregat-Santiago, F.; Bisquert, J.; Palomares, E.; Otero, L.; Kuang, D.; Zakeeruddin, S. M.; Grätzel, M. *J. Phys. Chem. C* **2007**, 111, 6550.
- (67) Fabregat-Santiago, F.; Barea, E. M.; Bisquert, J.; Mor, G. K.; Shankar, K.; Grimes, C. A. *J. Am. Chem. Soc.* **2008**, 130, 11312.
- (68) Fabregat-Santiago, F.; Bisquert, J.; Cevey, L.; Chen, P.; Wang, M.; Zakeeruddin, S. M.; Grätzel, M. *J. Am. Chem. Soc.* **2009**, 131, 558.
- (69) Sah, C.-T. *Fundamentals of Solid State Electronics*; World Scientific: Singapur, 1991.
- (70) Prince, M. B. *Journal of Applied Physics* **1955**, 26, 534.
- (71) Sze, S. M. *Physics of Semiconductor Devices*, 2nd ed.; John Wiley and Sons: New York, 1981.
- (72) Jonscher, A. K. *Dielectric Relaxation in Solids*; Chelsea Dielectrics Press: London, 1983.
- (73) Macdonald, J. R. *Impedance Spectroscopy*; John Wiley and Sons: New York, 1987.
- (74) Bisquert, J. *Electrochim. Acta* **2002**, 47, 2435.
- (75) Bisquert, J. *Phys. Rev. B* **2008**, 77, 235203.
- (76) Mora-Seró, I.; Bisquert, J.; Fabregat-Santiago, F.; Garcia-Belmonte, G.; Zoppi,

- G.; Durose, K.; Proskuryakov, Y. Y.; Oja, I.; Belaidi, A.; Dittrich, T.; Tena-Zaera, R.; Katty, A.; Lévy-Clement, C.; Barrioz, V.; Irvine, S. J. C. *Nano Lett.* **2006**, *6*, 640.
- (77) Pajkossy, T. *J. Electroanal. Chem.* **1994**, *364*, 111.
- (78) Varney, R. N.; Fischer, L. H. *Am. J. Phys.* **1980**, *48*, 405.
- (79) Jamnik, J.; Maier, J. *Phys. Chem. Chem. Phys.* **2001**, *3*, 1668.
- (80) Glunz, S. W. *Adv. Optoelect.* **2007**, 97370.
- (81) Abayev, I.; Zaban, A.; Fabregat-Santiago, F.; Bisquert, J. *Phys. Stat. Sol. (a)* **2003**, *196*, R4.
- (82) Snaith, H. J.; Schmidt-Mende, L. *Adv. Mat.* **2007**, *19*, 3187.
- (83) Niinobe, D.; Makari, Y.; Kitamura, T.; Wada, Y.; Yanagida, S. *J. Phys. Chem. B* **2005**, *109*, 17892.
- (84) Zhang, Z.; Zakeeruddin, S. M.; O'Regan, B. C.; Humphry-Baker, R.; Grätzel, M. *J. Phys. Chem. B* **2005**, *109*, 21818.
- (85) Berger, T.; Lana-Villarreal, T.; Monllor-Satoca, D.; Gomez, R. *J. Phys. Chem. C* **2007**, *111*, 9936.
- (86) Ruhle, S.; Greenshtein, M.; Chen, S.-G.; Merson, A.; Pizem, H.; Sukenik, C. S.; Cahen, D.; Zaban, A. *J. Phys. Chem. B* **2005**, *109*, 18907.
- (87) Bisquert, J.; Fabregat-Santiago, F.; Mora-Seró, I.; Garcia-Belmonte, G.; Barea, E. M.; Palomares, E. *Inorg. Chim. Acta* **2008**, *361*, 684.
- (88) Dor, S.; Ruhle, S.; Grinis, L.; Zaban, A. *J. Phys. Chem. C* **2009**, *113*, 2022.
- (89) Hamman, T. W.; Jensen, R. A.; Martinson, A. B. F.; Ryswykac, H. V.; Hupp, J. T. *Energy Environ. Sci.* **2008**, *1*, 66.
- (90) Peter, L. M. *J. Electroanal. Chem.* **2007**, *599*, 233.
- (91) Mora-Seró, I.; Fabregat-Santiago, F.; Denier, B.; Bisquert, J.; Tena-Zaera, R.; Elias, J.; Lévy-Clement, C. *Appl. Phys. Lett.* **2006**, *89*, 203117.
- (92) Mora-Seró, I.; Bisquert, J. *Nano Lett.* **2003**, *3*, 945.
- (93) Sato, N. *Electrochemistry at Metal and Semiconductor Electrodes*; Elsevier: Amsterdam, 1998.
- (94) Mora-Seró, I.; Garcia-Belmonte, G.; Boix, P. P.; Vázquez, M. A.; Bisquert, J. *Energy Environ. Sci.* **2009**, DOI:1039/B812468J.
- (95) Bashahu, M.; Nkundabakura, P. *Solar Energy* **2007**, *81*, 856.
- (96) Cameron, P. J.; Peter, L. M. *J. Phys. Chem. B* **2005**, *109*, 7392.
- (97) Huang, S. Y.; Schilchthörl, G.; Nozik, A. J.; Grätzel, M.; Frank, A. J. *J. Phys. Chem. B* **1997**, *101*, 2576.
- (98) Clifford, J. N.; Palomares, E.; Nazeeruddin, M. K.; Grätzel, M.; Durrant, J. R. *J. Phys. Chem. C* **2007**, *111*, 6561.
- (99) Lyon, L. A.; Hupp, J. T. *J. Phys. Chem. B* **1999**, *103*, 4623.
- (100) Miyashita, M.; Sunahara, K.; Nishikawa, T.; Uemura, Y.; Koumura, N.; Hara, K.; Mori, A.; Abe, T.; Suzuki, E.; Mori, S. *J. Am. Chem. Soc.* **2008**, *130*, 17874.
- (101) Clifford, J. N.; Palomares, E.; Nazeeruddin, M. K.; Grätzel, M.; Nelson, J.; Li, X.; Long, N. J.; Durrant, J. R. *J. Am. Chem. Soc.* **2004**, *126*, 5225.
- (102) Bisquert, J.; Zaban, A.; Salvador, P. *J. Phys. Chem. B* **2002**, *106*, 8774.
- (103) Salvador, P.; González-Hidalgo, M.; Zaban, A.; Bisquert, J. *The Journal of Physical Chemistry B* **2005**, *109*, 15915.
- (104) Hens, Z. *J. Phys. Chem. B* **1999**, *103*, 122.
- (105) Hens, Z.; Gomes, W. P. *J. Phys. Chem. B* **1999**, *103*, 130.
- (106) Bisquert, J.; Zaban, A.; Greenshtein, M.; Mora-Seró, I. *Journal of the American Chemical Society* **2004**, *126*, 13550.
- (107) Rickert, H. *Electrochemistry of Solids*; Springer Verlag: Berlin, 1982.
- (108) Bisquert, J.; Garcia-Belmonte, G.; Fabregat Santiago, F. *J. Solid State Electrochem.* **1999**, *3*, 337.
- (109) Turrión, M.; Bisquert, J.; Salvador, P. *J. Phys. Chem. B* **2003**, *107*, 9397.
- (110) Rühle, S.; Dittrich, T. *J. Phys. Chem. B* **2005**, *109*, 9522.
- (111) Lana-Villarreal, T.; Bisquert, J.; Mora-Seró, I.; Salvador, P. *J. Phys. Chem. B* **2005**, *109*, 10355.

- (112) Schiff, E. A. *Sol. Energy Mater. Sol. Cells* **2003**, 78, 567.
- (113) Blom, P. W. M.; Vissenberg, M. C. J. M. *Mat. Sci. Eng. R* **2000**, 27, 53.
- (114) Lampert, M. A.; Mark, P. *Current Injection in Solids*; Academic: New York, 1970.
- (115) Onsager, L.; Fuoss, R. M. *J. Phys. Chem.* **1932**, 36, 2689.
- (116) Gomer, R. *Rep. Prog. Phys.* **1990**, 53, 917.
- (117) Myshlyatsev, A. V.; Stepanov, A. A.; Uebing, C.; Zhdanov, V. P. *Physical Review B* **1995**, 52, 5977.
- (118) Darken, L. S. *Trans. Am. Inst. Min. Eng.* **1948**, 175, 184.
- (119) Tiedje, T.; Rose, A. *Solid State Commun.* **1981**, 37, 49.
- (120) Orenstein, J.; Kastner, M. *Phys. Rev. Lett.* **1981**, 46, 1421.
- (121) Hoesterey, D. C.; Letson, G. M. *J. Phys. Chem. Solids* **1963**, 24, 1609.
- (122) Pomerantz, Z.; Zaban, A.; Ghosh, S.; Lellouche, J.-P.; Garcia-Belmonte, G.; Bisquert, J. *J. Electroanal. Chem.* **2008**, doi: 10.1016/j.jelechem.2007.11.005.
- (123) Bailes, M.; Cameron, P. J.; Lobato, K.; Peter, L. M. *J. Phys. Chem. B* **2005**, 109, 15429.
- (124) van de Lagemaat, J.; Kopidakis, N.; Neale, N. R.; Frank, A. J. *Phys. Rev. B* **2005**, 71, 035304.
- (125) Peter, L. M.; Dunn, H. K. *J. Phys. Chem. C* **2009**, 113, 1021/jp810884q.
- (126) Candy, J.-P.; Fouilloux, P.; Keddad, M.; Takenouti, H. *Electrochim. Acta* **1981**, 26, 1029.
- (127) Albery, W. J.; Mount, A. R. *J. Chem. Soc. Faraday Trans.* **1994**, 90, 1115.
- (128) Paasch, G.; Micka, K.; Gersdorf, P. *Electrochim. Acta* **1993**, 38, 2653.
- (129) Bisquert, J.; Grätzel, M.; Wang, Q.; Fabregat-Santiago, F. *J. Phys. Chem. B* **2006**, 110, 11284.
- (130) Pitarch, A.; Garcia-Belmonte, G.; Mora-Seró, I.; Bisquert, J. *Phys. Chem. Chem. Phys.* **2004**, 6, 2983.
- (131) Brioullin, L. *Wave Propagation in Periodic Structures*; Dover: New York, 1953.
- (132) Bisquert, J.; Garcia-Belmonte, G.; Fabregat-Santiago, F.; Compte, A. *Electrochim. Commun.* **1999**, 1, 429.
- (133) Bisquert, J.; Garcia-Belmonte, G.; Fabregat-Santiago, F.; Bueno, P. R. *J. Electroanal. Chem.* **1999**, 475, 152.
- (134) Garcia-Belmonte, G.; Bisquert, J.; Pereira, E. C.; Fabregat-Santiago, F. *J. Electroanal. Chem.* **2001**, 508, 48.
- (135) Bisquert, J.; Vikhrenko, V. S. *Electrochim. Acta* **2002**, 47, 3977.
- (136) Nelson, J. *The Physics of Solar Cells*; Imperial College Press: London, 2003.
- (137) Bisquert, J.; Garcia Belmonte, G. *Electron. Lett.* **1997**, 33, 900.
- (138) Peter, L. M.; Duffy, N. W.; Wang, R. L.; Wijayantha, K. G. U. *J. Electroanal. Chem.* **2002**, 524-525, 127.
- (139) He, C.; Zhao, L.; Zheng, Z.; Lu, F. *J. Phys. Chem. C* **2008**, 112, 18730.
- (140) Randriamahazaka, H.; Fabregat-Santiago, F.; Zaban, A.; García-Cañadas, J.; Garcia-Belmonte, G.; Bisquert, J. *Phys. Chem. Chem. Phys.* **2006**, 8, 1827.
- (141) Kavan, L.; Grätzel, M. *Electrochim. Acta* **1995**, 40, 643.
- (142) Boschloo, G.; Fitzmaurice, D. *J. Phys. Chem. B* **1999**, 103, 7860.
- (143) Wang, H.; He, J.; Boschloo, G.; Lindström, H.; Hagfeldt, A.; Lindquist, S. *J. Phys. Chem. B* **2001**, 105, 2529.
- (144) Gregg, B. A.; Pichot, F.; Ferrere, S.; Fields, C. L. *J. Phys. Chem. B* **2001**, 105, 1422.
- (145) Wang, Q.; Zhang, Z.; Zakeeruddin, S. M.; Gratzel, M. *J. Phys. Chem. C* **2008**, 112, 7084.
- (146) Bisquert, J. *J. Phys. Chem. C* **2007**, 111, 17163.
- (147) Okermann, T.; Zhang, D.; Yoshida, T.; Minoura, H. *J. Phys. Chem. B* **2004**, 108, 2227.
- (148) Halme, J.; Boschloo, G.; Hagfeldt, A.; Lund, P. *J. Phys. Chem. C* **2008**, 112, 5623.

- (149) Peter, L. M.; Dunn, H. K. *J. Phys. Chem. C* **2009**, *113*, 4726.
- (150) Barnes, P. R. F.; Anderson, A. Y.; Koops, S.; Durrant, J. R.; O'Regan, B. *J. Phys. Chem. C* **2009**, *113*, 1126.
- (151) Cao, Y.; Bai, Y.; Yu, Q.; Cheng, Y.; Liu, S.; Shui, D.; Gao, F.; Wang, P. *J. Phys. Chem. C* **2009**, *113*, ASAP.
- (152) Lobato, K.; Peter, L. M.; Wurfel, U. *J. Phys. Chem. B* **2006**, *110*, 16201.
- (153) Lobato, K.; Peter, L. M. *J. Phys. Chem. B* **2006**, *110*, 21920.
- (154) Peter, L. M.; Walker, A. B.; Boschloo, G.; Hagfeldt, A. *J. Phys. Chem. B* **2006**, *110*, 13694.
- (155) Quintana, M.; Edvinsson, T.; Hagfeldt, A.; Boschloo, G. *J. Phys. Chem. C* **2007**, *111*, 1035.
- (156) Baxter, J. B.; Aydil, E. S. *Appl. Phys. Lett.* **2005**, *86*, 053114.
- (157) Baxter, J. B.; Aydil, E. S. *Sol. Energy Mater. Sol. Cells* **2006**, *90*, 607.
- (158) Martinson, A. B. F.; Elam, J. W.; Hupp, J. T.; Pellin, M. J. *Nano Lett.* **2007**, *7*, 2183.
- (159) Martinson, A. B. F.; McGarrah, J. E.; Parpia, M. O. K.; Hupp, J. T. *Phys. Chem. Chem. Phys.* **2006**, *8*, 4655.
- (160) Mor, G. K.; Shankar, K.; Paulose, M.; Varghese, O. K.; Grimes, C. A. *Appl. Phys. Lett.* **2007**, *91*, 152111.
- (161) Mor, G. K.; Varghese, O. K.; Paulose, M.; Shankar, K.; Grimes, C. A. *Sol. Energy Mater. Sol. Cells* **2006**, *90*, 2011.
- (162) Martinson, A. B. F.; Goes, M. S.; Fabregat-Santiago, F.; Bisquert, J.; Pellin, M. J.; Hupp, J. T. *J. Phys. Chem. A* **2009**.
- (163) Memming, R. *Semiconductor Electrochemistry*; Wiley-VCH: Weinheim, 2001.
- (164) Araujo, G. L.; Sanchez, E.; Marti, M. *Solar Cells* **1982**, *5*, 199.
- (165) Arcipiani, B. *Revue de Physique Appliquée* **1985**, *20*, 269.